TUM SCHOOL OF NATURAL SCIENCES

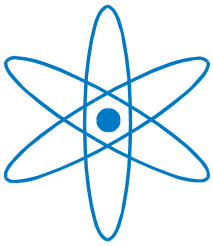

Unraveling Hybrid Plasmonic Nanostructures Using Advanced Scattering Technique

Dissertation

von

Tianfu Guan

TECHNISCHE UNIVERSITÄT MÜNCHEN

TECHNISCHE UNIVERSITÄT MÜNCHEN

TUM School of Natural Sciences

Unraveling Hybrid Plasmonic Nanostructures Using Advanced Scattering Technique

Tianfu Guan

Vollständiger Abdruck der von der TUM School of Natural Sciences der Technischen Universität München zur Erlangung eines

Doktors der Naturwissenschaften (Dr. rer. nat.)

genehmigten Dissertation.

Vorsitz:	Prof. Dr. Andreas Weiler
Prüfer der Dissertation:	1. Prof. Dr. Peter Müller-Buschbaum
	2. apl. Prof. Dr. Hristo Iglev

Die Dissertation wurde am 06.09.2024 bei der Technischen Universität München eingereicht und durch die TUM School of Natural Sciences am 31.10.2024 angenommen.

Abstract

Hybrid plasmonic nanostructures have attracted significant interest for their ability to combine the unique properties of their constituent materials. The use of hybrid materials enhances the overall performance of these nanostructures and expands their range of potential applications. However, there is a lack of comprehensive studies that integrate detailed structural analysis with practical application scenarios. In this thesis, I successfully fabricated hybrid plasmonic nanostructures and conducted an in-depth morphological analysis using grazing-incidence X-ray scattering (GIXS) techniques. The GIXS analysis provides critical insights into the optimal properties of these nanostructures, facilitating their application in specific contexts. Our research approach combines both fabrication and characterization methodologies, aiming to inspire potential advancements in the field of plasmonics.

Zusammenfassung

Hybride plasmonische Nanostrukturen haben aufgrund ihrer Fähigkeit, die einzigartigen Eigenschaften ihrer Bestandteile zu kombinieren, großes Interesse geweckt. Der Einsatz hybrider Materialien verbessert die Gesamtleistung dieser Nanostrukturen und erweitert ihre potenziellen Anwendungsbereiche. Es mangelt jedoch an umfassenden Studien, die eine detaillierte Strukturanalyse mit praktischen Anwendungsszenarien integrieren. In dieser Arbeit habe ich erfolgreich hybride plasmonische Nanostrukturen hergestellt und eine eingehende morphologische Analyse mittels streifender Röntgenbeugung durchgeführt. Die Analyse mit Röntgenstreuung unter streifendem Einfall liefert entscheidende Einblicke in die optimalen Eigenschaften dieser Nanostrukturen und erleichtert deren Anwendung in spezifischen Kontexten. Unser Forschungsansatz kombiniert sowohl Herstellungs- als auch Charakterisierungsmethoden und soll potenzielle Fortschritte im Bereich der Plasmonik inspirieren.

Contents

List of abbreviations

SPR: Surface plasmon resonance
LSPR: Localized surface plasmon resonance
Au NPs: Gold nanoparticles
Au NSs: Gold nanospheres
DLS: Dynamic Light Scattering
UV/Vis: Ultraviolet-visible spectroscopy
SEM: Scanning electron microscopy
PL: Photoluminescence
TRPL: Time-resolved photoluminescence
SERS: Surface-enhanced Raman scattering
DA: Decoupling approximation
DC: Direct current
DWBA: Distorted wave Born approximation
DESY: Deutsches Elektronen-Synchrotron
SDD: Sample-to-detector distance
SLD: Scattering length density
GIXS: Grazing-incidence X-ray scattering
GISAXS: Grazing-incidence small-angle X-ray scattering
GIWAXS: Grazing-incidence wide-angle X-ray scattering
HiPIMS: High-power impulse magnetron sputter
LMA: Local monosdisperse approximation
QCM: Quartz crystal microbalance
QD: Quantum dot
DI water: Deionized water
R6G: Rhodamine 6G
IDE: Inter digital electrode
CTAB: Cetyltrimethylammonium bromide
CTAC: Cetyltrimethylammonium chloride
MPTES: (3-Mercaptopropyl) trimethoxysilane
MeOH: Methanol
PbS QDs: Lead sulfide quantum dots
BMNs: Bimetallic nanostructures

1 Introduction

Light-matter interactions involve collective electronic oscillations, known as plasmons, responsible for special optical capabilities [1, 2]. The development of classical electromagnetic theory provided a scientific framework to explain these phenomena. The study of plasmons and their effects has greatly expanded the knowledge of optical physics, leading to the development of the plasmonics field. Notably, even before contemporary science formally defined the mechanism, people had already begun using metal nanomaterials, despite lacking systematic preparation methods and characterization techniques. Historical examples of the use of metal nanomaterials include the Lycurgus Cup from ancient Rome and the stained glass windows of medieval churches [3]. These artifacts contain silver and gold nanoparticles (Au NPs) of varying sizes, which produce color-changing effects based on the direction of light illumination. A landmark contribution to the modern understanding of these phenomena is made by Gustav Mie, who applied Maxwell's equations to describe how subwavelength gold spheres strongly absorb green light when illuminated by a plane wave [4]. His work detailed the scattering, extinction, and absorption of light by spherical metal particles, explaining the localized surface plasmon resonance (LSPR).

In the past decade, significant breakthroughs in advanced characterization and synthesis techniques have paved the way for the development of metal nanoparticles with precisely controlled properties [5, 6]. Among the key plasmonic materials including gold (Au), silver (Ag), platinum (Pt), copper (Cu), and aluminum (Al) are favored for their exceptional optical and chemical properties [7]. Current research is pushing the boundaries of plasmonics by exploring hybrid nanostructures that combine plasmonic metals with additional metals or semiconductor materials [8]. These innovative combinations aim to reduce energy losses and enhance light-matter interactions. The hybrid nanostructures exhibit plasmonic behaviors across a wide range of spectral regions, including the infrared and terahertz, thus expanding the potential applications of plasmonic materials [8].

Recently, several fabrication methods have emerged for developing plasmonic

nanostructures, with the most used being lithography techniques, template fabrication, and colloidal nanoparticle self-assembly methods [4, 9]. Advanced nanofabrication techniques within lithography play a crucial role, which including a variety of approaches, including electron-beam lithography (EBL), focused-ion beam lithography (FIB), dip-pen nanolithography (DPN), laser interference lithography (LIL), nanosphere lithography (NSL), and nanoimprint lithography (NIL) [10, 11]. While lithography techniques achieve high-resolution nanostructures with high throughput, they are often time-consuming and expensive. Template fabrication methods are crucial in guiding the formation and spatial arrangement of nanostructures, preserving the original shape or symmetry of the template [9]. These methods can be broadly categorized into templated synthesis and templated assembly. Templated synthesis involves conducting reactions either within porous membranes or on substrates masked by an auxiliary nanostructure. Templated methods leverage the extensive library of biomolecular structures, available through chemical and biological synthesis, to provide a plethora of templates for constructing plasmonic nanostructures [12]. However, the introduction of various template materials can complicate the process, adding steps and increasing the complexity of the experiments.

Colloidal nanoparticle self-assembly methods, which allow the direct assembly of metal nanoparticles onto various substrates, have garnered significant attention. Various techniques have been proposed, including convective self-assembly, the Langmuir–Blodgett (LB) method, the Marangoni effect, template-assisted methods, and field-assisted methods [9, 13]. Due to the simplicity of their fabrication process, this thesis uses the self-assembly method to create Au nanoarrays for constructing hybrid nanostructures. These assemblies are crucial for generating efficient plasmonic hotspots, which arise from the plasmonic coupling between adjacent nanoparticles. In addition, these fabrication methods can be combined to fully explore and achieve precise control over the nanostructure fabrication process. For example, self-assembled nanospheres can serve as masks in lithographic processes, enhancing the uniformity and periodicity of the structures. Similarly, template fabrication can be integrated with lithography techniques to achieve multi-scale patterning, combining the high resolution of lithography with the large-area capabilities of templating.

Plasmonic structures possess the ability to confine and guide light at the nanoscale, resulting in extraordinarily strong electromagnetic (EM) field enhancement [14]. Surface plasmons arise from the interaction of oscillating free carriers in matter with incident electromagnetic fields. Throughout the lifetime of surface plasmons, various effects emerge, including hot-carrier generation and transfer, local plasmonic thermalization, collective plasmon resonances, and the coupling of plasmonic modes with neighboring resonances or external fields [15, 16]. These phenomena offer numerous opportunities for a wide range of applications such as sensors [17],

photodetectors [18], waveguides [19], bioimaging [20], and energy harvesting [21], as shown in Figure 1.1.

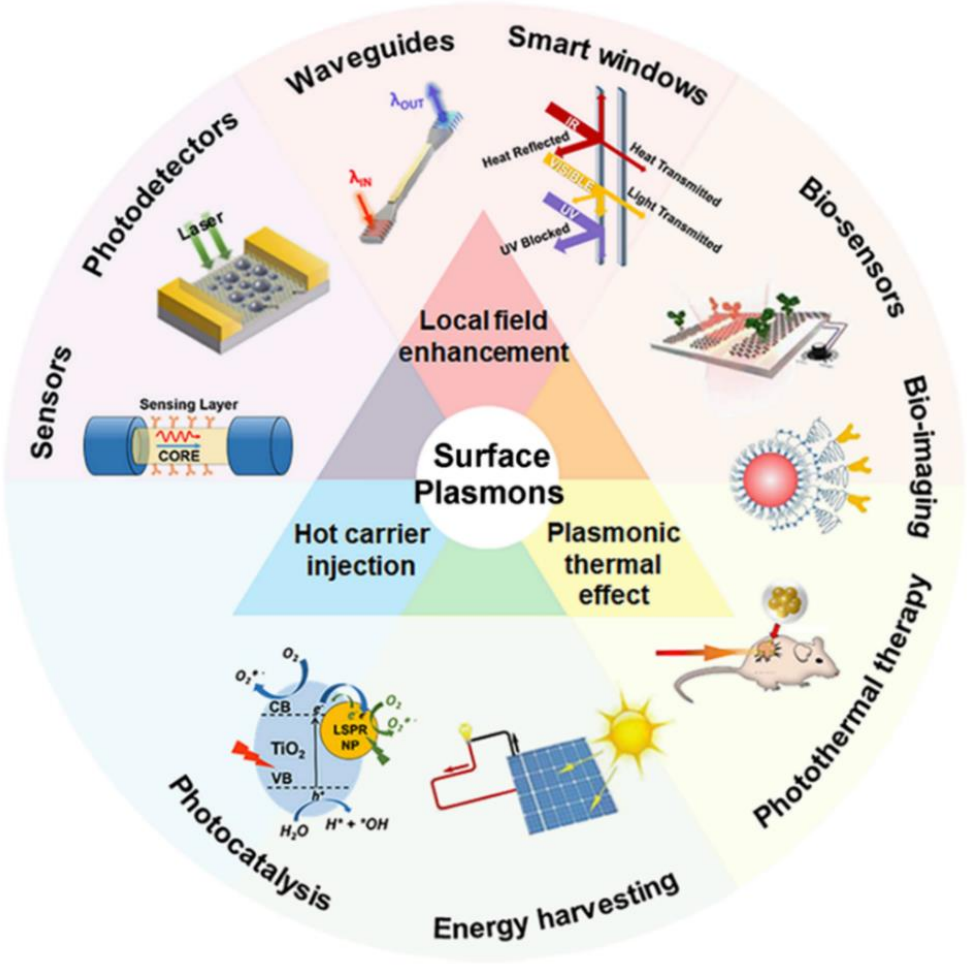

Figure 1.1. *Primary applications of plasmonic nanostructures governed by the corresponding plasmonic effects [11]. Copyright 2023 Elsevier Ltd.*

In the present thesis, the applications of hybrid plasmonic nanostructures in surface-enhanced Raman scattering (SERS) and photodetectors is investigated. The intense EM fields generated at the hot spots can dramatically enhance the signals in SERS measurement. In SERS, the localized EM field enhancement leads to a significant increase in the Raman scattering cross-section, allowing for the identification of molecular fingerprints at extremely low concentrations [22, 23]. This makes SERS a powerful tool for chemical and biological sensing, capable of detecting pollutants, pathogens, and even biomarkers in clinical diagnostics [24]. In addition, plasmonic nanostructures have significantly propelled photodetectors forward by enhancing light absorption, facilitating charge transfer, improving efficiency, and enabling innovative

design strategies [25, 26]. In photodetectors systems, plasmonic nanostructures boost light absorption by concentrating and trapping light at sub-wavelength scales, leading to higher efficiencies. This is particularly beneficial in thin-film photodetectors, where enhanced light absorption can significantly improve the performance. Additionally, plasmonic nanostructures can facilitate hot electron injection, where high-energy electrons generated by plasmon decay contribute to current generation, further increasing the efficiency of photodetectors [27, 28].

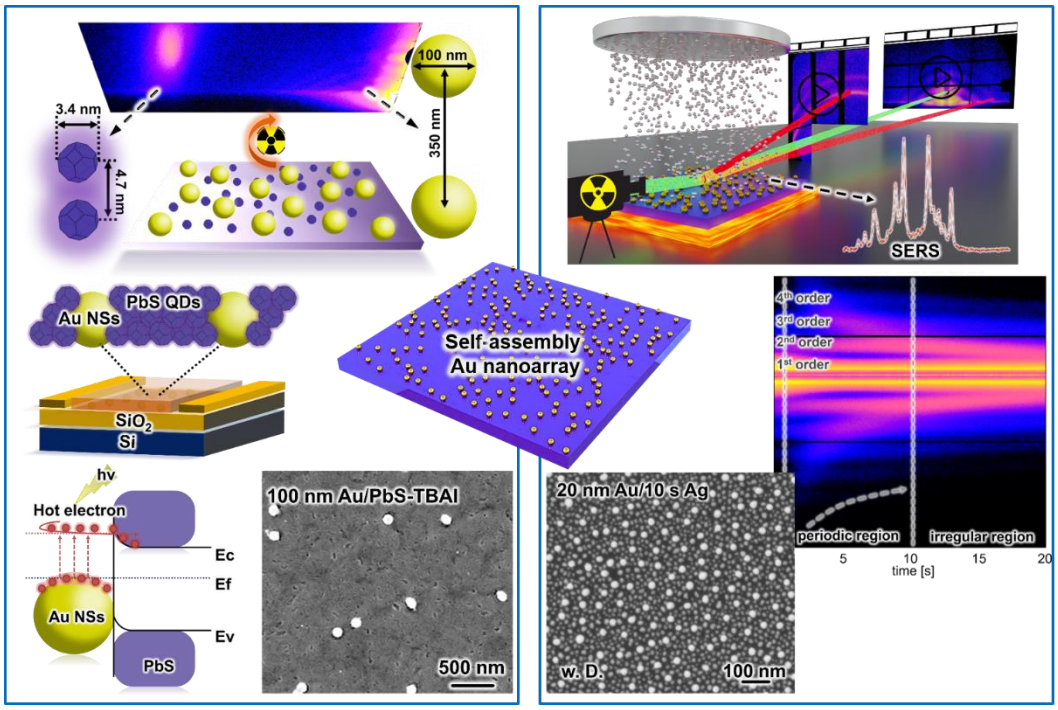

Figure 1.2. *Overview of the projects presented in this Ph.D. thesis. The hybrid plasmonic nanostructures are all fabricated based on self-assembled Au nanoarray and characterization with the GIXS technique. Reproduced with permission from [23, 28]. Copyright 2023 and 2024 American Chemical Society.*

Grazing-incidence X-ray scattering (GIXS) provides a non-destructive method for statistically and reliably probing the internal structure of hybrid plasmonic nanostructures [29, 30]. Grazing-incidence small-angle X-ray scattering (GISAXS) specifically examine the arrangement configurations, inter-dot distances, and Au nanoarray aggregates. Additionally, grazing-incidence wide-angle X-ray scattering (GIWAXS) analyzes the crystallinity of Au nanoarrays. The real features of well-ordered Au nanoarrays can also be simulated using the GISAXS technique. This synergistic use of advanced experimental and simulation methods promises to significantly enhance the understanding and control of plasmonic hybrid nanostructures. In this thesis, Au/Ag and Au/PbS hybrid plasmonic nanostructures are

fabricated based on self-assembled Au NP arrays. The morphology of these hybrid architectures is systematically investigated using GIXS techniques, with further exploration of their applications in photodetectors and SERS platforms. The primary goal of this thesis is to integrate fabrication and characterization methods for potential applications in the plasmonic field. Figure 1.2 provides an overview of the projects presented in this thesis.

In Chapter 2, the theoretical background of plasmonics is presented. This includes fundamentals of Au NPs, such as their basic properties, synthesis, self-assembly, and behavior in colloidal quantum dots, as well as the formation of bimetallic nanostructures. The chapter also elaborates on the basic principles of X-ray scattering and the theory of hybrid nanostructure characterization, with a focus on GISAXS and GIWAXS. Chapter 3 introduces the main characterization and analytical methods used in this thesis, covering both structural and spectroscopic characterizations. It also details the methods for photodetector device characterization and 2D GISAXS data simulation. Chapter 4 covers sample preparation, including all the materials and fabrication processes presented in this thesis.

In Chapter 5, various sizes of Au NPs are synthesized and their optical properties are characterized using dynamic light scattering (DLS) and UV/visible spectroscopy. By comparing scanning electron microscopy (SEM) images of two self-assembly methods, electrostatic adsorption and phase interface transfer, the electrostatic adsorption method provides better nanoparticle arrangement. Therefore, this method is chosen for the further fabrication of hybrid plasmonic nanostructures.

Chapter 6 focuses on creating bimetallic nanostructures on solid supports through high-power impulse magnetron sputter (HiPIMS) deposition of silver (Ag) onto self-assembled Au nanoarray templates. Moderate substrate heating during the sputtering process induces dewetting conditions. The growth dynamics of these hybrid structures are closely examined using *in situ* GISAXS and GIWAXS.

In Chapter 7, a hybrid nanocomposite design is introduced in which a lead sulfide (PbS) layer is deposited on a monolayer of Au NPs. GISAXS is used to examine the internal structure of the Au-PbS hybrid films and conduct a detailed analysis of their morphology. Interdigital photodetectors are developed using this hybrid approach to investigate how the plasmonic nanostructures influence device performance.

The final chapter, summarizes the overall conclusions of this thesis and provides a brief outlook for future research directions.

2 Background

This chapter lays the groundwork for the topics addressed in this thesis by outlining background and theoretical concepts. And these fundamentals are based on the literatures [31-71]. Section 2.1 introduces plasmonics, offering an overview of its principles. Section 2.2 elaborates the fundamental properties, synthesis, and self-assembly of Au NPs. Section 2.3 introduces the Au NPs in colloidal quantum dots and Section 2.4 elaborates the Au NPs based bimetallic nanostructures. Section 2.5 introduces the basic principles of X-ray scattering, including advanced techniques used in this thesis, GISAXS and GIWAXS.

2.1 Plasmonics

Over the past decades, significant advancements in understanding the fundamental physical phenomena and improving fabrication techniques have motivated the research and development of plasmonic nanostructures. Recent progress in fabrication and characterization methodologies have enabled a thorough exploration of plasmon modes and their complex interactions with nanostructures. This in-depth understanding of the fundamental and optical properties of plasmonic nanostructures is crucial for their development to meet diverse applications demands.

Drude model

A plasmon represents the collective oscillations of free electrons within noble metals, acting as the quantum manifestation of plasma oscillations. This concept connects closely with the advancements made by Paul Drude in 1900 through his Drude model, which offers insights into the electron transport mechanisms in metals. The model likens electron dynamics to the motions of particles in an ideal gas, incorporating several critical assumptions for its application. This model assumes that electrons behave as free and independent particles, allowing them to move under the influence of external electric fields according to Newton's laws of motion [3, 31].

During their journey, electrons experience elastic collisions with atomic nuclei, lattice imperfections, or impurities, leading to scattered directions of movement until they freely move again. A notable aspect of Drude's model is the introduction of a mean collision time, τ, termed the relaxation time. This time interval, which is independent of the electrons speed and location, signifies the average duration between collisions and corresponds to a collision probability of $1/\tau$. Furthermore, Drude's theory extends to describe how a metal's dielectric constant may vary with the frequency of an incident electromagnetic wave, incorporating this interaction into the model framework [32].

The model elaborates on the equation of motion for free electrons when subjected to an external, time-varying electric field, expressed as:

$$E(t) = E_0 e^{-i\omega t} \tag{2.1}$$

where E_0 is the field amplitude, ω is the angular frequency of the field, and t is time. This is also stated as:

$$m\frac{d^2x(t)}{dt^2} + m\gamma\frac{dx(t)}{dt} = -eE(t) \tag{2.2}$$

Through this classical perspective, Drude's model not only elucidates the fundamental behaviors of electrons in metals but also connects to a broader understanding of plasmonic oscillations, highlighting the interconnected nature of classical physics and quantum phenomena in the study of electron dynamics and plasmonic behavior.

Solving the equation leads us to the functional relationship of the Drude dispersion model, which is given by:

$$\epsilon_{Drude}(\omega) = 1 - \frac{\omega_p^2}{\omega^2 + i\gamma\omega} \tag{2.3}$$

Here,

$$\omega_p = \sqrt{\frac{ne^2}{m_e\epsilon_0}} \tag{2.4}$$

represents the plasma frequency, which is the natural oscillation frequency of free electrons in their unexcited state. The term n denotes the density of free electrons, e is the elementary charge, m_e refers to the effective mass of an electron, and ϵ_0 is the vacuum permittivity. The frequency ω corresponds to the frequency of the incident light wave, and γ is the radiation damping frequency caused by electron scattering:

$$\gamma = \frac{v_f}{l} = \frac{1}{\tau} \tag{2.5}$$

where v_f is the Fermi velocity, l is the mean free path of the electrons, and τ is the relaxation time.

This model highlights the influence of electron density and scattering mechanisms on the optical properties of metals, specifically how they affect the metal response to electromagnetic radiation. The plasma frequency signifies a critical point beyond which the metal becomes transparent to electromagnetic waves, while the damping factor accounts for energy loss due to electron collisions. The Drude model thus provides a foundational understanding of the optical properties of metals, including their reflective and conductive behaviors.

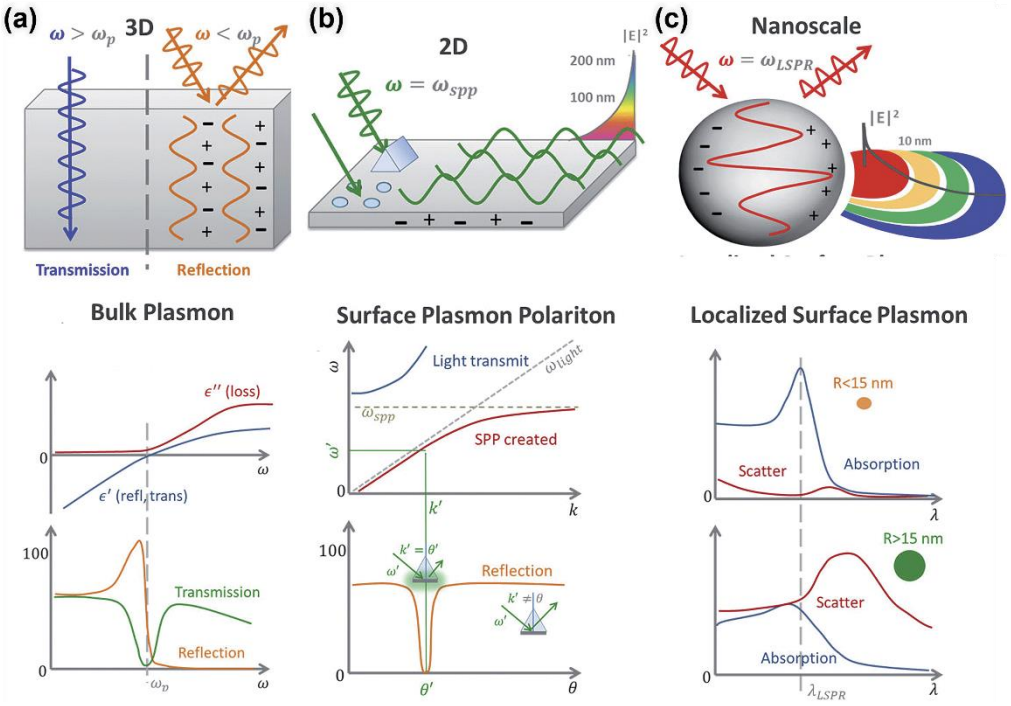

Figure 2.1. *Volume, surface and localized surface plasmon resonances. (a) The plasma frequency of a metal describes the frequency below which the conduction electrons oscillate in the incident field. (b) On a 2D surface, electron oscillations lead to propagating charge waves known as SPPs. These oscillations are coupled to an electromagnetic field which propagates along the interface and with amplitude that exponentially decreases away from the interface. (c) LSPRs exists when the metal nanoparticle is smaller than the incident wavelength, making the electron oscillations in phase. The collective oscillations lead to a large absorption and scattering cross-section, as well as an amplified local EM field. For small particles less than 15 nm, absorption dominates and the absorption cross-section is large. For big nanoparticles greater than 15 nm, the scattering cross-section dominates. The EM field is taken as polarized in the plane of incidence in the figures [32]. Copyright 2015 The Royal Society of Chemistry.*

The concept of plasmons based on the Drude model, manifests in three distinct types across various metal forms are shown in Figure 2.1. In the context of bulk metals (Figure 2.1a), these materials are significantly larger than the wavelength of light in all dimensions, allowing for volumetric electron oscillations. However, when these metals are reduced to thin films (Figure 2.1b), the oscillatory behavior becomes restricted to their surfaces. This leads to the emergence of surface plasmon polaritons (SPPs), commonly referred to as surface plasmons. These surface plasmons are optically excited and can interact with light, enabling the coupling of light into either standing or propagating surface plasmon modes. This coupling is facilitated through the presence of a grating or an imperfection on the metal surface.

Further miniaturization of metal to the scale of nanoparticles (Figure 2.1c), where dimensions are on the order of the light wavelength, gives rise to localized surface plasmons (LSPs). In this situation, the nanoparticles free electrons engage in collective oscillations, significantly influenced by the particle size and shape. LSPs are particularly noteworthy for their ability to concentrate light into sub-wavelength volumes, enhancing local electromagnetic fields.

Mie Theory

In contrast to the bulk metal materials, the metal NPs exhibited unique colors observed with the naked eye. In examining the vivid color revealed by plasmonic NPs, it becomes necessary to reevaluate traditional theories of color formation. This reassessment addresses the seemingly paradoxical shift from the appearance of bulk materials to the vibrant colors observed at the nanoscale. This change in perceived color arises from the nanoscale dimensions of the particles, where their optical characteristics are predominantly influenced by plasmonic effects. These effects are highly sensitive to the size, shape, and surrounding environment of the nanoparticles, leading to the distinct colors observed.

Gustav Mie provided an analytical solution to Maxwell equations, offering a comprehensive description of how spherical particles scatter and absorb light [33]. This solution, known as Mie scattering, complements the earlier understood Rayleigh scattering and specifically addresses the interaction between a plane wave and a homogeneous conducting sphere. The resulting expressions for the total scattering σ_{sca}, extinction σ_{ext}, and absorption σ_{abs} cross-sections are given by:

$$\sigma_{sca} = \frac{2\pi}{|k|^2}\sum_{L=1}^{\infty}(2L+1)(|a_L|^2 + |b_L|^2) \tag{2.6}$$

$$\sigma_{ext} = \frac{2\pi}{|k|^2}\sum_{L=1}^{\infty}(2L+1)\mathrm{Re}(a_L + b_L) \tag{2.7}$$

$$\sigma_{abs} = \sigma_{ext} - \sigma_{sca} \tag{2.8}$$

Here, a_L and b_L are coefficients that depend on the size parameter and the complex refractive index of the particles, with L denoting the order of the multipole contribution. The term k is the wave number of the incident light.

To further investigate the specifics of LSPR phenomena, focusing solely on the dipole approximation provides a frequently cited formula for the resonance behavior of nanoparticle plasmons:

$$\sigma_{ext} = \frac{18\pi\epsilon_m^{3/2}V}{\lambda}\frac{\epsilon_2(\lambda)}{[\epsilon_1(\lambda)+2\epsilon_m]^2+\epsilon_2(\lambda)^2} \tag{2.9}$$

In this expression, V represents the volume of the particle, indicating how the particle size directly influences the extent of light extinction due to resonance. An analogous approach for calculating the scattering cross-section results in:

$$\sigma_{sca} = \frac{32\pi^4\epsilon_m^2V^2}{\lambda^4}\frac{(\epsilon_1-\epsilon_m)^2+\epsilon_2^2}{(\epsilon_1+2\epsilon_m)^2+\epsilon_2^2} \tag{2.10}$$

The terms $\epsilon_1(\lambda)$ and $\epsilon_2(\lambda)$ refer to the real and imaginary parts of the particle dielectric function at wavelength λ, respectively, while ϵ_m is the dielectric constant of the surrounding medium. These formulations highlight the sensitivity of LSPR to changes in the dielectric properties of both the nanoparticle and its environment [34]. As is shown in Figure 2.2a, the illustration of the LSPR excitation and extinction spectra for plasmonic nanospheres (NSs). There is a shift in the resonant wavelength λ^* in response to an alteration in the refractive index of the medium containing the sizes of the plasmonic substance.

Gans Theory

Mie theory, initially developed to describe the scattering and absorption of light by spherical particles, finds its application somewhat limited to this specific geometry. Richard Gans extended Mie's work to encompass particles of different shapes, particularly for non-spherical particles like metallic nanorods, which can be approximated as ellipsoids for the purpose of understanding their optical properties [35]. This adaptation, known as Gans theory, enables the analysis of the optical behaviors of metal nanorods through the dipole approximation, treating these rod-like particles as prolate spheroids.

The absorption cross-section, denoted by σ_{abs}, for metal nanorods, which can be treated as ellipsoids within the dipole approximation of Gans theory, is given by the

following formula:

$$\sigma_{abs} = \frac{\omega^3}{3c}\epsilon_m^{3/2} V \sum_j \left(\frac{1}{P_j^2}\right) \frac{\epsilon_2}{\left\{\epsilon_1 + \left[(1-P_j)/P_j\right]\epsilon_m\right\}^2 + \epsilon_2^2} \tag{2.11}$$

This equation incorporates a summation over the three dimensions of the particle, considering the depolarization factors P_j, which include P_A, P_B, and P_C, corresponding to each axis of the ellipsoid. The condition $A > B = C$ characterizes the particle as a prolate spheroid. The depolarization factors play a crucial role in determining how the shape of the particle influences its optical properties, reflecting the anisotropy inherent in non-spherical particles. Figure 2.2b illustration the LSPR excitation and extinction spectra for plasmonic nanorods (NRs), shows the electron oscillations along the long and short axes.

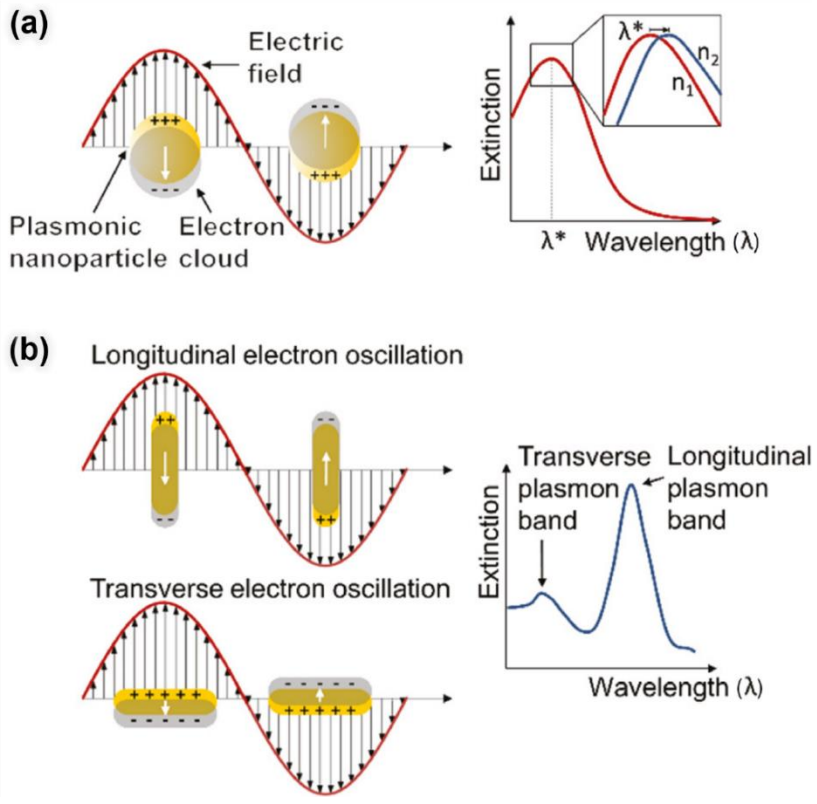

Figure 2.2. *LSPR excitation and extinction spectra for plasmonic (a) nanospheres and (b) nanorods. LSPR detect shifts in the resonance wavelength λ*, shown in the extinction spectra of (a), in response to alterations in the refractive index of the medium containing the plasmonic nanosphere. The nanorods of (b) show longitudinal and transverse plasmon bands corresponding to the electron oscillations along the long and short axes, respectively [34]. Copyright 2018 Walter de Gruyter GmbH.*

2.2 Gold nanoparticles (Au NPs)

Plasmonic Au NPs have emerged as a significant research focus due to their extensive surface area, small size, and tunable reactivity. In this thesis, plasmonic nanostructures based on Au NPs are fabricated. This Section will provide the fundamental properties, synthesis methods, self-assembly techniques, and applications of Au NPs.

2.2.1 Basic properties of Au NPs

SPR in plasmonic Au NPs is a critical optical phenomenon arising from the collective oscillation of free electrons in response to incident electromagnetic radiation. This phenomenon strongly depends on the size and shape of the nanoparticles, among other factors [36]. The optical properties of Au NPs are intricately linked to their size. Smaller Au NPs, typically in the range of a few nanometers, exhibit distinctive quantum size effects, leading to pronounced changes in their optical absorption and scattering properties [37]. The color perception of colloidal gold solutions is one of the most intuitive ways to describe the physicochemical properties of plasmonic nanoparticles. To accurately understand this phenomenon, the concept of color in reflection or transmission must be reconsidered in terms of nanoscale effects. When the size of an object is significantly smaller than the wavelength of incident light, light is not only specularly reflected from the surface but also scattered in various directions [38, 39]. Additionally, light is partially absorbed when passing through the medium. The combined attenuation of incident light by scattering and absorption is defined as extinction. Thus, microscopic reflection corresponds to nanoscale scattering, while transmitted light relates to the extinction effect. For instance, a 20 nm Au NP primarily absorbs light due to its size-related absorption efficiency, while a larger 40 nm Au NP demonstrates a combination of absorption and scattering phenomena. As the size of AuNPs increases further, such as to 80 nm, both absorption and scattering contributions become more pronounced and balanced.

The incident light is a combination of various wavelengths, which induces the LSPR effect through the coherent oscillatory displacement of electrons within the metal nanoparticles. This effect causes the nanoparticles to scatter and absorb specific wavelengths based on their size and material properties. The color perceived by the observer depends on the relative position of the light source and the observer [39, 40]. From the side, the observer sees only the scattered light, resulting in a color caused solely by scattering. In contrast, an observer aligned with the light source sees the transmitted light, influenced by both absorption and scattering effects. Thus, the color

of the colloidal nanoparticle solution in this scenario is determined by extinction. The TEM images and UV/Vis absorption of Au NPs with different sizes are shown in Figure 2.3a, the inserted picture represents the colors of the Au NPs.

In addition to the sizes of Au NPs, the shape of the Au NPs plays a crucial role in their SPR characteristics. According to Gan's theory, altering the shape from spherical to elongated or rod-like forms results in the splitting of the SPR band. This phenomenon generates distinct absorption peaks: a strong, longitudinal band in the near-infrared (NIR) region and a weaker, transverse band in the visible spectrum. The longitudinal band corresponds to electron oscillations along the longest axis of the nanoparticle, while the transverse band relates to oscillations perpendicular to this axis. This shape-dependent SPR behavior is crucial for applications requiring tunable optical properties, such as sensing and imaging technologies. Figure 2.3b depicts the TEM images and UV/Vis absorption of different shapes of Au NPs nanospheres, nanocubes, nanobranches, nanorods, nanobipyramids.

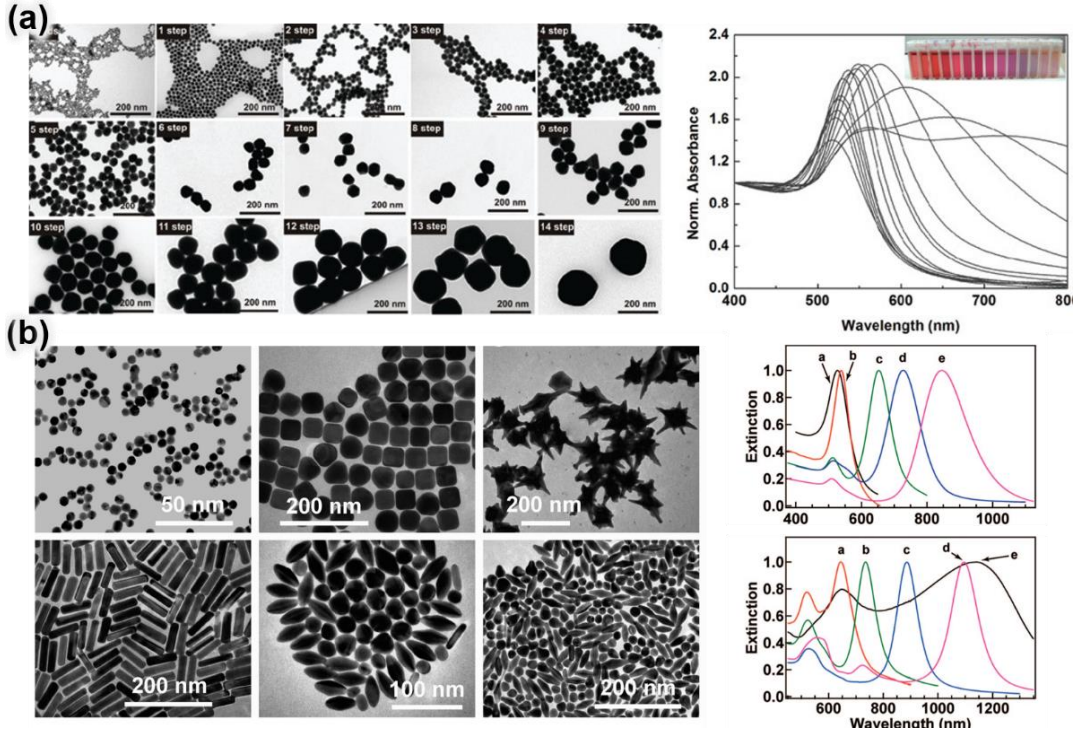

Figure 2.3. *(a) TEM images and UV/Vis absorption of Au NPs with particle size increases from 8.4 to 180.5 nm, representative. (b) TEM images and UV/Vis absorption of Au NPs with different shapes and sizes: nanospheres, nanocubes, nanobranches, nanorods, nanobipyramids [40]. Copyright 2008 American Chemical Society.*

The electronic structure of Au NPs significantly influences their photothermal properties, particularly relevant in photothermal therapy [41]. AuNPs with sizes around 2 nm exhibit a notable extinction coefficient, indicating high efficiency in converting incident light into heat. This attribute is exploited in biomedical applications where localized heating can selectively destroy cancer cells or trigger drug release from nanocarriers. The magnetic properties of AuNPs vary with size and surface chemistry [42]. Bulk gold is diamagnetic, but at the nanoscale, especially when surface ligands (such as thiolates) are present, Au NPs can exhibit ferromagnetic-like behavior [8]. This transition to ferromagnetic properties is attributed to surface effects and changes in electron confinement within the nanoparticle. Such magnetic characteristics are significant in applications ranging from magnetic separation to data storage and biomedical imaging.

Overall, the size and shape of Au NPs intricately dictate their optical, electronic, and magnetic properties. These properties are fundamental to understanding and exploiting the unique behaviors of Au NPs in various applications.

2.2.2 Synthesis of Au NPs

Nucleation of the NPs

During the synthesis of Au NPs in a liquid medium, the occurrence of nucleation refers to the scenario where initial nuclei arise uniformly throughout a supersaturated solution. The nucleation is understood as a thermodynamic process, an idea that traces back to the classical nucleation theory proposed by Gibbs in the 1870s [43]. According to this theory, the change in Gibbs free energy for homogeneous nucleation, ΔG, is given by a balance between volumetric and surface contributions to the energy:

$$\Delta G = \frac{4}{3}\pi r^3 \Delta G_v + 4\pi r^2 \gamma \tag{2.12}$$

where r is the radius of the nucleus, ΔG_v is the change in free energy per unit volume, and γ is the surface free energy per unit area.

The change in free energy per unit volume, ΔG_v, is influenced by the degree of supersaturation S and is described by:

$$\Delta G_v = \frac{-k_B T \ln(S)}{v} \tag{2.13}$$

with k_B being Boltzmann's constant, T is the absolute temperature, and S is the supersaturation ratio.

Because the surface free energy is always positive and the crystal free energy is always negative, there is a point where the free energy reaches a maximum as a nucleus forms. The energy barrier for nucleation, ΔG^*, representing the maximum in Gibbs free energy during the nucleation process, is described by:

$$\Delta G^* = \frac{4}{3}\pi\gamma r^{*2} \tag{2.14}$$

the critical radius r^* for a nucleus, beyond which growth will lead to a decrease in free energy and thus spontaneous nucleation, is given by the relation:

$$r^* = \frac{-2\gamma}{\Delta G_v} = \frac{2\gamma v}{k_B T ln\,(S)} \tag{2.15}$$

where v is the molar volume of the crystal. This critical radius corresponds to the minimum size at which a particle can survive in solution without being redissolved. If the nucleus is smaller than this critical size, creating a new surface demands energy and a higher chemical potential. Conversely, once the nucleus exceeds the critical size, any further increase in its radius reduces the free energy change until it reaches a stable state.

Seed-mediated growth

When particles exceed a certain critical radius, they will continue to form and grow, whereas particles below this radius will redissolve [44]. However, this alone does not account for the variations in particle sizes during growth. A phenomenon known as Ostwald ripening, which involves size focusing, can be considered by examining diffusion-controlled growth. Commonly, a tetrachloroauric acid ($HAuCl_4$) solution serves as the starting point, acting as a soluble precursor that must be reduced from its gold (III) state to elemental gold to form the nanoparticle structure.

As is shown in Figure 2.4, the synthesis process is divided into three discrete stages, structured to differentiate between homogeneous and heterogeneous nucleation events. Figure 2.4a shows the heterogeneous nucleation, the attachment of single atoms to preexisting particles or Wulff-seeds, is contrasted with homogeneous nucleation, where multiple atoms coalesce independently of any seeds. Since heterogeneous nucleation surmounts a lesser energy barrier-rendering it preferable when seeds are accessible, it is the favored process, ideally yielding a consistent distribution of monodisperse particles.

During synthesis, it is imperative to inhibit nanoparticle aggregation, driven by a thermodynamic inclination towards a minimal surface area to volume ratio. To

counteract this, stabilizing agents are used as is shown in Figures 2.4b and c. Surfactants such as polyvinylpyrrolidone (PVP) or cetyltrimethylammonium bromide/chlorid (CTAB/C) are utilized to form an electrostatic barrier around each particle, thereby precluding coalescence. The choice of the surfactant, in combination with the potency of the reducing agent, critically influences the attributes of the resultant Au NPs.

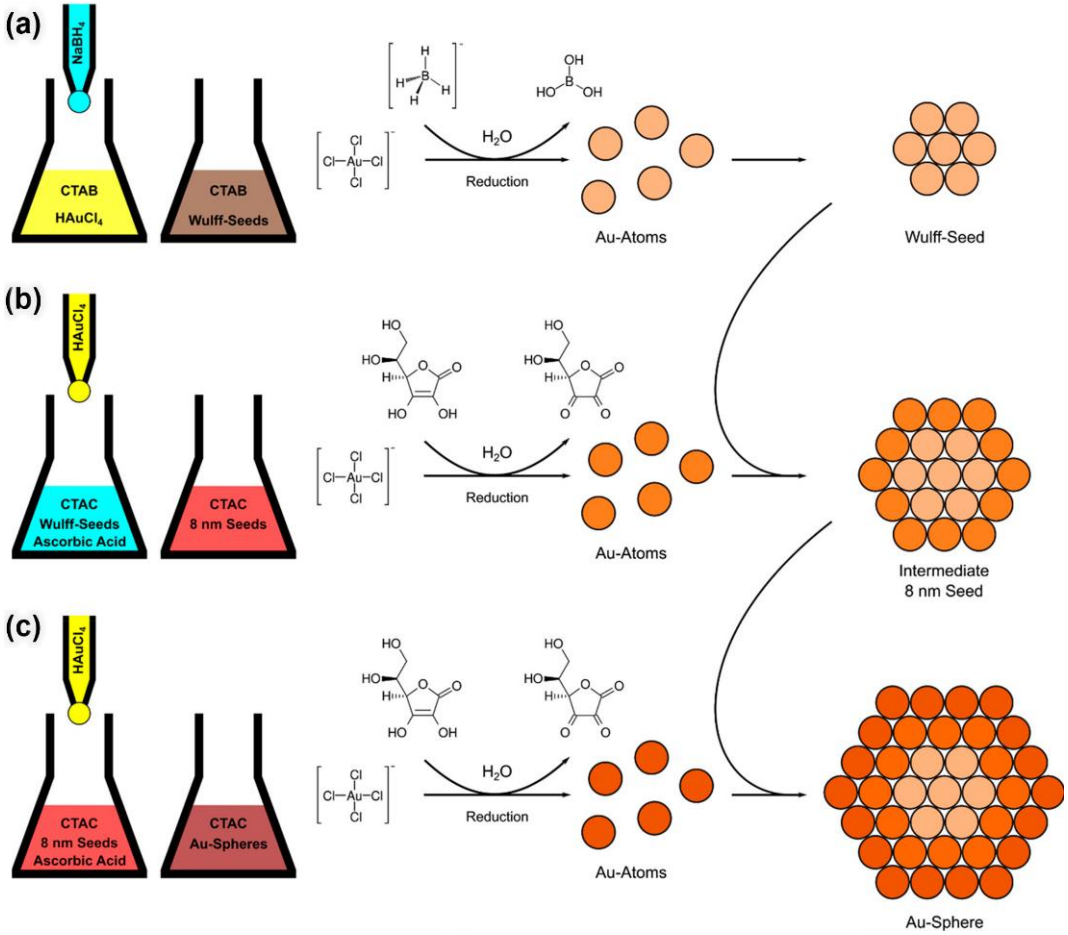

Figure 2.4. *An illustration overview of the synthesis process for Au NSs. (a) Initial Wulff-seeds are produced by quickly reducing the gold precursor, HAuCl4, with NaBH4, resulting in the formation of gold atoms within a solution stabilized by CTAB. These seeds are then grown incrementally, (b) firstly to seeds of 8 nm in size, and (c) subsequently to Au NSs of the target size of demands, by gently reducing additional gold precursor introduced into the system with ascorbic acid. Note that surfactant molecules are not depicted for the sake of simplicity [39]. Copyright 2021 American Chemical Society.*

The energy threshold for heterogeneous nucleation is substantially lower than that for homogeneous nucleation, particularly when additional surface energy aspects are considered [45]. This variance is largely due to the seed presence, which alters the system energy landscape. In heterogeneous nucleation, monomers coalesce on a pre-synthesized seed, creating a stable platform for further metallic growth and forming solid-state heterointerfaces. The calculation of surface energy encompasses the energies of the interfaces between the seed and the surrounding medium (γ_1), the secondary material (γ_2), and the interface between the seed and the expanding material (γ_{12}).

The equilibrium contact angle (θ) between the nucleus and the seed is described by Young's equation, which equates the interfacial tensions. This relation assists in determining the energy barrier for heterogeneous nucleation (ΔG_{hetero}), which is a function of θ and the energy barrier for homogeneous nucleation (ΔG_{homo}):

$$\gamma_{12} = \gamma_1 + \gamma_2 \cos(\theta) \tag{2.16}$$

$$\Delta G_{\text{hetero}} = \Delta G_{\text{homo}} f(\theta) \tag{2.17}$$

here, $f(\theta)$, the wetting function, lies between 0 and 1, indicating that the energy barrier for heterogeneous nucleation is invariably lower than for homogeneous nucleation when stable nucleation sites are available. This property confirms the inherent advantage of heterogeneous nucleation, allowing for its occurrence under less stringent synthesis conditions, such as lower temperatures and decreased monomer concentrations, thereby enhancing the precision and control within nanoparticle synthesis.

2.2.3 Self-assembly of Au NPs

Self-assembly with electrostatic adsorption method

The bottom-up approach enables mass production of nanoparticles and allows for the assembly of tunable and flexible encoding platforms. Common methods for bottom-up fabrication of colloidal nanoparticle monolayers on substrates include capillary forces, DNA binding, and electrostatic interactions [46]. The self-assembly of Au NPs on a substrate is primarily determined by the electrostatic interactions between the particles and the interactions between the particles and the substrate.

The distance between two particles can be described by the Helmholtz and Gouy-Chapman model [47]. This model relates the distance between two neighboring colloidal nanoparticles in a free state to the electric double-layer thickness and is given by the following formula:

$$\kappa = \sqrt{\frac{4\pi e^2}{\epsilon k_B T} \sum_i n_i Z_i^2} \tag{2.18}$$

here, e is the electron charge, ϵ is the absolute dielectric constant, k_B is the Boltzmann constant, T is the temperature, n_i is the ionic concentration, and Z_i is the ionic valence. The effective diameter of the particle is the sum of the double-layer thickness and the diameter of the rigid core, expressed as:

$$D = d + \frac{2}{\kappa} \tag{2.19}$$

However, this relationship only considers particles in a free state. The spacing between neighboring nanoparticles on a charged surface is described by equation 2.20, which accounts for the electrostatic balance between the net charge of the nanoparticles and the substrate surface:

$$d = \sqrt{\frac{4\beta(n_i, r)}{\sqrt{3}\int_{\phi_s}^{\phi_e} \sinh\left(\frac{ze\phi}{k_B T}\right) d\phi}} \tag{2.20}$$

here, r is the particle radius, ϕ_s is the surface potential of the substrate, The spacing between nanoparticles is proportional to the core diameter of the nanoparticles. This equation also indicates that d is inversely proportional to ϕ_s.

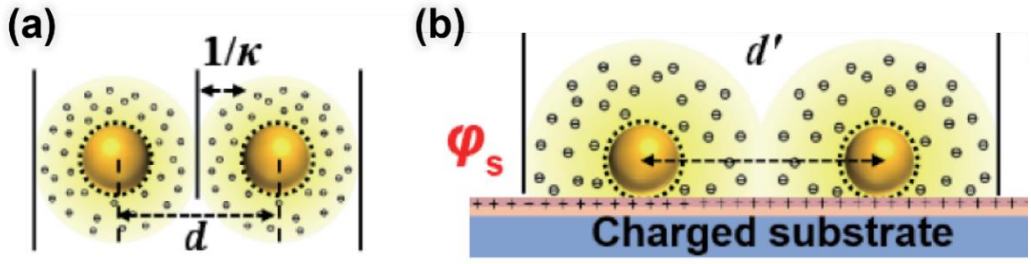

Figure 2.5. *Schematic diagram of the inter-particle spacing (a) in the colloidal system and (b) on the charged substrate [47]. Copyright 2022 Springer Nature.*

Therefore, the inter-particle spacing can be increased by weakening the substrate surface potential. The synthesized Au NPs can be surface-coated with ligands during the synthesis process. In this thesis, CTAB is used as the surface-coating material.

Chapter 5 will elaborate on the self-assembly process of Au NPs. The inter-particle spacing of Au NPs in both colloidal system and on the charged substrate surface is depicted in Figure 2.5.

Self-assembly with phase interfacial method

The assembly of Au NPs into two- or three-dimensional structures has attracted considerable attention on account of their unique electronic and optical properties. The main concept of phase interfacial self-assembly is that Au NPs are trapped at the interface between two immiscible phases, where they form an organized layer due to interfacial phenomena such as electrostatic interactions, capillary action, and van der Waals forces [48]. The adsorption of nanoparticles at the interface can be affected by factors such as the nanoparticle size and the contact angle of the particles at the oil-water interface. Recently, various methods have been developed to enhance the interfacial capture and self-assembly of nanoparticles at the oil-water interface [48, 49]. It has been found that simple heating or the addition of water- and oil-miscible solvents such as acetone or ethanol can assemble hydrophilic nanoparticles at the interface. The self-assembly of nanoparticles at the oil-water interface can also be enhanced and controlled by adjusting other parameters such as particle surface properties, the use of surfactants, pH, ionic strength of the aqueous phase, and concentrations of nanoparticles and polymer ligands.

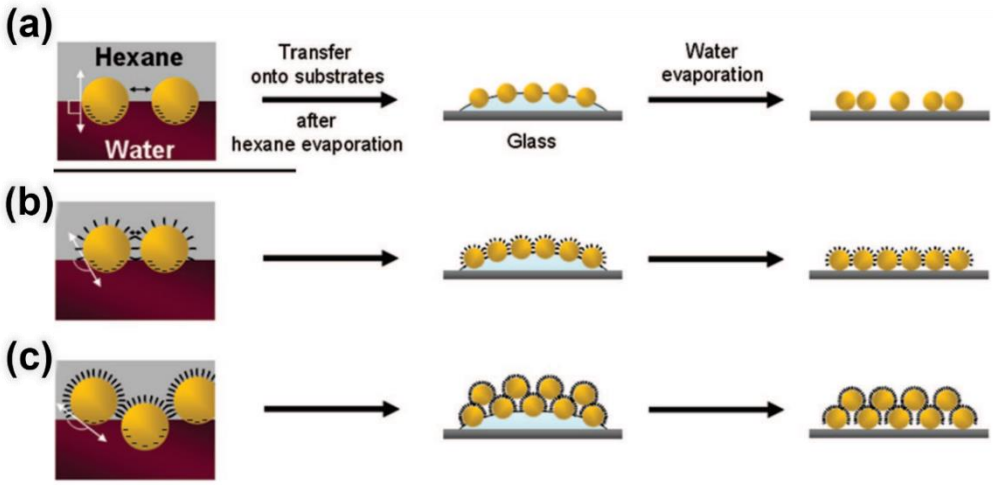

Figure 2.6. *Schematic representation of the NP film formation. (a) NP film formation at a water/hexane interface and its transfer onto substrates after hexane evaporation. (b) As in scheme (a) except the presence of an optimum amount of 1-dodecanethiols in a hexane phase for nanoparticulate film. (c) As in scheme (a) except the presence of the extra amount of 1-dodecanethiols in a hexane phase. Copyright 2018 The Royal Society of Chemistry.*

Figure 2.6 shows a schematic diagram of the self-assembly of Au NPs through the water/hexane phase interface. When a layer of hexane is added to the synthesized Au NP solution, two separate phases are formed due to the immiscibility of water (a polar solvent) and hexane (a nonpolar alkane). The addition of ethanol causes a tilt in the surface charge of the Au NPs in suspension due to the competitive adsorption of ethanol molecules. Consequently, the Au NPs are immediately pulled into the interface between water and hexane to form a high-density gold monolayer without aggregation or multilayer formation.

2.3 Au NPs in colloidal quantum dot (CQD) photodetector

Free electrons on the surface of a plasmonic antenna will collectively oscillate when incident light of a specific wavelength interacts with Au NPs. This interaction leads to a significant enhancement of the electric field surrounding the plasmonic nanostructure and the generation of hot electrons induced by plasmons. These hot electrons subsequently flow through the metal nanostructure and can release energy due to flexible aggregation in the metal film. When a Schottky barrier is formed between a semiconductor and the plasmonic nanostructure, and the hot electrons possess sufficient energy to surpass this barrier, they can be injected into the semiconductor conduction band [50, 51]. This process can generate a current for photodetection below the semiconductor band edge, thereby extending the detection range of the semiconductor to wavelengths it would otherwise be unable to absorb.

In Au NPs hot carrier devices, metal conduction electrons are excited electromagnetically to form plasmons, as illustrated in Figure 2.7. After excitation, scattering from other electrons and the nanoparticle surface causes individual plasmon electrons to lose their collective phase, resulting in the generation of "hot" carriers. These plasmonic hot carriers are often harnessed using the Schottky barrier between the semiconductor and the metal, which helps overcome their short lifetime, as shown in Figure 2.7b.

The semiconductor receives the hot carriers with energies exceeding the Schottky barrier, and the internal fields of the junction prevent the recombination of photoexcited electrons and holes after their transfer. If there is an energy band offset between the semiconductor and the metal, the hot carriers are maintained at higher energies. This energy band offset acts as an efficient filter, allowing the Schottky barrier to separate and store the energy of the hot carriers for later use. Moreover, plasmon oscillating electrons can be used to extract plasmonic hot carriers by scattering directly into the interface states before other intrinsic losses occur, as shown in Figure 2.7c.

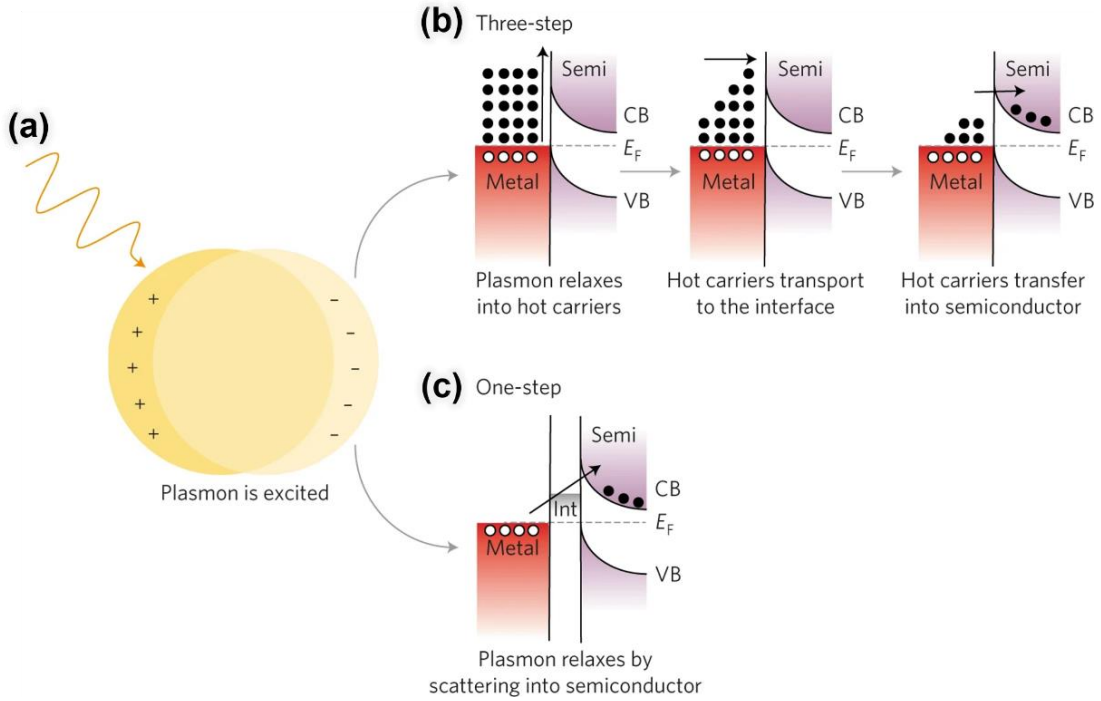

Figure 2.7. *Hot-carrier capture from a plasmonic nanoparticle. (a) A plasmon is the collective oscillation of conduction electrons during electromagnetic excitation. (b) When the oscillating electrons scatter and lose their collective phase, a hot-carrier distribution is created with energy up to the plasmon frequency above the Fermi level (EF). The hot carriers can transfer over a metal–semiconductor Schottky barrier, capturing and storing the energy of the plasmon in the semiconductor. (c) A plasmon can be de-excited by directly scattering the oscillating electrons into a semiconductor. This timescale is shorter than the time it takes for the plasmon energy to be lost to heat in the metal, and could therefore lead to higher extraction efficiencies [52]. Copyright 2017 Springer Nature.*

This type of plasmon damping is usually referred to as chemical interface damping and it dominates with small metal nanoparticles usually < 10 nm. This mechanism enhances the efficiency of hot carrier generation and enhance photodetection and energy conversion.

In recent years, colloidal quantum dots (CQDs) have garnered significant research interest due to their exceptional performance and promising application prospects [53, 54]. Their pronounced quantum confinement effects result in strong light-matter interactions and unique optical properties, most notably wide tunable band gaps and high absorption coefficients. Consequently, CQDs hold great potential as absorbers for low-cost detectors with adjustable spectral responses.

Additionally, the localized surface plasmon resonance (LSPR) characteristics of metal nanostructures can be tuned to efficiently convert incident light and strongly confine and enhance the electric field around the metal nanostructures. These properties of plasmonic antennas suggest their potential to directly enhance the sensitivity of sensors, as well as the detection capability and efficiency of photodetectors.

Therefore, incorporating Au NPs into CQD photodetectors is a promising strategy for improving device performance. This approach leverages the unique optical and electronic properties of both CQDs and Au NPs to create advanced photodetectors with superior sensitivity and efficiency [28, 55].

The hot electrons generated from surface plasmon decay in the active antenna can traverse the Schottky barrier and inject into the conduction band, thereby directly contributing to the photocurrent for photodetection in optical telecommunication regimes [56]. Photocurrent generation occurs when the photon energy is only slightly higher than the Schottky barrier height. It has been proposed and demonstrated that the spectral response of an active antenna-based device can be considered analogous to that of a Schottky diode incorporating a specific plasmon resonance [57].

For a Schottky diode, the photoresponse depends on the quantum transmission probability η_i of the carriers, which can be approximated by the modified Fowler equation:

$$\eta_i \approx \mathrm{C_F} \frac{(h\nu - q\phi_b)^2}{h\nu} \tag{2.21}$$

where C_F is the Fowler emission coefficient, $h\nu$ is the photon energy, and $q\phi_b$ is the Schottky barrier height. This equation allows for a preliminary approximation of the number of carriers with sufficient energy to overcome the barrier height and contribute to the photocurrent for a Schottky diode, even in the absence of a specific plasmon resonance.

When the Schottky junction is formed by plasmonic nanostructures, the photoresponsivity (R) of the active antenna-based device will exhibit a Fowler response (η_i) modified by the plasmonic absorption (A):

$$R = \eta_i A \tag{2.22}$$

Moreover, the spectral photocurrent and absorbance spectrum of the active optical antennas can be readily controlled by adjusting the dimensions and shapes of the NPs. This tunability allows for the optimization of device performance across different operational regimes.

2.4 Au NPs based bimetallic nanostructures

Bimetallic composite nanostructures, composed of two distinct metallic elements, have garnered significant scientific and technological interest due to their unique electronic, optical, catalytic, and photocatalytic properties, which are not observed in single metallic system [58-60]. The synergistic effects between the two metals in BMNs are anticipated to impart both novel characteristics and a combination of the properties inherent to each metal. Figure 2.8 shows the plasmonic bimetallic nanostructures and the components, configurations, properties, and applications.

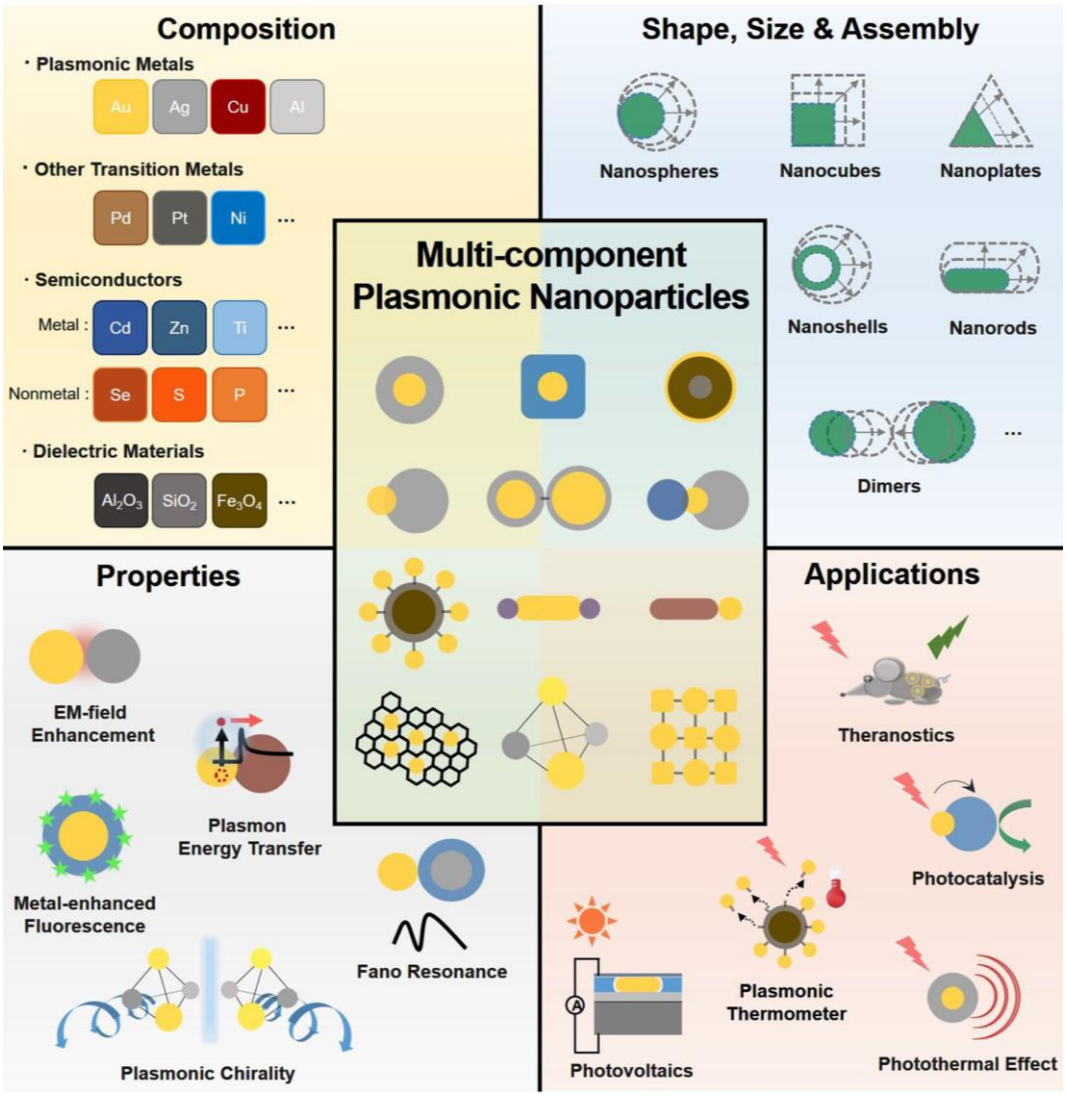

Figure 2.8. *Plasmonic bimetallic nanostructures and the components, configurations, properties, and applications [8]. Copyright 2019 American Chemical Society.*

The structural configuration of Au NPs based BMNs, dictated by the distribution pattern with an additional element, can appear as core-shell structures, random alloys, intermetallic compounds, or cluster-in-cluster formations [8]. The physicochemical properties of the resulting nanomaterials are substantially influenced by the size and shape of both single and bimetallic nanoparticles, which are determined by the specific synthesis conditions and fabrication methods used. Several chemical, physical, and hybrid fabrication strategies have been proposed and successfully implemented for the preparation of Au NPs based bimetallic nanostructures [61, 62]. These methods enable precise control over the composition, morphology, and distribution of the constituent metals, which is crucial for tailoring their properties for specific applications.

Chemical heterogeneous synthesis techniques, such as seed-mediated growth, co-precipitation, chemical reduction, and sol-gel methods, have been extensively utilized to fabricate Au NPs based bimetallic nanostructures [8]. These methods enable the fine-tuning of particle size, composition, and morphology by adjusting key reaction parameters such as temperature, pH, and precursor concentration. In addition, microemulsion and polyol synthesis offer a high degree of control over bimetallic nanoparticles shape and spatial distribution. Furthermore, hydrothermal and solvothermal synthesis methods use high-pressure and high-temperature conditions to synthesize bimetallic nanostructures, which are particularly useful for creating highly crystalline and thermodynamically stable nanoparticles [8, 63]. Electrochemical synthesis methods offer the ability to finely tune the composition and size of BMNs through the control of electrochemical parameters. This approach is advantageous for producing uniform coatings and films with precise thicknesses.

In addition to chemical methods, various physical deposition techniques offer alternative routes for fabricating bimetallic nanostructures [23, 64, 65]. These methods, including sputtering, thermal evaporation, atomic layer deposition, and laser ablation, involve the physical transfer of atoms from a target material to a substrate, enabling the formation of thin films or layered structures with precise control over thickness and composition. Physical deposition methods offer the ability to create high-quality, uniform, and precisely controlled bimetallic nanostructures.

Hybrid fabrication strategies combine chemical and physical approaches to leverage the advantages of both. For instance, electrochemical deposition can be used in conjunction with chemical reduction techniques to create nanostructures with enhanced uniformity and improved catalytic properties. Similarly, template-assisted methods, which involve the use of pre-formed templates or scaffolds, can be combined with chemical deposition techniques to produce complex nanostructures with controlled geometries. In the present thesis, Au/Ag BMNs are fabricated via a hybrid technique by sputter Ag film on a self-assembled Au NPs template, more details will be elaborated in Chapter 6.

2.5 X-ray scattering

Within the context of this thesis, X-ray scattering method are used to investigate the internal morphology and crystalline architectures of films, providing statistically significant insights. The basic principles of scattering techniques are elucidated in Section 2.5.1. Subsequently, detailed discussions on Grazing-Incidence Small-Angle X-ray Scattering (GISAXS) and Grazing-Incidence Wide-Angle X-ray Scattering (GIWAXS) are elaborated in Sections 2.5.2 and 2.5.3, respectively.

2.5.1 Basic principles

The electric field vector, represented as $\vec{E}(\vec{r})$, is expressed as a function contingent upon the position vector $\vec{r}$, with $\vec{\mathrm{r}} = (\mathrm{x}, \mathrm{y}, \mathrm{z})$ delineated as follows [66]:

$$\vec{E}(\vec{r}) = \vec{E}_0 \exp\left(i\vec{k}_i \cdot \vec{r}\right) \tag{2.23}$$

In this context, $\vec{E}_0$ denotes the amplitude of the electric field, which is indicated by the polarization characteristics of the wave. The term $\vec{k}_i$ represents the wave vector, a fundamental concept that characterizes the direction of wave propagation and its spatial frequency.

The magnitude of the wave vector, $\left|\vec{k}_i\right|$, is quantitatively expressed through the wave number k or alternatively, through the wavelength λ, as follows:

$$\left|\vec{k}_i\right| = k = \frac{2\pi}{\lambda} \tag{2.24}$$

this equation establishes a direct relationship between the wave vector magnitude and the physical parameters of the wave, such as its wavelength [67]. The wave number k, being equivalent to 2π divided by the wavelength λ, serves as a crucial parameter in understanding the wave propagation characteristics and its interaction with the medium.

The scattering vector, denoted as $\vec{q}$, plays a crucial role in the analysis of scattering phenomena, capturing the discrepancy between the incident wave vector, $\vec{k}_i$, and the scattered wave vector, $\vec{k}_f$. This vectorial differentiation expressed by the equation:

$$\vec{q} = \vec{k}_f - \vec{k}_i \tag{2.25}$$

The scattering vector $\vec{q}$ is essential for revealing the structural and dynamic characteristics of the sample under study, indicating the modifications in the wave

trajectory resultant from the scattering process.

The scattering length density (SLD) quantifies the capacity of a material to diffract or scatter incoming radiation. It plays a crucial role in highlighting the variations in scattering attributes both within different areas of a single material and across various materials [68]. Determination of the SLD becomes feasible with knowledge of the material chemical makeup and its average electron density, ρ_e. The SLD for the X-ray measurement is mathematically defined by the formula:

$$\text{SLD} = \frac{n_e \rho_e N_A r_e}{M_w} \tag{2.26}$$

where n_e symbolizes the total number of electrons per molecule, ρ_e represents the electron density, N_A is the Avogadro constant, indicating the number of constituent particles per mole of a substance, and M_w denotes the molar mass of the material. This formulation underscores the relationship between the SLD and fundamental physical constants, as well as the material-specific properties such as electron density and molar mass.

By linking these parameters, the SLD effectively measures how a material interacts with radiation, offering insights into its structural and compositional characteristics that influence scattering phenomena.

Bulk specimens have been extensively investigated using transmission geometry due to their substantial scattering volumes [69]. In contrast, thin-film samples present a challenge as their significantly smaller scattering volumes lead to weak scattering signals. To surmount this issue, reflection geometry using grazing incidence angles is utilized. This method enhances the effective scattering volume, thereby facilitating access to the internal structures of thin films. Utilizing grazing angles not only amplifies the scattering signal but also enables detailed exploration of the film intricate internal architectures, providing valuable insights into their structural characteristics.

When the incidence angle is below the critical angle ($\alpha_i < \alpha_c$), total reflection yielding primarily surface-related insights. To probe internal structures, it is necessary to use an incidence angle that is lower with critical angle. Yoneda's work illustrates the highest scattering intensity at the critical angle, attributed to a peak in the Fresnel coefficients [70]. This phenomenon, in the Yoneda region, allows for the extraction of material-specific data, underscoring the critical angle dependence on the material inherent properties.

For hard X-rays ($E > 5$ keV), where the refractive index is below one, the X-ray beam undergoes reflection at the juncture between a denser medium and a less dense medium. This reflective behavior adheres to Snell’s law, which is mathematically formulated as:

$$n_0 \cos(\alpha_i) = n \cos(\alpha_t) \tag{2.27}$$

the incidence angle, denoted by α_i, is defined as the angle formed between an incoming wave and the perpendicular line to the boundary separating two distinct media. The refractive index of the medium through which the wave travels is represented by n, while n_0 indicates the refractive index of the atmosphere enveloping the initial medium, typically considered the incident medium. The angle of transmission or refraction, labeled as α_t, characterizes the wave direction of travel within the second medium, measured in relation to the normal at the interface as well.

When the angle of incidence equals the critical angle $\alpha_i = \alpha_c$, and the angle of transmission is zero $\alpha_t = 0$, assuming air is the incident medium where $n_0 = 1$, the equation is accordingly simplified can be written as:

$$\cos(\alpha_c) = n = 1 - \frac{\lambda^2}{2\pi} r_e \rho_e = 1 - \frac{\lambda^2}{2\pi} \mathrm{SLD} \tag{2.28}$$

When applying the small angle approximation according to the Taylor series where α_c is close to 0, the equation simplifies to:

$$\cos(\alpha_c) \approx 1 - \frac{\alpha_c^2}{2} \tag{2.29}$$

An approximation for the critical angle in terms of the SLD is then derived, linking it directly with the physical and optical properties of the material:

$$\alpha_c \approx \sqrt{2\delta} = \lambda \sqrt{\frac{\mathrm{SLD}}{\pi}} \tag{2.30}$$

This set of equations enables the calculation of the critical angle based on the known properties of the material and the incident radiation wavelength λ. The approximation of α_c underscores the significance of the material SLD in determining how it interacts with radiation, especially useful for characterizing thin films and interfaces through scattering techniques.

2.5.2 Grazing-incidence small-angle X-ray scattering

Grazing-incidence small-angle X-ray scattering (GISAXS) offers a profound method to probe both the surface and subsurface morphologies of thin films, effectively mapping structures across a substantial length scale that spans from the nanometer to the micrometer range. The technique is particularly advantageous when dealing with thin films due to the minimal quantity of material present for analysis. In GISAXS, a very shallow angle of incidence, typically $\alpha_i < 1^\circ$, is used. This small angle significantly increases the footprint of the X-ray beam upon the film, thereby

enhancing the interaction volume. The footprint length in the direction of the beam, l, is given by the formula:

$$l = \frac{h}{\tan(\alpha_i)} \tag{2.31}$$

where h represents the vertical dimension of the incident beam. For instance, with an incidence angle of $\alpha_i = 0.4°$ and an X-ray beam size of $20 \times 30\ \mu m^2$, the area of illumination is expanded by more than two orders of magnitude. This amplification is critical for achieving a detectable scattering signal from the film, allowing for detailed structural analysis at large length scales.

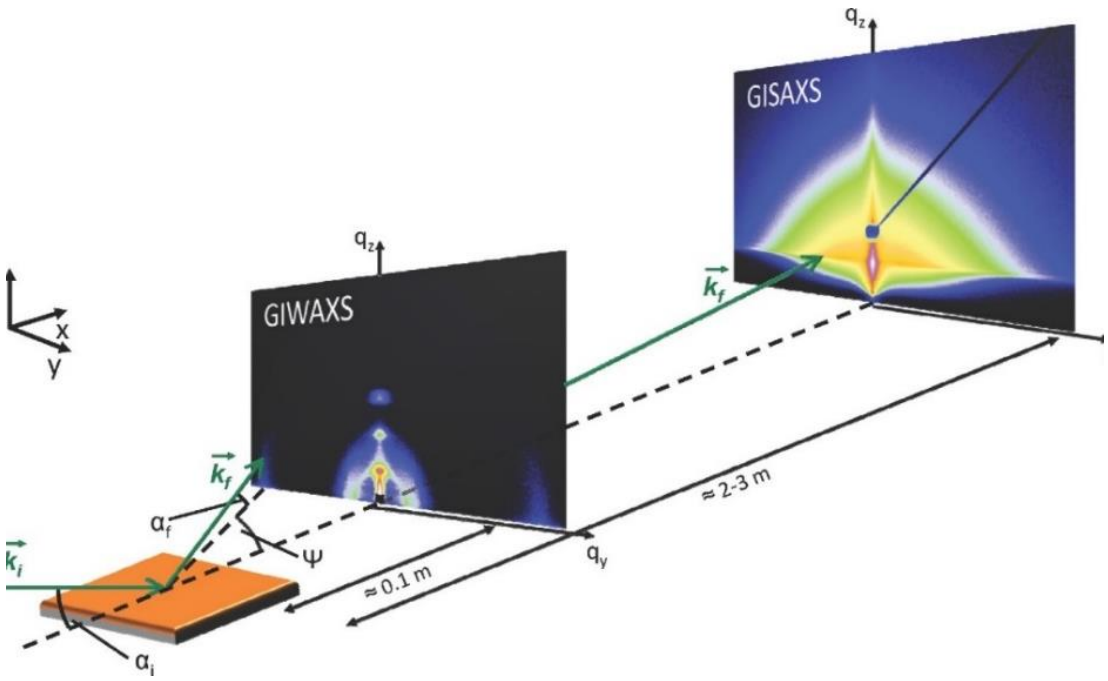

Figure 2.9. *Illustration of GISAXS/GIWAXS geometry. Copyright 2014 John Wiley & Sons.*

The basic scattering geometry for GISAXS is shown in Figure 2.9. A monochromatic X-ray beam characterized by the wave vector $\vec{k}_i$ impinges upon the sample surface at a very shallow angle of incidence, α_i, relative to the surface plane. Within an established Cartesian coordinate system, the z-axis is defined as perpendicular to the surface plane, the x-axis runs parallel to the surface in the direction of the beam, and the y-axis is orthogonal to both, forming a right-handed coordinate system.

X-rays scatter in various directions, defined by the wave vector $\vec{k}_f$, with the scattering characterized by angles ψ (azimuthal angle) and α_f (out-of-plane angle) relative to the surface. These interactions with electron density fluctuations across the illuminated

area of the surface result in a scattered wave. The scattering vector $\vec{q}$, is expressed as:

$$\vec{q} = (q_x, q_y, q_z) = \vec{k}_f - \vec{k}_i = \frac{2\pi}{\lambda}\begin{pmatrix}\cos(\alpha_f)\cos(\psi) - \cos(\alpha_i)\\ \cos(\alpha_f)\sin(\psi)\\ \sin(\alpha_f) + \sin(\alpha_i)\end{pmatrix} \quad (2.32)$$

The scattering intensity measured at low angles, typically just a few degrees, is registered using a two-dimensional detector, which discloses the sample lateral structures that span from several to hundreds of nanometers. This detector is strategically positioned along the x-axis and is placed at a considerable sample-to-detector distance, ranging from 2 to 3 m.

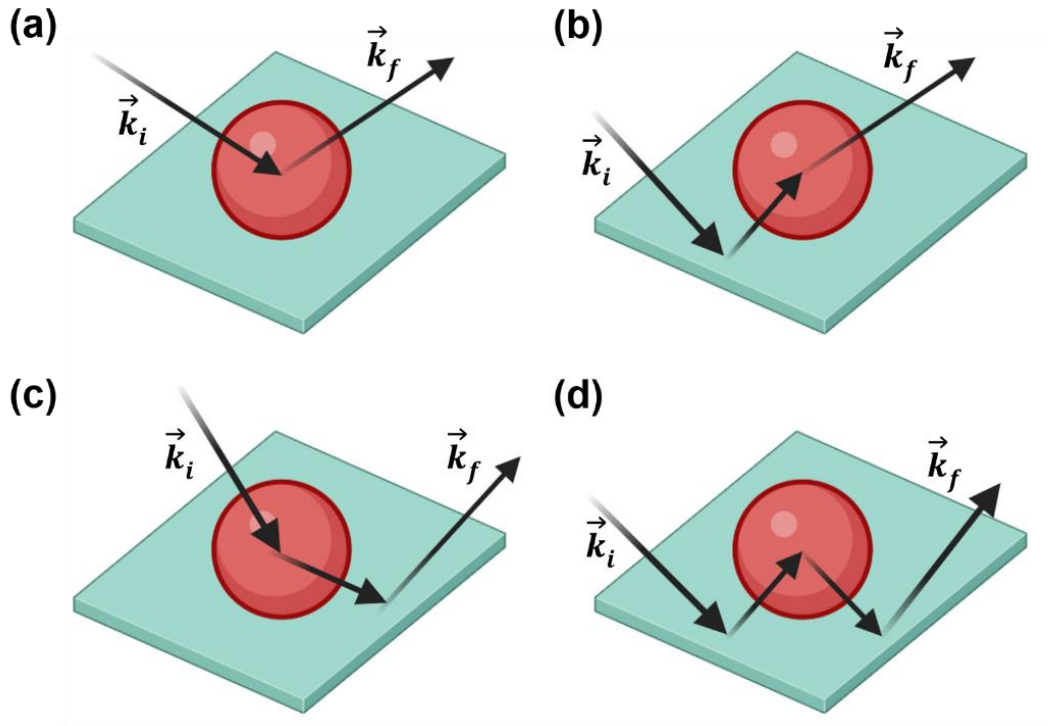

Figure 2.10. *Schematic representation of the DWBA involved four terms in the scattering by a supported object: (a) directly scattered beam (BA) with (b) first reflected and then scattered (c) first scattered and then reflected (d) reflected-scattered-reflected. Illustration created with BioRender.com*

Under grazing incidence, reflection and refraction occur at both the sample and substrate interfaces. Diffuse scattering is generally analyzed using the distorted-wave Born approximation (DWBA) framework. Within the DWBA, when considering an object on a substrate, four terms that influence scattering are considered. As illustrated in Figure 2.10, these include the standard scattering event, reflection followed by scattering, scattering followed by reflection, and reflection followed by scattering with a subsequent second reflection. The first term is the Born approximation (BA),

where the incoming beam is scattered directly by the object. The second term describes the incident beam is first reflected by the substrate and then scattered by the object. In the third term, the incoming beam is initially scattered by the object and subsequently reflected by the substrate. The fourth term represents reflection at the interface, followed by scattering at the object, and then another reflection.

Data analysis for GISAXS can be conducted by using specialized software to model the entire scattering pattern, or by focusing on a horizontal line cut at the material critical angle [71]. For quantitative analysis in this thesis, the effective interface approximation (EIA) is employed for further simplification. According to the EIA, scattering objects are assumed to have only a single distinct surface, focusing solely on lateral interactions and allowing the decoupling of the radius and height of the scattering objects. Since the size of actual scattering objects varies around a mean value, several approximations are necessary. For polydisperse domains, an effective average form factor is introduced using the decoupling approximation (DA, Figure 2.11a) or the local monodisperse approximation (LMA, Figure 2.11b). In this thesis, a model based on the LMA is used to describe GISAXS data (Figure 2.11c), assuming that the structures are standing cylinders with three different sizes co-existing in the thin film. Additionally, structures of similar sizes are assumed to form locally nearly monodisperse domains.

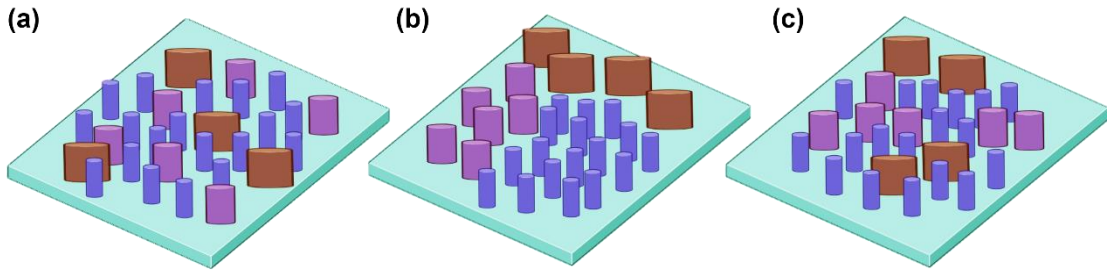

Figure 2.11. *Illustration of common approximation models for scattering factors. (a) decoupling approximation (DA), (b) local monodisperse approximation (LMA), and (c) the model assumed in this thesis based on the LMA. Illustration created with BioRender.com*

The comprehensive scattering function is conceptualized as an incoherent sum of distinct scattering events from various types of scattering entities, each of which can be analyzed separately. For a monodisperse structures, the diffuse scattering factor, which accounts for the spread of scattered intensity, can be estimated approximated by:

$$P(\vec{q}) \propto N|F(\vec{q})|^2|S(\vec{q})| \tag{2.33}$$

where N is the number of scattering entities within the sample, $F(\vec{q})$ is the form factor,

and $S(\vec{q})$ is the structure factor. In practical experiments, scattering objects often exhibit a range of dimensions rather than a uniform size, leading to polydispersity within the system. When dealing with such a polydisperse system, where the scattering objects share the same shape but differ in size, the relevant equations must be adapted to incorporate an effective average form factor.

2.5.3 Grazing-incidence wide-angle X-ray scattering

Grazing incidence wide-angle X-ray scattering (GIWAXS) is a powerful technique to investigate the crystalline structures of the film [70]. As is shown in Figure 2.9, the setup for a GIWAXS experiment shares similarities with that of GISAXS, though it typically involves a shorter SDD, ranging from 0.1 to 0.2 m. This adjustment in the experimental setup enables the detection of scattered signals at large exit angles. Such a configuration is crucial for accessing structural data at the sub-nanometer level, offering insights into the atomic arrangement within the material.

The scattering patterns observed are primarily governed by the periodicity of the crystal lattice. Within these crystals, individual atoms, ions, or molecules serve as scattering centers and are arranged periodically. Constructive interference occurs when the waves scattered from each plane are in phase, leading to amplified intensity. This happens when the path length difference between the waves matches an integer multiple of the X-ray wavelength. The condition for constructive interference and the resulting intense scattering peaks is described mathematically by Bragg's equation, which relates the spacing between planes in a crystal lattice, denoted as d_{hkl}, with the wavelength of the incident X-rays λ, the order of the reflection n, and the angle of incidence θ:

$$d_{hkl} = \frac{n\lambda}{2\sin\ \theta} \tag{2.34}$$

The Laue condition generalizes Bragg's law to three dimensions, offering a criterion for constructive interference that occurs when the change in the wave vector $\Delta\vec{k}$ is equivalent to a reciprocal lattice vector $\vec{Q}$ represented as:

$$\Delta\vec{k} = \vec{k}_f - \vec{k}_i = \vec{q} = \vec{Q} \tag{2.35}$$

and

$$\vec{Q} = h\vec{a}_1 + k\vec{a}_2 + l\vec{a}_3 \tag{2.36}$$

where $\vec{a}_1$, $\vec{a}_2$, and $\vec{a}_3$ are the reciprocal lattice vectors, and h, k, l are the Miller indices corresponding to the planes in the crystal lattice.

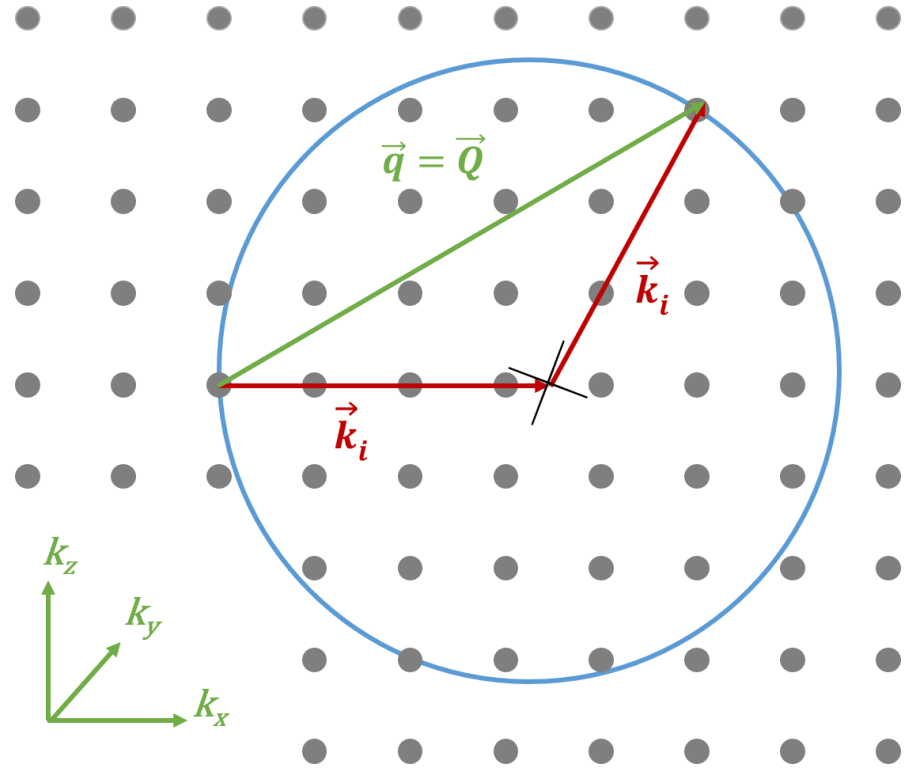

Figure 2.12. *Schematic illustration of the Ewald sphere. Diffraction patterns occur when the Ewald sphere touches a reciprocal lattice point.*

As is shown in Figure 2.12, the reciprocal lattice is conceptually the Fourier transform of the real-space crystal lattice and comprises all possible wave vectors that result in diffraction. A scattering signal is detected when the Laue condition is met, signifying that the incident wave vector $\vec{k}_i$ has been diffracted into the final wave vector $\vec{k}_f$ by the crystal lattice. An incoming beam interacts with a scatterer in real space, the complete set of all possible incident and scattered wave vectors ($\vec{k}_i$ and $\vec{k}_f$) forms a geometric locus known as the Ewald sphere. When a point in the reciprocal lattice coincides with the surface of this sphere, diffraction peaks become observable. Through GIWAXS, these Bragg peaks enable the determination of key crystallographic parameters such as lattice spacing, crystallite size, and orientation. Additionally, the degree of crystallinity within the sample, which correlates with the intensity of the scattered signal, can be assessed.

3 Characterization and analytical methods

This chapter describes various techniques used to characterize hybrid plasmonic nanostructures. Section 3.1 covers structure characterization, including both real- and reciprocal-space imaging methods for investigating the hybrid structures. Spectroscopic characterization techniques are detailed in Section 3.2. Section 3.3 discusses the basic principles of ultraviolet/visible light (UV/Vis) spectroscopy, dynamic light scattering (DLS), photoluminescence (PL) spectroscopy, and Raman spectroscopy measurements. Photodetector characterization methods are elaborated in Section 3.4. Finally, Section 3.5 focuses on the simulation of 2D grazing incidence small-angle X-ray scattering (GISAXS) patterns.

3.1 Structural characterizations

3.1.1 Scanning electron microscopy

Scanning electron microscopy (SEM) is a powerful technique capable of providing both topographic and material-sensitive information about conductive thin films at a sub-nanometer scale. However, the resolution of SEM is ultimately constrained by the wavelength of the beam used to examine the sample surface. According to the principle of particle-wave duality introduced by De Broglie, electrons exhibit a shorter wavelength compared to photons at a given energy level. Consequently, SEM offers a significantly enhanced resolution compared to classical optical microscopy, often by several orders of magnitude.

The schematic and operational principles of a typical SEM instrument are depicted in Figure 3.1. Generally, SEM operate by emitting an electron beam from an electron gun, typically equipped with either a tungsten filament cathode or a lanthanum hexaboride cathode. These electrons are accelerated towards an anode, passing

through a central aperture within it at a consistent energy level. This approach is preferred for generating high-quality SEM images due to its ability to provide a high electron flux, precise kinetic energy control, and the option to operate at relatively low acceleration voltages, typically 5 keV or less. Electromagnetic lenses and apertures play a crucial role in regulating the beam size and focus, while scan coils accurately position the beam on the sample surface. Various detectors, including backscattered electron (BSE), secondary electron (SE), and X-ray detectors, are utilized to capture signals resulting from the interaction between the electron beam and the sample.

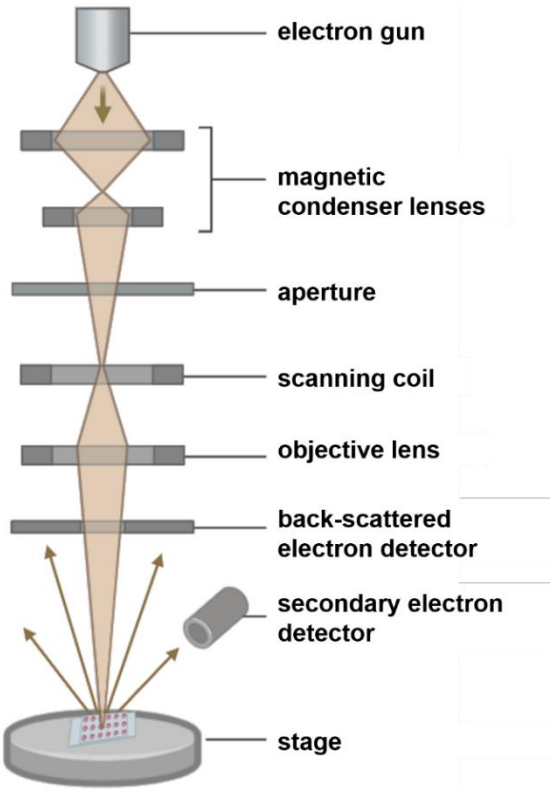

Figure 3.1. *Schematic illustration of a Scanning Electron Microscope. Illustration created with BioRender.com.*

The energy of the electron beam generated typically ranges from 0.2 keV to 40 keV. Using two magnetic condenser lenses, the electron beam is focused to a spot measuring approximately 0.4 nm to 5 nm in diameter, allowing it to scan the sample surface over a rectangular area. Due to their low energy levels, these electrons penetrate only a shallow depth into the sample, making SEM particularly effective for obtaining surface-sensitive information. Structures protruding from the sample surface often appear brighter in SEM images due to the reduced working distance. However, it is important to note that brightness levels can also be influenced by factors such as the composition of the material being investigated, providing additional insights into surface topography.

Additionally, the intensity of the backscattered electron signal is closely linked to the atomic number of the sample. Consequently, backscattered electron signals, along with characteristic X-rays, are commonly used to analyze the distribution of various elements within the sample. Therefore, energy-dispersive X-ray (EDX) spectroscopy can be conducted to further analyze the elemental composition.

All SEM measurements conducted in this thesis utilize a FESEM Gemini NVision 40 instrument from Carl Zeiss, operated with the SmartSEM software. The instrument is housed at the Walter-Schottky-Institut/ZNN of TU Munich. For measurement parameters, the electron beam energy is 5 keV with a work distance of 4.5 mm. All obtained SEM images are analyzed with the ImageJ software.

3.1.2 Grazing incidence small-angle X-ray scattering

GISAXS stands as a powerful and specialized X-ray scattering method, allowing for the exploration of plasmonic nanostructures across a wide range of length scales, spanning from nanometers to micrometers. In the present thesis, GISAXS serves as a potent and adaptable instrument for investigating the surface, sub-surface, and interface structures within hybrid plasmonic architectures. The GISAXS measurements conducted in this study are executed at the MiNaXS beamline P03, situated at the PETRA III storage ring of DESY (Hamburg, Germany).

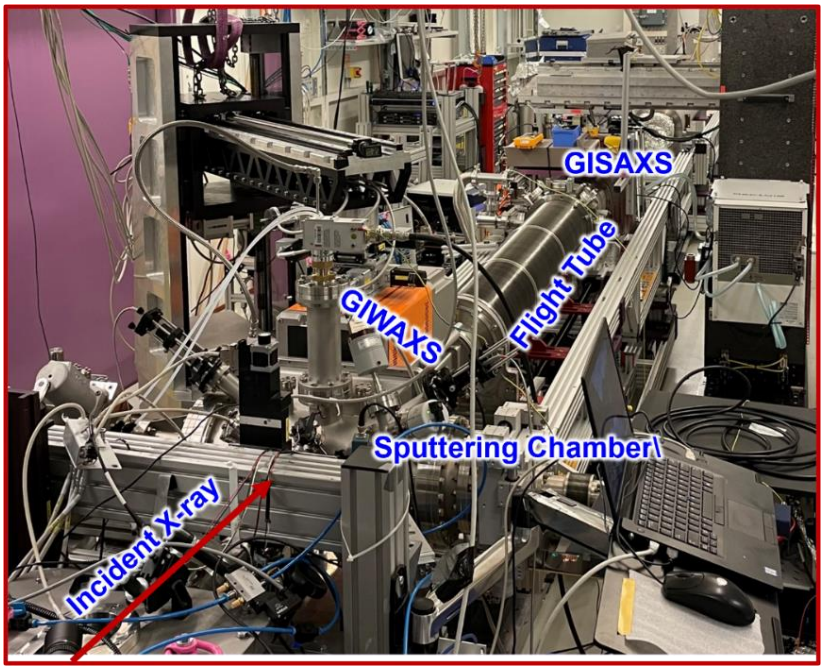

Figure 3.2. *Photograph of the mobile HiPIMS chamber integrated in the in situ GIS/WAXS setup at the P03/MiNaXS beamline of the PETRA III storage ring at DESY, Hamburg.*

In the context of the *in situ* GISAXS measurement outlined in Chapter 6, the incident X-ray photon energy is set at 11.72 keV, corresponding to a wavelength of 1.05 Å. The incident angle (α_i) is configured to 0.4°, while the sample-to-detector distance (SDD) is 3230 mm. The 2D GISAXS data are captured utilizing a Pilatus 1M detector (Dectris Ltd., Switzerland), with each pixel measuring 172 × 172 μm^2 and a time resolution of 20 Hz. To mitigate the risk of X-ray-induced damage to the sample, a beam-damage check is conducted. Additionally, the sample is periodically repositioned during the *in situ* GISAXS measurement to prevent prolonged exposure and minimize any adverse effects. Figure 3.2 shows the setup for integrating Ag sputter deposition with *in situ* GISAXS, as elaborated in Chapter 6, conducted at the P03/MiNaXS beamline of the PETRA III storage ring at DESY.

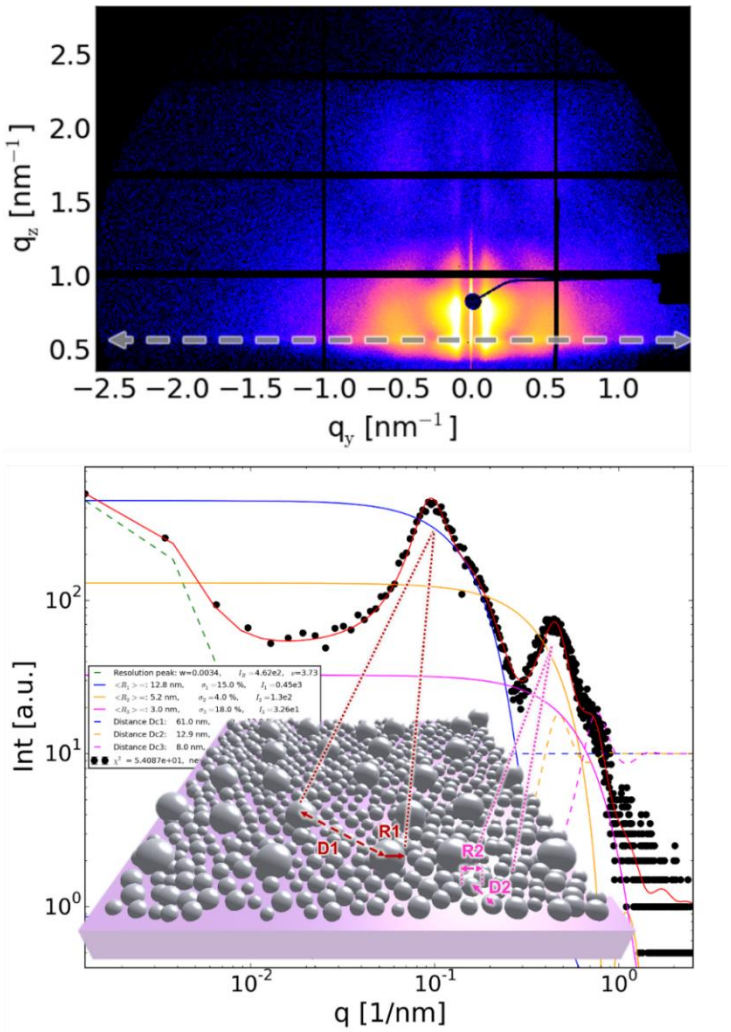

Figure 3.3. *Example of the applied GISAXS modeling of a horizontal line cut of the 2D GISAXS data. Reproduced with permission from [23]. Copyright 2024 American Chemical Society.*

For quantitative analysis of GISAXS data, horizontal line cuts are conducted at the material-specific Yoneda peak region, leveraging the DPDAK software. These line cuts contain valuable information regarding the lateral structure of the examined film. To extract characteristic length scales of the structure, these cuts are modeled using the DWBA, incorporating the EIA, the LMA, and a 1D paracrystalline lattice.

Within this analytical framework, the scattering objects are assumed to possess spherical shapes with Gaussian size distributions, which are termed form factors. The distances between neighboring objects centers, known as the structure factors, are also considered. Figure 3.3 depicts an illustrative example of a horizontal line cut extracted from 2D GISAXS data of Au/Ag nanostructures, accompanied by the applied modeling. Through this model, both the radius and the corresponding center-to-center distance can be derived. This analysis will be particularly beneficial for the investigation of formation of Au/Ag binary nanostructures, and will be further elaborated upon in Chapter 6.

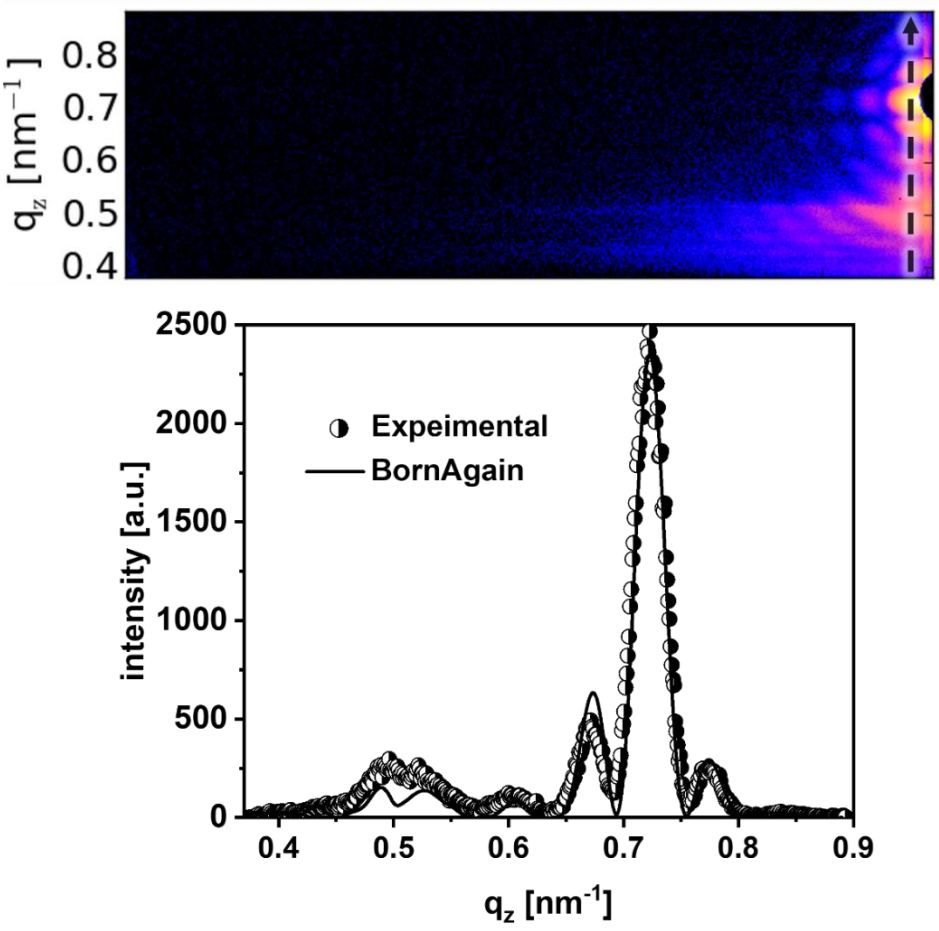

Figure 3.4. *Example of the applied off-center vertical line cut of the 2D GISAXS data. Reproduced with permission from [28]. Copyright 2023 American Chemical Society.*

Vertical line cuts, including off-centered cuts, provide insights into the film characteristics perpendicular to the substrate. As depicted in Figure 3.4, off-center line cuts of Au nanoarray offer an opportunity to analyze how the vertically organization of the NPs and their influence in the hybrid Au/PbS system. This aspect will be further explored in Chapter 7.

3.1.3 Grazing incidence wide-angle X-ray scattering

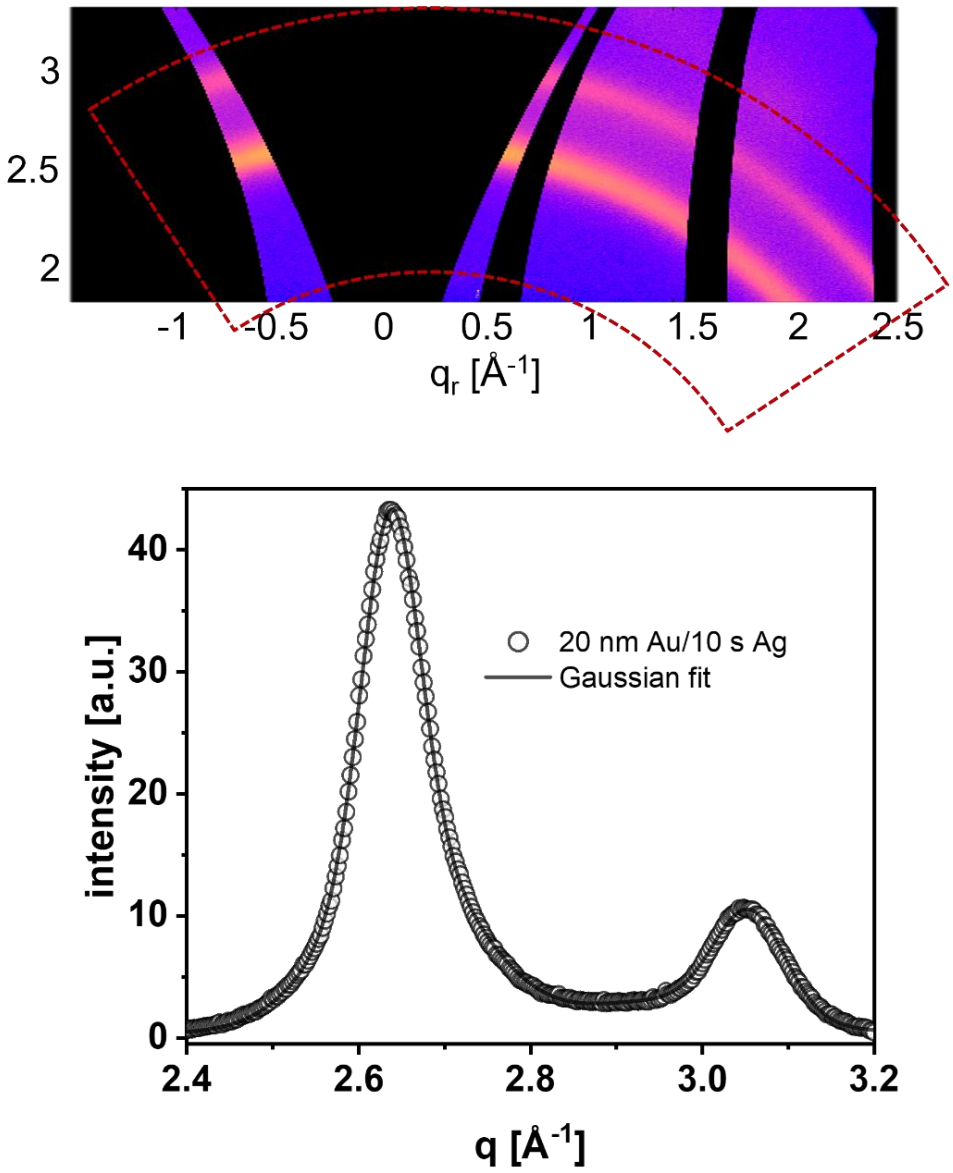

Figure 3.5. *Example of cake cut on 2D GIWAXS data and corresponding azimuthal integration. Reproduced with permission from [23]. Copyright 2024 American Chemical Society.*

GIWAXS emerges as a potent technique for probing the crystalline structure of thin films, allowing extraction of key properties such as lattice constants, crystal sizes, and orientations. In this study, *in situ* GIWAXS measurements are conducted at the P03/MiNaXS beamline of the PETRA III storage ring at DESY. Notably, due to differences in SDD between GIWAXS and GISAXS setups, simultaneous *in situ* GIWAXS and GISAXS measurements can be carried out during the sputter deposition of Ag on Au nanoarrays, as depicted in Figure 3.2. Consequently, the photon energy of the X-ray beam and the incident angle (α_i) remain consistent with those of the *in situ* GISAXS measurements, as they are conducted concurrently. The SDD of *in situ* GIWAXS measurements are set at 193.5 mm, and the corresponding 2D data is captured using a Lambda 9M detector (X-Spectrum GmbH, Germany) with a pixel size of 55 × 55 μm^2 and a time resolution of 2 Hz.

For quantitative analysis of GIWAXS data, a cake sector integral is used, as is shown in Figure 3.5. The reflecting line data is then subjected to fits with Gaussian functions. The lattice constant and crystallite size are determined by analyzing the peak center and FWHM obtained from the Gaussian function. The analysis of Au/Ag nanostructures GIWAXS patterns, offer an opportunity to analyze evolution of the binary structure during sputter deposition. This aspect will be further explored in Chapter 6.

3.2 Spectroscopic characterizations

3.2.1 UV/Vis spectroscopy

Ultraviolet-visible (UV/Vis) spectroscopy quantifies the absorption or transmission of discrete wavelengths spanning from ultraviolet to the visible region, comparing them to a reference or blank sample. The simplified configuration and operational principles of a typical double-beam UV/Vis spectrophotometer are depicted in Figure 3.6. Light is emitted by either a deuterium lamp or a tungsten halogen lamp, corresponding to the ultraviolet or visible region, respectively. Notably, the lamp can be switched during measurement to accommodate different spectral ranges.

The emitted light undergoes monochromatizating via a monochromator, comprising slits and prisms, to produce a monochromatic beam of the desired wavelength. This beam then splits into two equal parts using a beam splitter. One beam interacts with the sample being analyzed, while the other interacts with a sample reference. The intensities of both beams after interaction are captured by a detector and further analyzed by a computer.

In a UV/Vis absorption spectroscopy experiment, photons of varying wavelengths λ

are directed onto the sample, and the transmitted light is measured. According to the Lambert-Beer law, absorbance $A(\lambda)$ and transmittance $T(\lambda)$ are determined based on the relationship between the intensity of incident light and that of transmitted light through the sample. Mathematically, this relationship is expressed as:

$$A(\lambda) = log_{10}\ \frac{I_0(\lambda)}{I(\lambda)} = -log_{10}\ T(\lambda) \tag{3.1}$$

where the intensity of the incident light is $I_0(\lambda)$ and the intensity of the transmitted light is $I(\lambda)$.

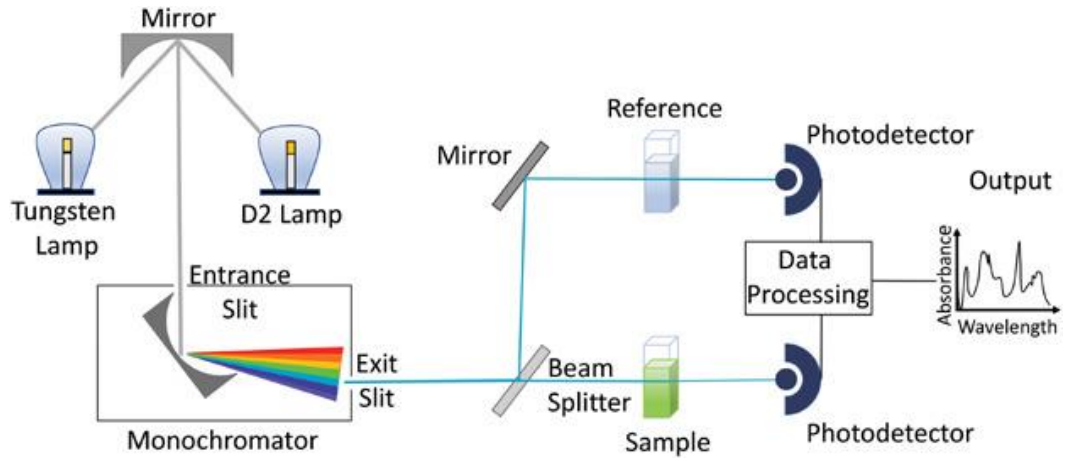

Figure 3.6. *Illustration of a typical UV/Vis spectrophotometer simplified configuration and working principle. A lamp generates light and is then monochromatized by a monochromator. Then the monochromatic beam is split into two beams by a beam splitter. One beam passes through the sample, while the other one penetrates the sample reference. The intensities of beams transmitted through sample and reference are collected by a photodetector and further analyzed [72]. Copyright 2014 John Wiley & Sons.*

Because of absorption phenomena, light intensity undergoes an exponential decrease as it traverses through the medium. This decay is mathematically expressed as:

$$I(\lambda) = I_0(\lambda) exp\ (-\mu(\lambda) d) \tag{3.2}$$

here, $\mu(\lambda)$ represents the material-specific linear absorption coefficient, and d denotes the path length of light through the medium, such as the thickness of a thin film or the cuvette.

Hence, the absorbance can be represented as:

$$A(\lambda) = log_{10}\frac{I_0(\lambda)}{I(\lambda)} = \frac{1}{ln(10)}\mu(\lambda)d \tag{3.3}$$

Consequently, the material-specific absorption coefficient can be determined using the formula:

$$\mu(\lambda) = \frac{A(\lambda)}{dln\,(10)} \tag{3.4}$$

In the case of reflective samples, like thin films, the absorption of light is influenced by substantial intensity losses resulting from total or partial reflection at interfaces with differing refractive indices. Thus, it becomes imperative to account for reflection processes. The absorbance $A(\lambda)$ in such scenarios is expressed as:

$$A(\lambda) = -log_{10}\,\frac{T(\lambda)}{I(\lambda) - R(\lambda)} \tag{3.5}$$

here, $R(\lambda)$ signifies the intensity of reflected light. This equation considers the relative decrease in transmitted light $T(\lambda)$ due to both absorption and reflection, thus providing a comprehensive assessment of absorbance for reflective samples.

For the UV/Vis spectroscopy experiments detailed in Chapter 5, the absorbance of partially transparent samples deposited on glass substrates is recorded using a Lambda 35 spectrophotometer from PerkinElmer, USA. The wavelength range is configured from 400 nm to 800 nm, with a scanning speed set to 240 nm/min and a step size of 1 nm.

In Chapter 7, UV/Vis spectroscopy measurements focus on the reflectance of non-transparent samples deposited on Si substrates. These measurements are conducted using a Lambda 950s spectrophotometer, also from PerkinElmer, USA, equipped with an integrating sphere. The wavelength range is adjusted from 350 nm to 1200 nm, with a scanning speed set to 240 nm/min and a step size of 1 nm.

3.2.2 Dynamic light scattering

In light scattering experiments, a sample is illuminated with monochromatic coherent light, and the intensity of scattered light is analyzed concerning scattering angle and/or time. The standard experimental configuration is depicted in Figure 3.7. In dynamic light scattering, variations in the intensity of scattered light over time are scrutinized, offering insights into particle diffusion. A laser emitting light with a wavelength λ is directed onto the sample, typically a solution contained within a quartz cuvette, where it undergoes scattering. The intensity of scattered light $I(t, \theta)$ is

then monitored as a function of time t and scattering angle θ using a photodetector.

To analyze particle diffusion, the normalized intensity autocorrelation function $g_2(\tau, \theta)$ is computed using a correlator:

$$g_2(\tau, \theta) = \frac{\langle I(t, \theta) I(t + \tau, \theta) \rangle}{\langle I(t, \theta) \rangle_t^2} \tag{3.6}$$

This function correlates the intensity at time t with the intensity after a delay time τ, averaging over all times. At small values of τ, when particles haven't diffused significantly, the intensities remain strongly correlated. As τ increases, the intensities become increasingly uncorrelated. Thus, the decay of $g_2(\tau, \theta)$ carries information about particle diffusion.

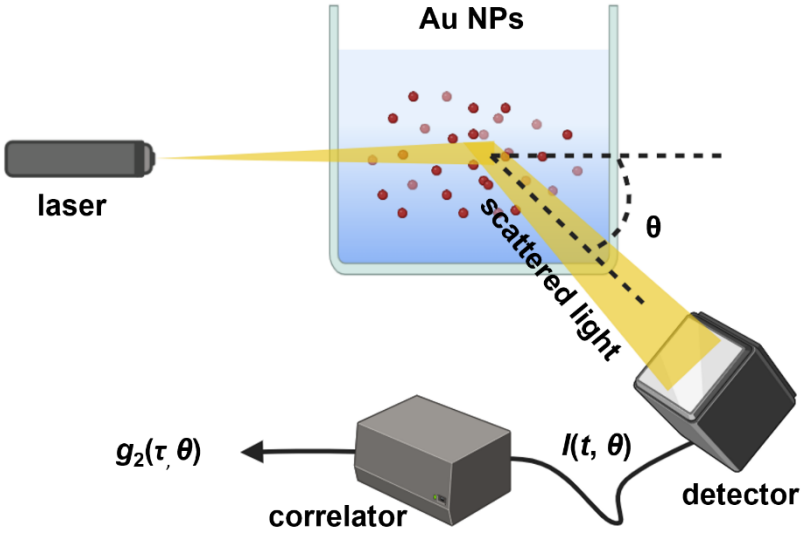

Figure 3.7. *Schematic illustration of a light scattering setup. Laser light with wavelength λ scatters from the sample. At a scattering angle θ, the scattered light intensity I (t, θ) is recorded as a function of time by a photodetector. A correlator transforms the signal into the normalized autocorrelation function* $g_2(\tau, \theta)$ *. Illustration created with BioRender.com.*

The normalized field autocorrelation function $g_1(\tau, \theta)$ is related to $g_2(\tau, \theta)$ by the Siegert relation:

$$g_2(\tau, \theta) - 1 = \beta |g_1(\tau, \theta)|^2 \tag{3.7}$$

here, β is a coherence factor dependent on the setup, typically ≤ 1. The Siegert relation holds for ergodic systems with non-interacting particles at sufficiently high number density, a condition often met in dilute polymer solutions.

In the case of monodisperse particles, the decay of the intensity autocorrelation function $g_1(\tau, \theta)$ follows a single exponential function:

$$g_1(\tau, \theta) = e^{-\Gamma\tau} = e^{-\frac{\tau}{\tau_0}} \tag{3.8}$$

where Γ represents the decay rate or the reciprocal of the decay time τ_0.

The translational diffusion coefficient (D_t) of the particles can be expressed as:

$$D_t = \frac{\Gamma}{q^2} = \frac{1}{\tau_0 q^2} \tag{3.9}$$

here, q denotes the magnitude of the scattering vector, defined by:

$$q = \frac{4\pi n}{\lambda} \sin\left(\frac{\theta}{2}\right) \tag{3.10}$$

where n represents the refractive index of the sample solvent, λ is the wavelength of the incident light, and θ is the scattering angle. For translational diffusion, D_t remains independent of the scattering angle. To verify this, DLS measurements are frequently conducted at various scattering angles. A linear relationship between Γ and q^2 suggests purely translational diffusion.

The hydrodynamic radius (R_h) of the particles is related to D_t by the Stokes-Einstein equation:

$$R_h = \frac{k_B T}{4\pi\eta D_t} \tag{3.11}$$

where k_B represents Boltzmann's constant, T denotes the solution temperature, and η stands for the solvent viscosity. R_h signifies the radius of an equivalent sphere having the same diffusion coefficient as the particles.

In Chapter 5, the DLS experiments are conducted to measure the various sizes of synthesized Au NPs. These measurements are essential to ensure that the NPs used in subsequent experiments are of the desired sizes and in optimal condition for further investigations.

3.2.3 Photoluminescence spectroscopy

Photoluminescence (PL) spectroscopy serves for analyzing the light emission from a sample post-photon absorption. This technique offers crucial insights into radiative

relaxation processes, particularly exciton recombination, which play a significant role in the operation of optoelectronic devices. During PL analysis, a specific excitation wavelength is meticulously selected, typically one that is efficiently absorbed by the material under investigation, often at its absorbance maxima. Subsequently, the emitted light is detected.

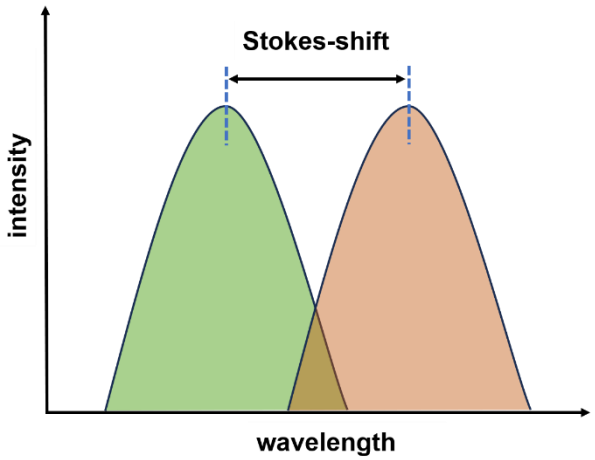

Figure 3.8. *Illustration of typical absorbance and PL spectra. Due to relaxation processes, the emission spectrum is red-shifted relative to the absorbance spectrum (Stokes-shift).*

In addition to providing insights into exciton recombination, PL spectroscopy can also reveal important information about the electronic structure, bandgap, and defect states within the material. By examining the spectral characteristics of the emitted light, it can gain valuable knowledge about the material photophysical properties. The emitted photons arise from various vibrational levels of the electronically excited state, transitioning to different vibrational levels of the ground state. As depicted in Figure 3.8, this phenomenon leads to the observation of a broad emission spectrum, often fits well with a Gaussian function.

Time-resolved photoluminescence (TRPL) analysis serves as an invaluable technique for study the intricacies of charge carrier dynamics within functional stacking layers, such as those observed in optoelectronic devices. Time-correlated single photon counting (TCSPC) is a widely adopted method for conducting TRPL measurements. The fundamental operational principle of TCSPC is vividly illustrated in Figure 3.9. Here, the sample undergoes illumination by a laser pulse, resulting in the generation of a characteristic waveform. The time interval between the excitation of the sample by the laser pulse and the subsequent detection of the emitted photon at the detector is meticulously measured and plotted along the x-axis. The corresponding number of photons detected for each time delay is represented along the y-axis. In scenarios

where the number of detected photons per excitation pulse is notably less than 1, mirrors the decay curve. Typically, multi-exponential decay functions are used to fit the decay curve, enabling the extraction of decay times τ.

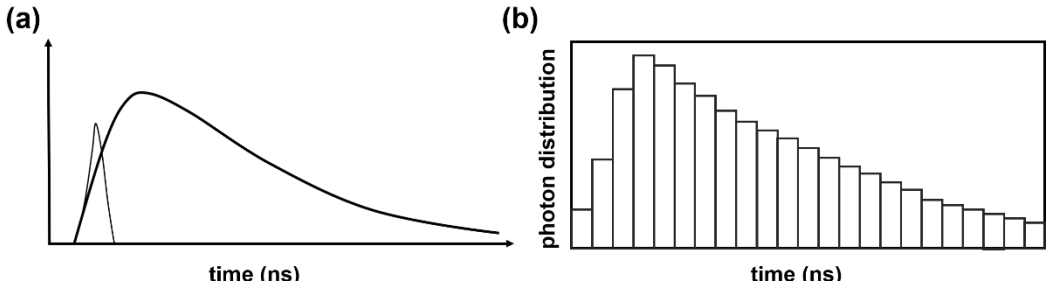

Figure 3.9. *Schematic illustration of working principle of TCSPC (a) A measured waveform, (b) a histogram of the number of photons detected at different time scale.*

The amplitude-weighted average lifetime (τ_{v1}) is calculated using the equation:

$$\tau_{v1} = \sum_i \alpha_i \tau_i \tag{3.12}$$

Intensity-weighted average lifetime (τ_{v2}) is calculated using the equation:

$$\tau_{v2} = \frac{\sum_i \alpha_i \tau_i^2}{\sum_i \alpha_i \tau_i} \tag{3.13}$$

here, τ_i represents the decay lifetime for different components, and α_i denotes the amplitude fraction of each lifetime component.

In Chapter 7, a Picoquant Fluotime 300 spectrofluorometer is utilized to perform both PL and TRPL measurements, using an excitation wavelength of 370 nm. These measurements played a crucial role in examining how the presence of Au NPs impacted the charge carrier mobility within the hybrid PbS film.

3.2.4 Raman spectroscopy

Surface-enhanced Raman spectroscopy (SERS) is an advanced variant of Raman spectroscopy that leverages nanostructured metal surfaces to significantly enhance Raman signals. This enhancement arises from the excitation of localized surface plasmons, leading to a substantial increase in signal intensity. Raman spectroscopy is an invaluable analytical tool, utilize light scattering to elucidates diverse properties of

a substance, ranging from its chemical composition, phase, and crystallinity to molecular interactions. It serves as a non-invasive and non-destructive method, offering intricate insights into molecular structures, even within intricate matrices like tissues.

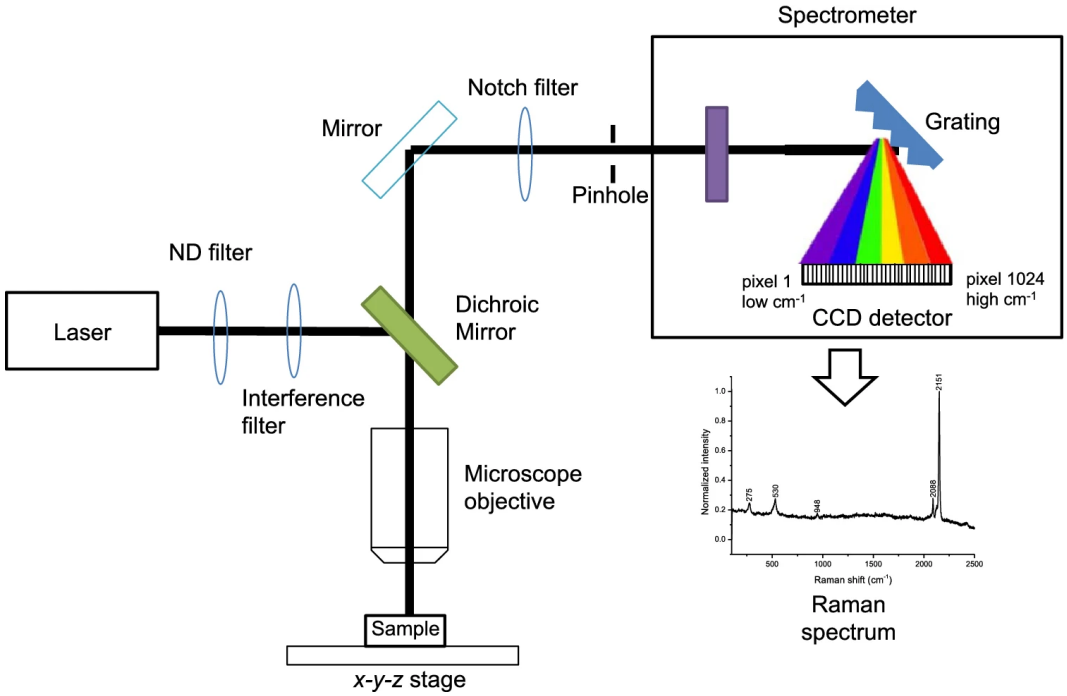

Figure 3.10. *Illustration of simplified light-path configuration and working principle of a typical Raman spectrometer. Laser, generated by a laser generator, passes through a series of optical components and microscopy and focuses on the sample surface. The scattered beam leaves the sample reversely and then passes through a filter, a slit, and a diffraction grating. Finally, the intensity of photons at each wavelength is recorded by a CCD camera. Green arrows show the path of the laser from the laser generator to the sample surface, while red arrows represent the path of the scattered beam from the sample surface to the CCD camera [73]. Copyright 2021 Springer.*

A standard Raman spectrometer, depicted in Figure 3.10, encompasses several integral components and adheres to a specific operational framework. Initially, a laser source emits a beam of light, subsequently expanded by a beam expander. This expanded beam traverses through a sequence of optical components before reaching a microscopy setup, where it converges onto the sample surface. Following interaction with the sample, the scattered signal retraces its trajectory, undergoing filtration to eliminate unwanted light elements, including Rayleigh scattering and out-of-focus rays. A strategically positioned diffraction grating along the light path disperses the scattered light based on its wavelength, facilitating the capture of photon intensity

across the spectrum by a charge-coupled device (CCD) detector.

In Chapter 6, Raman spectra are obtained using an alpha300R Confocal Raman Microscope (WITec GmbH, Germany), with a 633 nm laser and a TruePower module 50× objective (Zeiss LD Epiplan NEOFLUAR 50 × 0.55; Carl Zeiss AG, Germany). The spectrometer is located at Nano-Institute Munich (Ludwig-Maximilians-Universität München, Munich, Germany), which equipped with a 600 lines/mm grating and a Newton 970 EMCCD camera from Andor Technology Ltd., Belfast, UK. For SERS measurements, a rhodamine 6G aqueous solution (10^{-4} M, 10 μL) is deposited onto the sample surface. SERS spectra are acquired with an acquisition time of 2 s, 30 accumulations, and a laser power of 0.5 mW.

3.3 Photodetector characterization

Lateral photodetectors, also known as photoconductors, are primarily evaluated using a probe station (SOFN 7-SCF06A/B) system located at Department of Electrical & Electronic Engineering, Southern University of Science and Technology (SUSTech, Shenzhen, China). For optoelectrical measurements, the fabricated photodetector device is placed on the probe station. Electrical signals are applied and measured on the photodetector using a Keithley 4200 Source Meter, which offers a broad range of bias voltages from 0 to 200 V and can measure extremely small current signals. In combination with a light source (Zolix, TLS2-T250-DZL) and a monochromator, this setup characterizes the IV relationship and responsivity of the photodetectors. Responsivity, a measure of the device ability to convert light into an electrical current, is calculated by:

$$R = \frac{I_{light} - I_{dark}}{P_{input}} \tag{3.14}$$

where I_{light} represents the current under illumination, I_{dark} represents the current in darkness, and P_{input} is the input light power density.

Additionally, an oscilloscope and a light chopper are used to measure the on/off response of the photodetector. To calculate detectivity, another critical performance metric, noise analysis is performed using lock-in amplifiers (SR 570 and SR 830). Detectivity (D^*) is calculated using the following equation:

$$D^* = \frac{\sqrt{A}}{NEP} = R\sqrt{\frac{A\Delta f}{\bar{I}_n}} \tag{3.14}$$

this calculation is based on the noise equivalent power (NEP) and the mean noise current (I_n). Here, A is the active area (1 cm^2), R is the responsivity, and Δf is the electrical bandwidth (1 Hz).

A detailed performance analysis of the relevant photodetector devices are provided in Chapter 7.

3.4 2D GISAXS data simulation

As elaborated in this thesis GISAXS is used to characterized hybrid plasmonic nanostructures. The grazing-incidence configuration is used to analysis the dimensions and shape of nanostructures, both horizontally and vertically, in relation to the film surface. The substantial interaction between the X-ray beam and the sample in GISAXS results in a high scattering intensity, which is crucial for an extensive examination of the film area. The utilization of synchrotron radiation in GISAXS allows for real-time measurements. GISAXS simulations are at the forefront of this field, expanding the range of systems that can be modeled and accurately incorporating all elements influencing the scattering pattern within the DWBA framework. These simulations focus on creating 2D GISAXS patterns for specific film configurations, which are then aligned with experimental data for comparison and adjustment.

Despite the depth of analysis that simulations offer, there are several challenges that hinder the broader application of GISAXS. It is crucial to find an effective method for simulating 2D GISAXS patterns, especially for plasmonic nanostructures. In this thesis, the software BornAgain (version 1.17.0) is used to simulate the 2D GISAXS patterns of Au NSs [74]. This software is recognized for its ability to simulate nanoarrays with the flexibility to position particles, even those with complex shapes. BornAgain, developed by the Scientific Computing Group at MLZ, Garching, evolves from IsGisaxs, which was once the standard tool for GISAXS simulations. BornAgain not only inherits the capabilities of IsGisaxs but also improves upon them with a more user-friendly interface and additional functionalities. A significant enhancement in BornAgain is its ability to simulate samples containing multiple layers, a feature not present in IsGisaxs.

Table 3.1. Instrumental parameters of GISAXS data simulation.

α_i (°)	λ (Å)	SDD (mm)	P (µm)
0.32	0.965	3554	55

The fundamental parameters for the instrumentation are selected to match the experimental conditions. These parameters include the incident angle α_i , the wavelength of the X-ray beam λ, the sample to detector distance SDD, the size of the detector pixels P, and the position of the direct beam σ are list in Table 3.1.

In the simulations, the Au NSs are represented with spherical particles. The formulas for the full sphere form factor F, volume V, and horizontal cross-sectional area A are given below, with (R)indicating the sphere radius:

$$F = \frac{4\pi}{q^3} exp(iq_z R)\,[sin(qR) - qRcos(qR)] \tag{3.16}$$

$$V = \frac{4\pi}{3} R^3 \tag{3.17}$$

$$A = \pi R^2 \tag{3.18}$$

These spheres are organized into a hexagonal pattern, showing a degree of regularity. This arrangement is determined by the interference function of the particles, indicative of a paracrystalline structure.

$$S(\vec{q}) = Re\left(\frac{1 + P_1(\vec{q})}{1 - P_1(\vec{q})}\right) Re\left(\frac{1 + P_2(\vec{q})}{1 - P_2(\vec{q})}\right) \tag{3.19}$$

Here, $P_1(\vec{q})$ and $P_2(\vec{q})$ refer to two different patterns of particle arrangement. Each follows a Fourier-transformed Cauchy distribution, but they are oriented in varying lattice directions.

Table 3.2. SLD parameters of the used materials for 2D GISAXS simulation.

Materials	SLD_r (Å^{-2}, 10^{-4})	SLD_i (Å^{-2}, 10^{-6})
Au	1.1922	14.9134
Si	19.9001	0.1836

The simulation also considered the SLD of the used materials, including the real SLD and imaginary SLD, as listed in Table 3.2. Figure 3.11 shows an example of a 2D

GISAXS data simulation of a self-assembled 20 nm Au nanoarray. The layout of the simulation, as shown in Figure 3.11a, used a multilayer structure. This included a silicon substrate layer and an air layer with a monolayer of the modeled Au NSs, shaped as spheres and incorporating 2D paracrystal interface functions. The model and the GISAXS simulation results are shown in Figures 3.11b and c. In this specific simulation, the size of Au NPs is 20.4 nm with an interparticle distance of 71 nm.

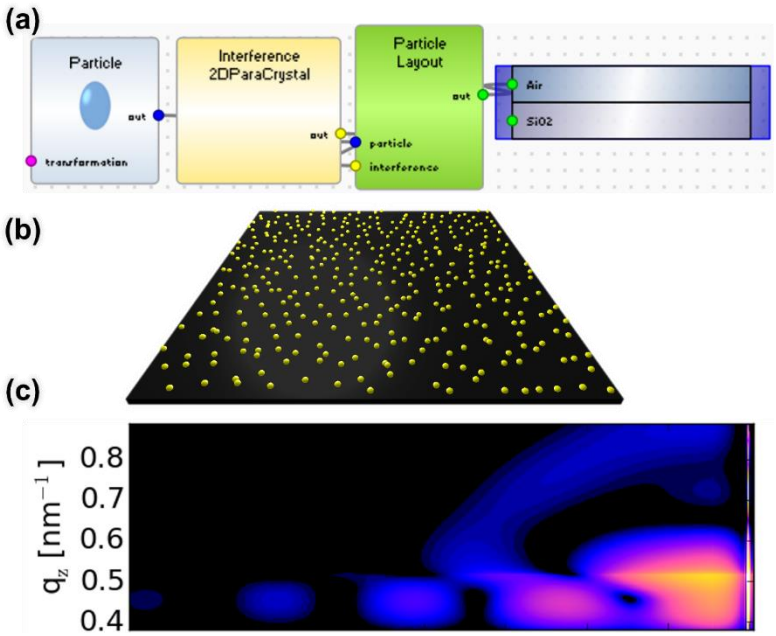

Figure 3.11. *(a) Interface of BornAgain simulation. (b) Visualization of 20 nm Au NSs modeling set up and (c) simulation results. These pictures are all exports from BornAgain software. Reproduced with permission from [28]. Copyright 2023 American Chemical Society.*

4 Sample preparation

This chapter introduces the sample preparation conducted before all experiments described in this thesis. Accordingly, Section 4.1 lists the materials used in this study. Section 4.2 outlines the preparation of Au nanoarray, including synthesis of Au NPs, self-assembly of Au nanoarray in both electronic adsorption and water/hexane interface transfer methods. An explanation of inter-digital electrode is presented in Section 4.3. The preparation of PbS quantum dots film is given in Section 4.4 containing both synthesis and spin-coating of PbS quantum dots. Finally, the preparation of Au/Ag nanostructure by sputter deposition is depicted in Section 4.5.

4.1 Materials

Chloroauric acid

Chloroauric acid ($HAuCl_4$, 99.9 %) was obtained from Sigma-Aldrich (Germany) and used as the precursor solution for the synthesis of Au NPs. Initially, the $HAuCl_4$ was dissolved in deionized water and subsequently diluted to a concentration of 0.3 M in a volumetric flask and stored in a 4 °C refrigerator for further use.

Sodium borohydride

Sodium borohydride ($NaBH_4$, 99 %) was obtained from Sigma-Aldrich (Germany)and used as a reducing agent in the synthesis of Au nanoseeds, which are utilized for the subsequent growth of larger Au NPs, as will be explained later.

L-ascorbic acid (AA)

L-ascorbic acid (AA, 99 %), procured from Sigma-Aldrich (Germany), functioned as the reducing agent in the synthesis of large-sized Au NPs, with further details to be discussed subsequently.

Cetyltrimethylammonium bromide (CTAB)

Cetyltrimethylammonium bromide (CTAB, 99 %), sourced from Sigma-Aldrich

(Germany), was used as a surfactant to stabilize both Au nanoseeds and the synthesized Au NPs.

Cetyltrimethylammonium chloride (CTAC)

Cetyltrimethylammonium chloride (CTAC, 98 %) was procured from Sigma-Aldrich (Germany) and utilized as a surfactant for stabilization purposes during the synthesis of large-sized Au NPs.

3-Aminopropyltriethoxysilane

3-Aminopropyltriethoxysilane (APTES, 98 %), acquired from Sigma-Aldrich, was dissolved in deionized water and then diluted to a concentration of 0.1 M. It was utilized for the surface modification of substrates to introduce amino groups, facilitating self-assembly.

Succinic anhydride

Succinic anhydride (99 %), sourced from Sigma-Aldrich (Germany), was used for the surface modification of substrates.

Lead(III) oxide

Lead(III) oxide (PbO_2, 99.99 %), sourced from Sigma-Aldrich (Germany), was used as the precursor to supply Pb in the fabrication of PbS QDs.

Oleic acid

Oleic acid (OA, 98.5 %) acquired from Sigma-Aldrich (Germany) was utilized as both a solvent and a surface-coating ligand for PbS-OA QDs.

1-octadecene

Octadecene (ODE, 90 %) purchased from Sigma-Aldrich (Germany) was used as a solvent and stabilizer in the preparation of PbS QDs.

Bis(trimethylsilyl)sulfide

Bis(trimethylsilyl)sulfide [$(TMS)_2S$] was obtained from Sigma-Aldrich (Germany) and used as a precursor to provide sulfur for the synthesis of PbS QDs.

Tetra-n-butylammonium iodide

Tetra-n-butylammonium iodide (TBAI, 10 mg mL^{-1} in methanol), procured from Sigma-Aldrich (Germany), served as surface-coating ligand for PbS-TBAI QDs

Octane

Octane (99 %) procured from Sigma-Aldrich (Germany) was used as a solvent for both the synthesis and dissolution of PbS-OA QDs

Methanol

Methanol (MeOH, 99.8 %) acquired from Sigma-Aldrich (Germany) was utilized as the solvent for preparing the TBAI solution.

Deionized Water

For all substrate cleaning procedures necessitating purified water, deionized water generated by a PURELAB CHORUS 1 (VEOLIA) was used.

Ethanol

Ethanol (99.8 %), obtained from Sigma-Aldrich (Germany), was utilized in the formulation of the ZnO precursor solution.

Acetone

Acetone (99.8 %), sourced from Carl Roth (Germany), was used in the ultrasonic cleansing of both Si and glass substrates.

Hydrogen Peroxide

Hydrogen peroxide (H_2O_2, 30 %), procured from Carl Roth (Germany), was utilized as an oxidizing agent for the acid cleaning of both Si and glass substrates.

Sulfuric Acid

Sulfuric acid (H_2SO_4, 96 %), obtained from Carl Roth (Germany), was used for the acid cleaning of both Si and glass substrates.

Rhodamine 6G (R6G)

Rhodamine 6G (R6G, 99 %), acquired from Sigma-Aldrich (Germany), as the detection molecule in SERS measurements and was diluted to a concentration of 10^{-4}.

Glass Substrates

Microscopic slides (7.5 cm × 7.5 cm) were obtained from Carl Roth (Germany) and the slides were segmented into pieces of 2.5 cm × 2.5 cm for underwent acid cleaning before being utilized as substrates for self-assembly of Au NPs.

Silicon wafers

Silicon wafers (Si 100, p-type) were acquired from Silchem Handels GmbH (Freiberg, Germany). These wafers were cut into segments measuring 2 cm x 2 cm and subjected to acid cleaning prior to their use as substrates for the self-assembly of Au NPs.

Silver

Silver (99.99 %) purity, procured from Goldkontor GmbH (Hamburg, Germany), was utilized as a sputter target for the deposition of Ag on the Au template in Chapter 6.

4.2 Preparation of Au nanoarray

The synthesis and self-assembly method for the Au NPs is based on the literature [47] and fabricated in collaboration with the Institute of Functional Nano & Soft Materials (FUNSOM) at Soochow University, Suzhou, China.

4.2.1 Synthesis of Au NPs

In the presented thesis, various sizes of Au NPs are synthesized to explore their possible applications. Initially, Au NPs with diameters ranging from 3-5 nm are synthesized to serve as seeds for the subsequent production of 10 nm and 20 nm Au NPs. These, in turn, are utilized as seeds for generating larger Au NPs, with sizes varying between 30 and 100 nm. The detailed methodology for the synthesis is described as follows. A mixed solution of CTAB (0.1 M, 9.75 mL) and $HAuCl_4$ (0.01 M, 0.25 mL) is quickly combined with a freshly prepared $NaBH_4$ solution (0.01 M, 0.6 mL) in an ice bath. The mixture is stirred at 600 rpm for 2 min and then allowed to stand at room temperature for 2 h, resulting in Au nanoseeds of 3-5 nm size. These nanoseeds are then used to synthesize 10 nm and 20 nm Au NPs.

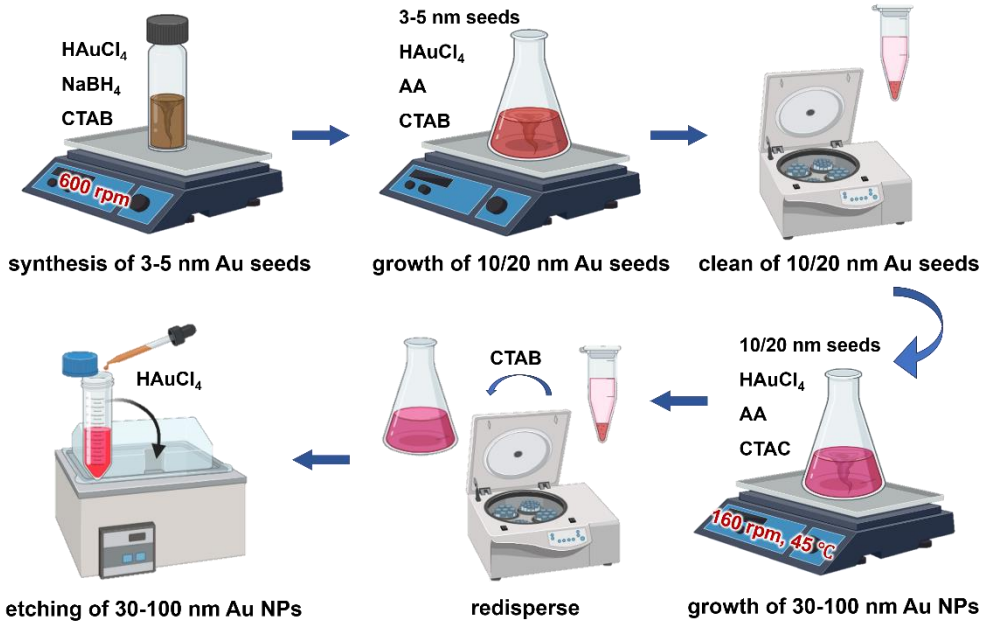

Figure 4.1. *Schematic illustration of the experimental procedure of the seed-mediated method for creating multi-sized Au NPs. Illustration created with BioRender.com.*

For 10 nm Au NPs, CTAB (0.1 M, 9.75 mL), $HAuCl_4$ (0.01 M, 4 mL), AA (0.1 M, 15

mL), and Au nanoseed solution (0.24 mL) are sequentially added to 190 mL of DI water. The reaction is stopped after 10 min, and the mixture is stirred and left to stand at room temperature overnight to yield Au NPs. Similarly, to obtain 20 nm Au NPs, CTAB (0.1 M, 19.5 mL), $HAuCl_4$ (0.01 M, 8 mL), AA (0.1 M, 30 mL), and Au nanoseed solution (0.24 mL) are sequentially added to 380 mL of deionized water. The reaction is halted after 10 min, and the mixture is stirred and left to stand at room temperature overnight.

Additionally, both 10 nm and 20 nm Au NPs can serve as seeds for the synthesis of larger Au NPs. Following an overnight rest, the solutions underwent two rounds of centrifugation to remove excess surfactant and then are redispersed in DI for subsequent procedures. Specifically, the centrifugation settings are 1000 rpm of 7 min for the 10 nm NPs, and 10000 rpm of 5 min for the 20 nm Au NPs. The schematic representation of the synthesis process can be referred to Figure 4.1.

Table 4.1. *Centrifugation speed and duration for Au NPs samples in different sizes*

Seeds (nm)	Amount (mL)	Expect Diameter (nm)	Centrifugation speed and time (rpm, min)
3-5	0.2	10	18000, 7
3-5	0.12	20	14000, 5
10	2	30	12000, 3
10	0.5	50	8000, 3
20	2	60	7000, 3
20	1.5	70	6000, 2
20	1	80	5000, 2
20	0.5	100	5000, 1

The seed growth method can fabricate Au NPs with sizes ranging from 30 to 50 nm and 50 to 100 nm, by adjusting the volume of Au nanoseeds (specifically, 10 and 20 nm Au NSs between 0.5 to 2 mL within the growth solution.

As an example, the synthesis of 50 nm Au NSs is detailed for elaborates. Initially, the 10 nm Au seeds are centrifuged, concentrated to four times their original volume, and then redispersed in water. Following this, in an aqueous CTAC solution 0.025 M, 30 mL under continuous stirring at a speed of 160 rpm, then introduced the seed solution 0.5 mL, AA 0.1 M, 0.75 mL, and $HAuCl_4$ (0.01M, 1.5 mL). This procedure is conducted in a water bath maintained at a constant temperature of 45 ℃. After 3 h, the solution is centrifuged to remove the supernatant and then redispersed in a CTAB solution (0.02 M, 30 mL). With stirring at 160 rpm and the temperature held constant at 45 ℃ in the water bath, $HAuCl_4$ (0.01 M, 0.2 mL) is added to the CTAB dispersion of the Au NPs. The solution underwent centrifugation 2 h later, and the obtained Au NPs are redispersed in water and stored in the refrigerator.

Prior to initiating the self-assembly process, the Au NPs are allowed to reach room temperature. This is followed by an additional centrifugation step to eliminate any surplus CTAB coatings on their surface. Figure 4.1 shows the schematic diagram of the synthesis process of large sizes Au NPs. And Table 4.1 centrifugation speed and duration for Au NPs samples in different sizes.

4.2.2 Preparation of substrates

All the substrates used in this thesis, including Si, glass, and IDE, underwent the same surface modification process. In this section, Si is served as an example to illustrate the method of surface modification applied to these substrates. To remove contaminants or organic residues from the surface of the Si substrate utilized in this thesis, they are subjected to cleaning via a hot acid bath before self-assembly. Consequently, a solution comprising 50 mL of deionized water, 180 mL of H_2SO_4, and 80 mL of H_2O_2 is prepared in a beaker, which is then placed in a water bath to gently heat the acidic mixture to a temperature of 80 ℃.

To prevent evaporation, the beaker containing the acid solution is covered with a watch glass. Si substrates within a sample holder, are immersed in the acid bath. Following a 15 min treatment, the substrates are extracted from the acid solution and rinsed sequentially in DI water. Each substrate is then thoroughly rinsed with deionized water and dried under a steady stream of N_2. For extended storage, all substrates are kept in a sealed sample box for future use.

In case the Si substrates that have been stored for a long period, it is necessary to re-clean the substrates. This involves securing them onto a holder and subjecting them to a cleansing process with acetone for 20 min, followed by ethanol for another 20 min, all within a water bath maintained at 30 ℃. After this cleaning procedure, the substrates are dried with N_2 gas. Subsequently, oxygen plasma cleaning is performed using a NANO PLASMA CLEANER (Diener Electronic). The substrates are placed

inside a vacuum chamber that is filled with oxygen, and plasma treatment is administered for 20 min at 0.45 mbar, 40 Hz, and 250 W. This oxygen plasma treatment not only increases the hydrophilicity of the surfaces but also improves their affinity for Au NPs solutions, which is advantageous for the self-assembly process.

4.2.3 Self-assembly of Au NPs

Electrostatic adsorption method

All synthesized Au NPs can undergo self-assembly through this method. Initially, a 6 mL solution of Au NPs is centrifuged as per the instructions in Table 4.1 to eliminate excess CTAB, and subsequently redispersed in 1 mL of DI water within a clean beaker. Following the cleaning process, a specific volume ratio of APTES to ethanol is prepared in a clean beaker, and the Si substrates are immersed in this solution for 6 h. Upon removal, the surface of the substrates is thoroughly cleansed of any residues using an ample amount of ethanol, followed by two ultrasonic washes in deionized water, and then dried with N_2. This procedure modifies the surface of the substrates with amino functional groups.

The substrates are then immersed in a 0.1 M ethanol solution of succinic anhydride to introduce carboxyl groups onto the surface. The surface-modified Si slides are then gently placed into the Au NPs solution, ensuring that the entire surface of the Si wafer is immersed in the solution. Figure 4.2 shows the schematic representation of the SAM method in which Au NPs assembled on the substrate through electrostatic adsorption method.

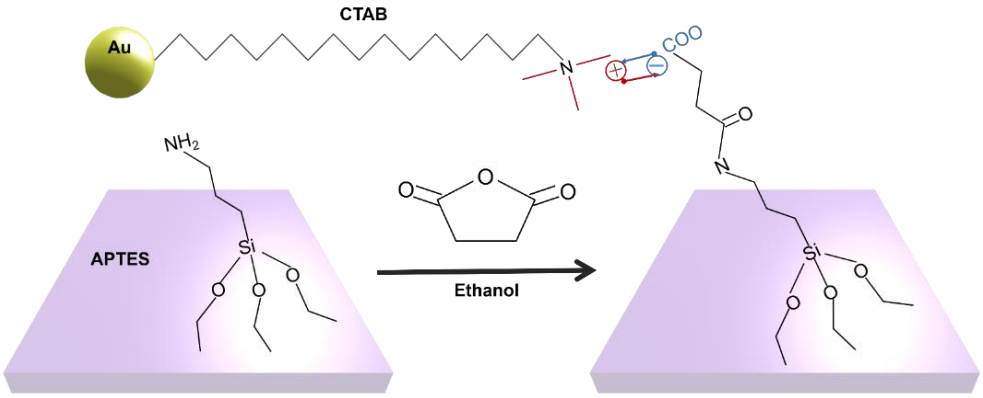

Figure 4.2. *Schematic diagram of SAM method in which Au NPs assembled on the substrate through electrostatic force.*

After allowing the setup to rest for 6 h at room temperature, the Si slides are removed and dried using a gentle stream of N_2. To thoroughly remove any chemical coatings from the Au NPs post self-assembly, the substrates are cleaned multiple times with

ethanol washing and subjected to annealing at 100 ℃ for 5 min. Then the dried Si slides are prepared for further analysis. The schematic representation of the substrates modification and self-assembly process can be referred to Figure 4.3.

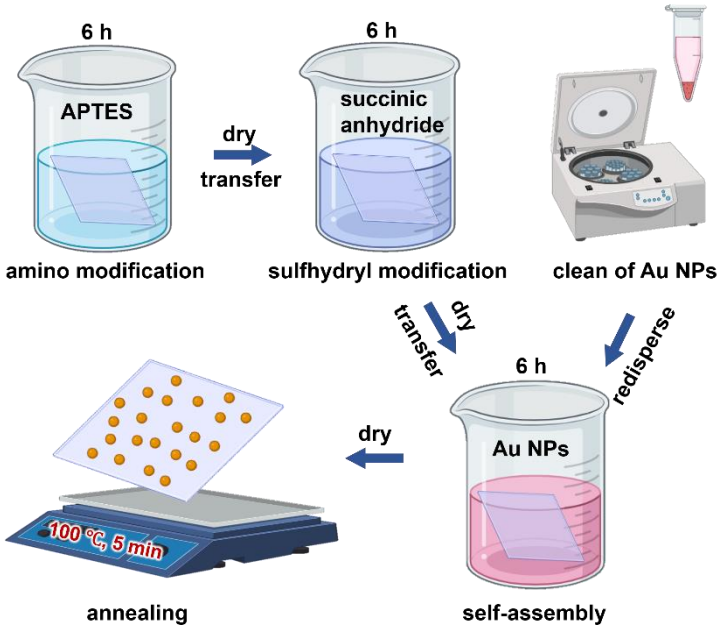

Figure 4.3. *Schematic illustration of the experimental procedure of self-assembly of AuNPs on a substrate. Illustration created with BioRender.com.*

Water/hexane phase interface transfer method

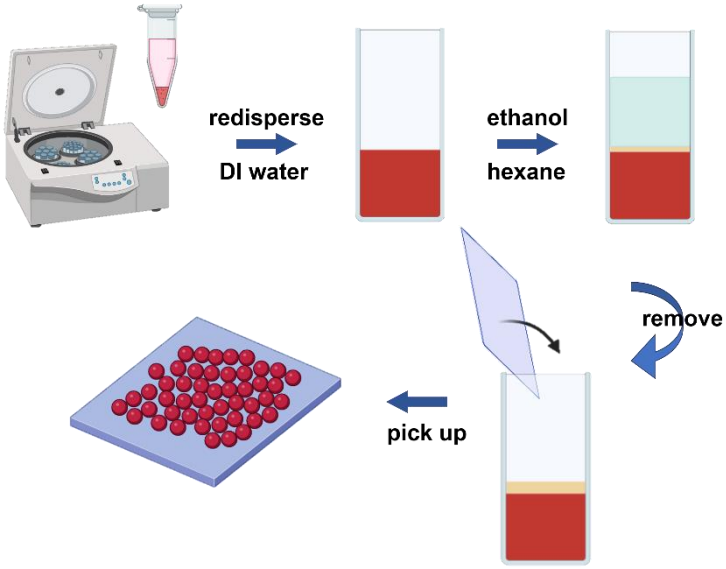

Figure 4.4. *Schematic illustration of the experimental procedure of the water/hexane interface method. Illustration created with BioRender.com.*

Similar with the electrostatic adsorption method, before assembly the Au NPs with the phase interface transfer method, each size of synthesized Au NPs is centrifuged as to remove the supernatant (CTAB). The Au NPs are then redispersed in 2 mL of DI water and transferred into a scintillation vial. Subsequently, 2 mL of hexane is added with care to form a layer above the aqueous colloid. Into the upper region of this colloid layer, 200 μL of ethanol is slowly introduced. Within minutes, a thin film displaying an Au shimmer forms at the interface between water and hexane, as visible in Figure 4.4. To facilitate the transfer of the Au NP monolayer onto a substrate, the hexane layer is carefully removed using a pipette, revealing the gold film. This film can then be collected using a precut small Si wafer. The Si wafers with the transferred gold film are left to dry for 8 h in preparation for further analysis.

4.3 Preparation of inter-digital electrode

Fabricating the inter-digital electrode substrate follows the method described in the literature [50] and is conducted in collaboration with the Department of Electrical & Electronic Engineering at Southern University of Science and Technology (SUSTech), Shenzhen, China. The fabrication process for the IDE is executed on a 4-inch silicon wafer equipped with a 300 nm thick thermal oxide layer SiO_x as the base. The photolithography sequence involved applying a dual-layer resist under specified conditions. Initially, a coating of LOR7A (MicroChem, USA) is spin-coated on the substrate at 5000 rpm for 20 s, followed by a baking period at 150 ℃ for 10 min. Subsequently, a second layer of RZJ-304 (Suzhou Ruihong, China) is applied at 4000 rpm for 20 s and baked at 100 ℃ for 2 min. The exposure phase utilized a light dose of 40 mJ/cm^2. Afterwards, the substrate is developed with RZX-3038 (Suzhou Ruihong, China) for 1 min, rinsed with deionized water, and baked at 150 ℃ for 10 min. An inductively-coupled plasma (ICP) oxygen etch treatment is executed for 30 s to serve as a descum step. Chromium is deposited at a rate of 0.5 Å/s to form a metal layer of 5 nm, followed by gold deposition at 0.5 Å/s to reach a thickness of 100 nm. The lift-off process involved soaking the substrate in a hot Dimethyl sulfoxide (DMSO) solvent at 80 ℃ for over an hour and then rinsing with DI water, culminating in the completion of IDE device.

4.4 Preparation of PbS quantum dots film

The method of preparation of PbS QDs film based on the approach described in the literature [50] is conducted in collaboration with the Department of Electrical & Electronic Engineering at Southern University of Science and Technology (SUSTech), Shenzhen, China.

4.4.1 Synthesis of PbS quantum dots

The synthesis of OA-capped PbS QDs is executed using a sophisticated hot injection method. A three-neck flask is charged with 5.4 g of PbO, 18 mL of OA, and 40 mL of ODE. This blend is progressively heated under a N_2 atmosphere to a temperature of 120 ℃, crucial for the stable formation of a lead precursor solution, indicated as $Pb(OA)_2$. The mixture is diligently kept at this temperature for 8 h to ensure the reaction reached completion.

Subsequently, a sulfur precursor is prepared by dissolving 2 mL of $(TMS)_2S$ in 20 mL of ODE. This solution is promptly injected into the $Pb(OA)_2$ solution, initiating the QD formation process. The reaction is permitted to proceed for 2 min, a specifically chosen time frame to optimize the growth of the QDs before being quenched with the introduction of 20 mL of octane. Immediate cooling in an ice bath ceased the reaction, essential for maintaining the targeted QD size and halting further growth.

The product then underwent multiple purification cycles to eliminate unreacted substances and by-products. This entailed a sequence of centrifugation operations using methanol and butanol as dispersants, efficiently isolating the QDs. Ultimately, the purified QDs are redispersed in octane to achieve a concentration of 50 mL rendering a uniform solution poised for additional characterization and utilization. The synthesis diagram of PbS QDs as illustrated in Figure 4.5.

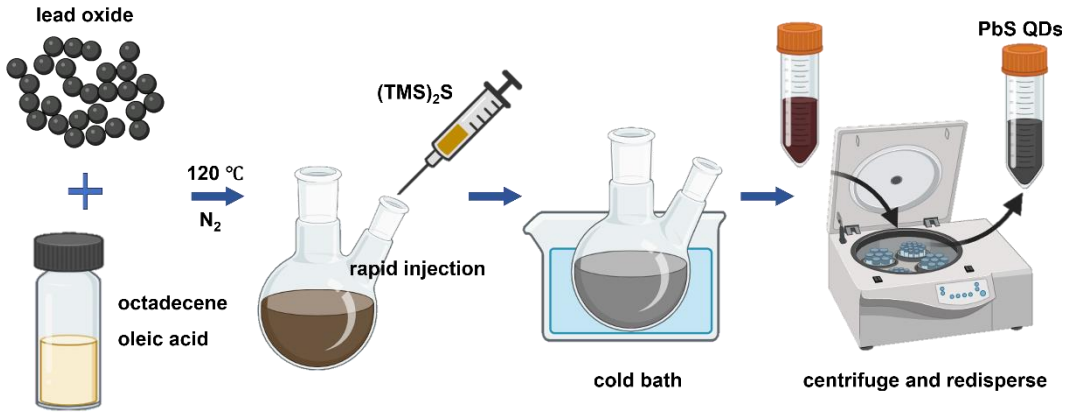

Figure 4.5. *Illustration of the process for preparing PbS QDs by hot-injection method. Illustration created with BioRender.com.*

4.4.2 Spin-coating of PbS quantum dots

The solution described above is subjected to a spin-coating procedure at 3000 rpm for 10 s, applied to both Si and IDE substrates, to the formation of OA-capped PbS films.

Furthermore, for the creation of the hybrid plasmonic film, self-assembled substrates adorned with 20 nm and 100 nm Au NPs, as previously detailed, are utilized. To synthesize the TBAI modified PbS solid, a TBAI solution (concentration: 10 mg/mL in methanol) is delicately dispensed onto the PbS-OA film and remain for 30 s. This initiated an automatic ligand exchange process, effectively replacing OA ligands with TBAI molecules on the PbS surface. To ensure the removal of any residual OA ligands, the film underwent a double rinse with pure methanol. For the fabrication of densely packed PbS-TBAI structures, the entire deposition and ligand exchange process is meticulously repeated three times. This approach ensures the formation of uniform and closely packed PbS-TBAI films, optimizing their properties for the intended applications. The spin-coating diagram of PbS QDs as illustrated in Figure 4.6.

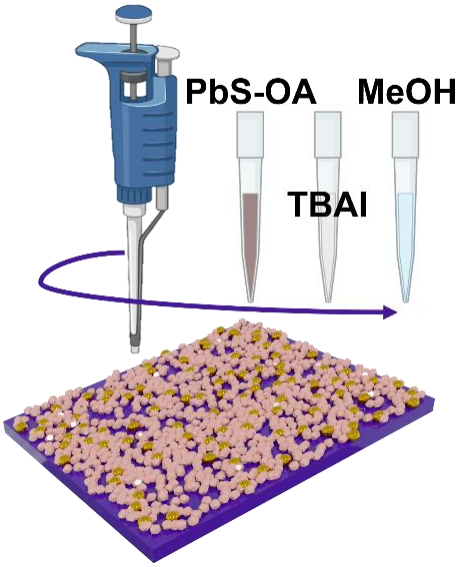

Figure 4.6. *Schematic of spin-coating PbS QDs on the substrate.*

4.5 Preparation of Au/Ag bimetallic nanostructure by sputter deposition

In Chapter 6, the HiPIMS technique is utilized for the deposition of Ag onto Au nanoarrays. As is shown in Figure 4.7, a custom HiPIMS deposition setup, developed by the Chair for Multicomponent Materials at Christian-Albrechts University in Kiel, are used. Central to this process is a vacuum chamber, which is crucial for maintaining a sputter-compatible environment. The procedure commences with the infusion of an inert gas, typically argon Ar, into the deposition chamber. This is

followed by the generation of a plasma, achieved by establishing a significant potential difference between a cathode (target material) and an anode, resulting in the ionization of the gas content of the chamber. The ionized Ar particles aggressively bombard the cathode, dislodging metal atoms from the target. Simultaneously, these ions release secondary electrons, which are propelled back into the plasma, where they ionize more gas atoms, thereby ensuring the continuity of the plasma. The dislodged metal atoms then accumulate on a substrate, forming a coherent metal layer.

Owing to the charged nature of ions, their speed and trajectory can be finely manipulated with magnetic fields. To this end, a magnet array is strategically positioned at the cathode to confine electrons close to the negatively charged target material, preventing them from indiscriminately hitting the substrate. This electron confinement significantly enhances the rate of deposition by ensuring a more efficient plasma maintenance.

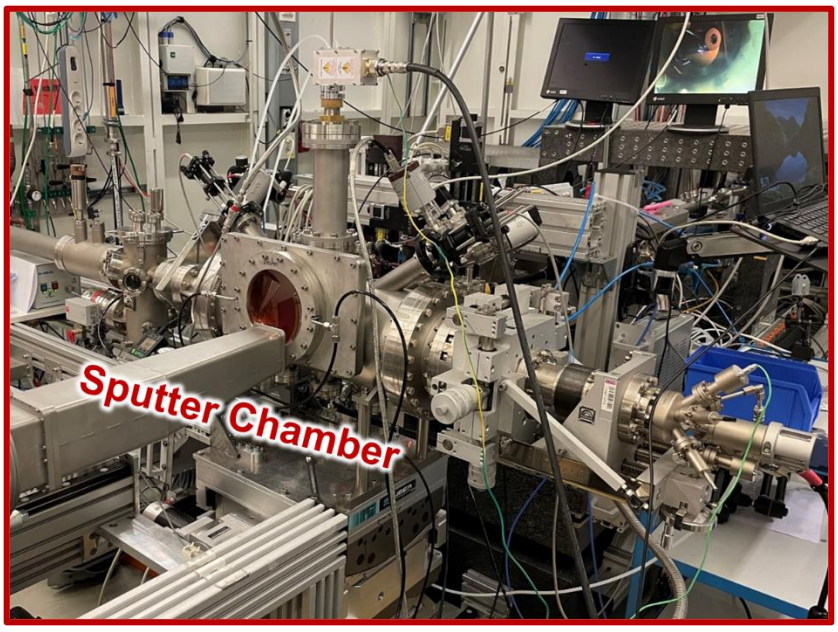

Figure 4.7. *HiPIMS deposition instrument from Christian-Albrechts University in Kiel, and settled at P03 beamline, DESY, Hamburg.*

For the sputter parameters in Chapter 6, include a pulse duration of 20 s at a frequency of 150 Hz, with the power set to 40 W. The applied voltage U is measured at 952 ± 4 V, and the peak current I is 1.41 ± 0.13 A cm^{-2}. The rate of deposition J, as determined by the Quartz Crystal Microbalance (QCM), is 0.306 pm 0.006 nm s^{-1}. The deposition duration is fixed at 20 s, achieving an effective film thickness of approximately 6.12 nm.

5 Synthesis and self-assembly of multi-sizes Au NPs

This thesis aims to fabricate the hybrid plasmonic nanostructures based on self-assembled Au NPs and explore their applications. In this chapter, the synthesis and self-assembly of multi-size Au NPs are discussed, examine their optical properties and surface morphology, and determine their sizes. Kyriaki N. Gavriilidou and Dong Li (FUNSOM, Soochow University) were involved in the synthesis of Au NPs and UV/Vis measurements. Peiran Zhang carried out the DLS measurements, while Kotone Tomioka contributed to the self-assembly of Au NPs. contributed to the DLS measurement. Additionally, the synthesized and assembled Au NPs is utilized in Chapters 6 and 7.

5.1 Optical properties

To meet the requirements of our applications, various sizes of Au NPs are synthesized: 10 nm, 20 nm, 30 nm, 50 nm, 60 nm, 70 nm, 80 nm, and 100 nm. The precise determination of the diameters and optical properties of these synthesized Au NPs is crucial, as their plasmonic characteristics significantly influence their performance in applications. Initially, the sizes of Au NPs are characterized with DLS and UV/Vis spectroscopy results.

5.1.1 DLS

The particle diameters of the synthesized Au NPs are first characterized by DLS analysis to check the synthesis process in a good condition. To give an example for the diameter calculation by DLS, as is shown in Figure 5.1, the decay rate T obtained from DLS measurements of particles with an estimated size of 30 nm is plotted against the squared momentum transfer (q^2), calculated using Equation 3.9. The observed linear relationship between the two variables confirms the correlation described in Equation 3.10, indicating that the nanoparticles are monodisperse and

diffuse. The slope of the linear fit provides a diffusion coefficient $D = (1.015 \pm 0.020) \times 10^{-11}$ m^2 s. When applied this value to the Stokes-Einstein equation (Equation 3.11), yields a hydrodynamic radius for the particle. The calculated diameter is d = 32 ± 2 nm. The deviation primarily arises from the linear fit function. The results obtained from DLS measurements for all synthesized Au NPs with different seeds amounts are summarized in Table 5.1.

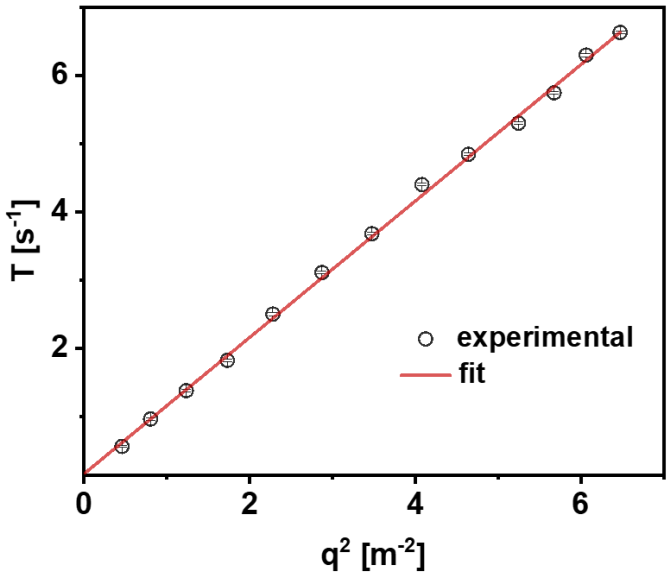

Figure 5.1. *Linear fit from the obtained experimental data with DLS for determination of the diffusion coefficient D for 30 nm particles.*

Table 5.1. *The amount of Au Seeds used for the Au NPs synthesis and calculated NPs sizes with DLS.*

Seeds (nm)	Amount (mL)	Diameter (nm)
3-5	0.2	12 ± 1
3-5	0.12	23 ± 1
10	2	32 ± 2
10	0.5	52 ± 3
20	2	63 ± 3
20	1.5	73 ± 4
20	1	82 ± 4
20	0.5	98 ± 5

5.1.2 UV/Vis spectroscopy

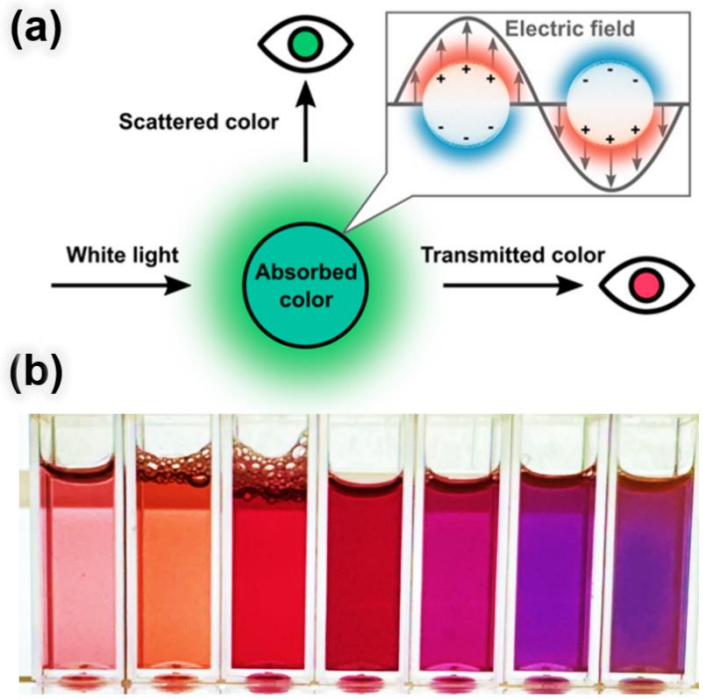

Figure 5.2. *Illustration of the absorbed, transmitted, and scattered color of Au NPs [39] and Synthesized Au NPs in cuvette for UV/Vis measurement. From left to right: 10 nm, 30 nm, 50 nm, 60 nm, 70 nm, 80 nm, and 100 nm. Copyright 2021 American Chemical Society.*

Figure 5.2 presents diluted solutions of synthesized Au NPs of various sizes for the UV/Vis measurement. The differences in color are visibly discernible to the naked eye. As shown in Figure 5.2, an observer positioned in line with the light source perceives the transmitted light, which is affected by both absorption and scattering effects. Consequently, the color of the colloidal nanoparticle solution in this context is governed by extinction. Thus, the extinction results of the Au NPs are corresponding to green light. As particle size increases from left to right, smaller particles exhibit a wine color, which transitions to dark red and eventually to dark purple with larger particle sizes. To minimize the limitations arising from solvent interactions, water is used as the solvent, as its effect is considered negligible for nonpolar components in a polar medium.

The UV/Vis absorption spectra are shown in Figure 5.3. The Au NPs with expected diameter of 10 nm exhibites a narrow peak with a λ_{max} at 519 nm corresponding to green light, whereas color capture by naked of the observer is wine red. As previously discussed in Section 2.2, when the size of Au NPs is significantly smaller than the

wavelength of the incident light, it induces the LSPR effect. This phenomenon results from the coherent oscillatory displacement of electrons within the metal nanoparticles, causing them to scatter and absorb specific wavelengths based on their size and material properties [75].

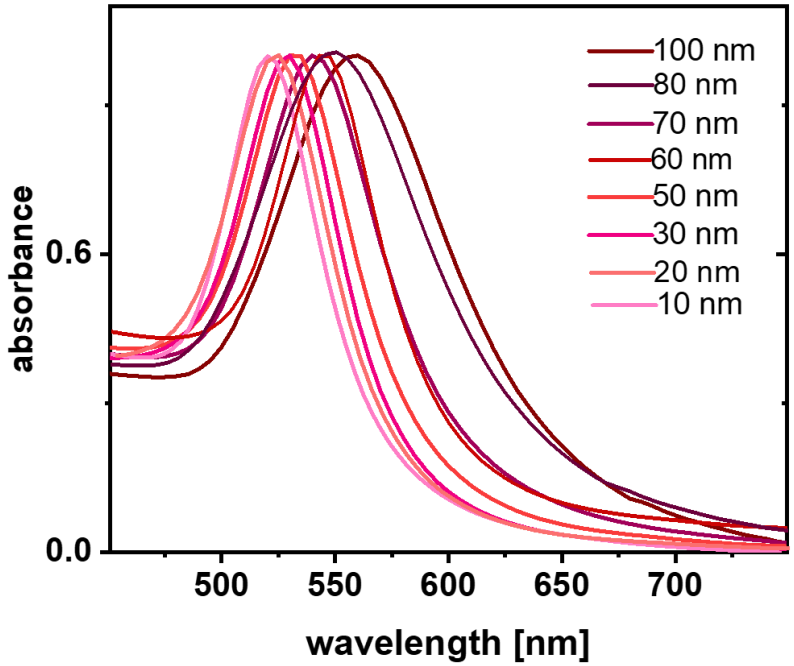

Figure 5.3. *UV/Vis absorbance spectra of synthesized Au NPs from 10 nm to 100 nm.*

Table 5.2. *Converted diameters of the Au NPs from the absorption peaks with UV/Vis Spectroscopy.*

Diameter DLS (nm)	UV/Vis peak (nm)	Converted Diameter (nm)
12 ± 1	519 ± 1	12 ± 0.5
23 ± 1	524 ± 1	21 ± 0.5
32 ± 2	528 ± 1	30 ± 0.5
52 ± 3	536 ± 2	51 ± 1
63 ± 3	541 ± 2	62 ± 1
73 ± 4	547 ± 2	70 ± 1
82 ± 4	551 ± 2	82 ± 1
98 ± 5	564 ± 2	97 ± 1

As the particle size increased from 10 nm to 100 nm, the absorption spectrum peak exhibited a red shift and broadening. To obtain more quantitative results, the size of the Au NPs can be estimated from the maximum wavelengths of the absorption spectra. According to the Beer-Lambert law, as stated in Section 3.2, these results are summarized in Table 5.2.

5.2 Surface morphology of self-assembled Au NPs

To further investigate the applications of synthesized Au NPs, it is crucial to constructing a high-organized Au nanoarrays. This configuration aims to fully explore the potential applications of these NPs in various fields, such as catalysis, sensing, and optoelectronics [76, 77]. The self-assembly of Au NPs is an effective method for fabricating Au nanoarrays, as it allows for precise control over the spatial arrangement of the NPs, which can significantly influence their plasmonic properties. In this study, two distinct assembly methods are used to fabricate Au nanoarrays: electrostatic absorption and phase interface transfer.

Electrostatic absorption involves utilizing the electrostatic forces between charged Au NPs and the substrate to form a uniform array. This method typically requires the functionalization of the substrate or the NPs with charged groups to facilitate strong electrostatic interactions. This technique is particularly useful for creating highly ordered nanoarrays. Phase interface transfer, on the other hand, exploits the differences in solubility and interfacial tension between two immiscible phases to assemble Au NPs at the interface which can achieve dense and well-organized nanoarrays. Figures 5.4 and 5.5 show SEM images of the self-assembled Au nanoarrays on Si substrates using electrostatic absorption and phase interface transfer methods, respectively.

Figure 5.4 reveals a highly ordered array of Au NPs, demonstrating the effectiveness of the electrostatic absorption method. The NPs are evenly distributed across the substrate, with minimal aggregation, indicating strong electrostatic interactions and uniform particle deposition. In contrast, the SEM image in Figure 5.5 shows the Au nanoarray fabricated using the phase interface transfer method. The image highlights the distinct pattern formation characteristic of this technique, with NPs tightly arranged on the substrate. However, the nanoarray does not fully cover the substrate and shows less uniformity, especially for the large sizes of Au NPs sample.

For applications in plasmonic structures, uniform plasmonic resonance can produce periodic hot carriers, which enhancing the plasmonic properties of the structure [78]. Additionally, a highly organized nanostructure is essential for X-ray scattering measurements, which are beneficial for characterizing hybrid plasmonic systems.

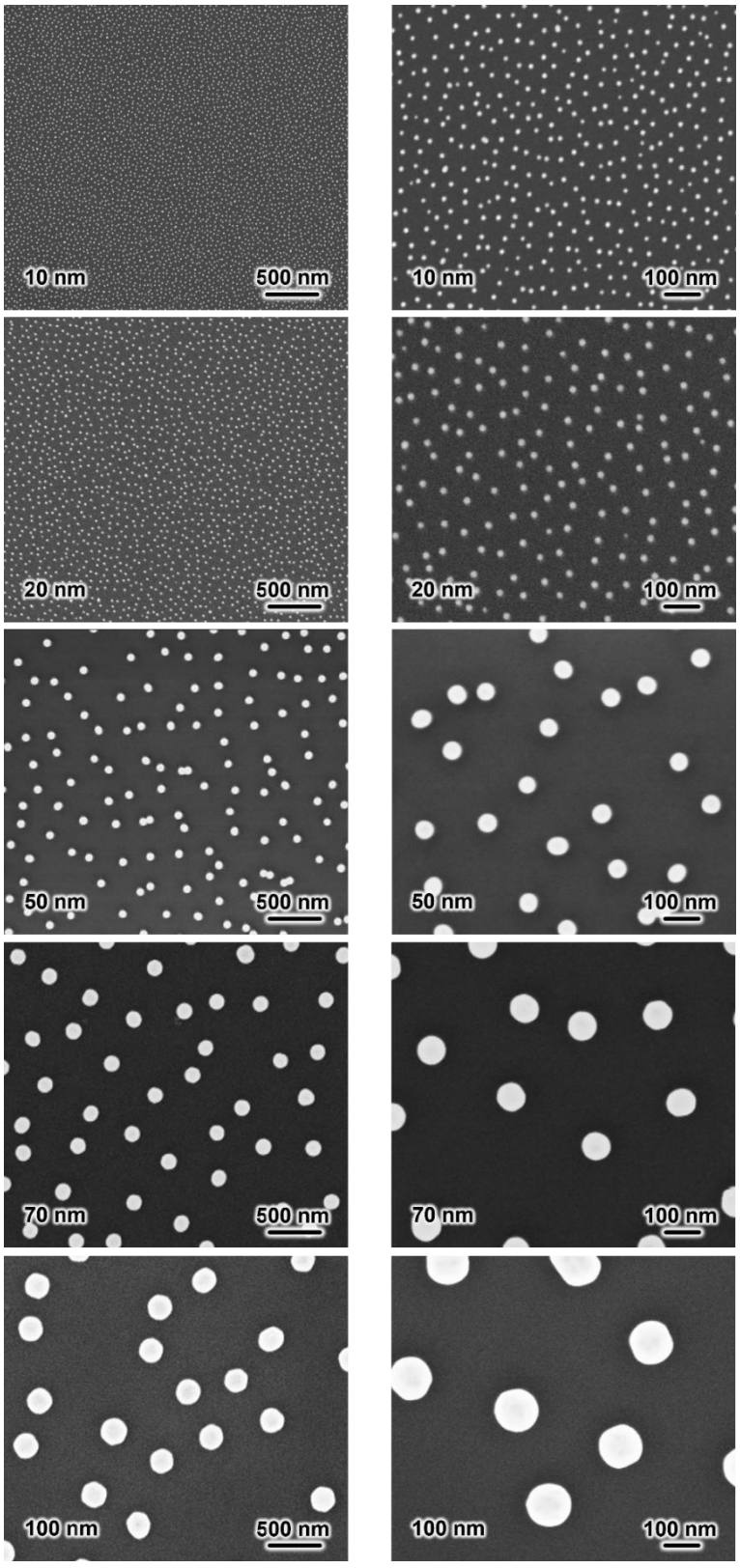

Figure 5.4. *SEM image of multi-sizes of Au NPs after electrostatic self-assembly.*

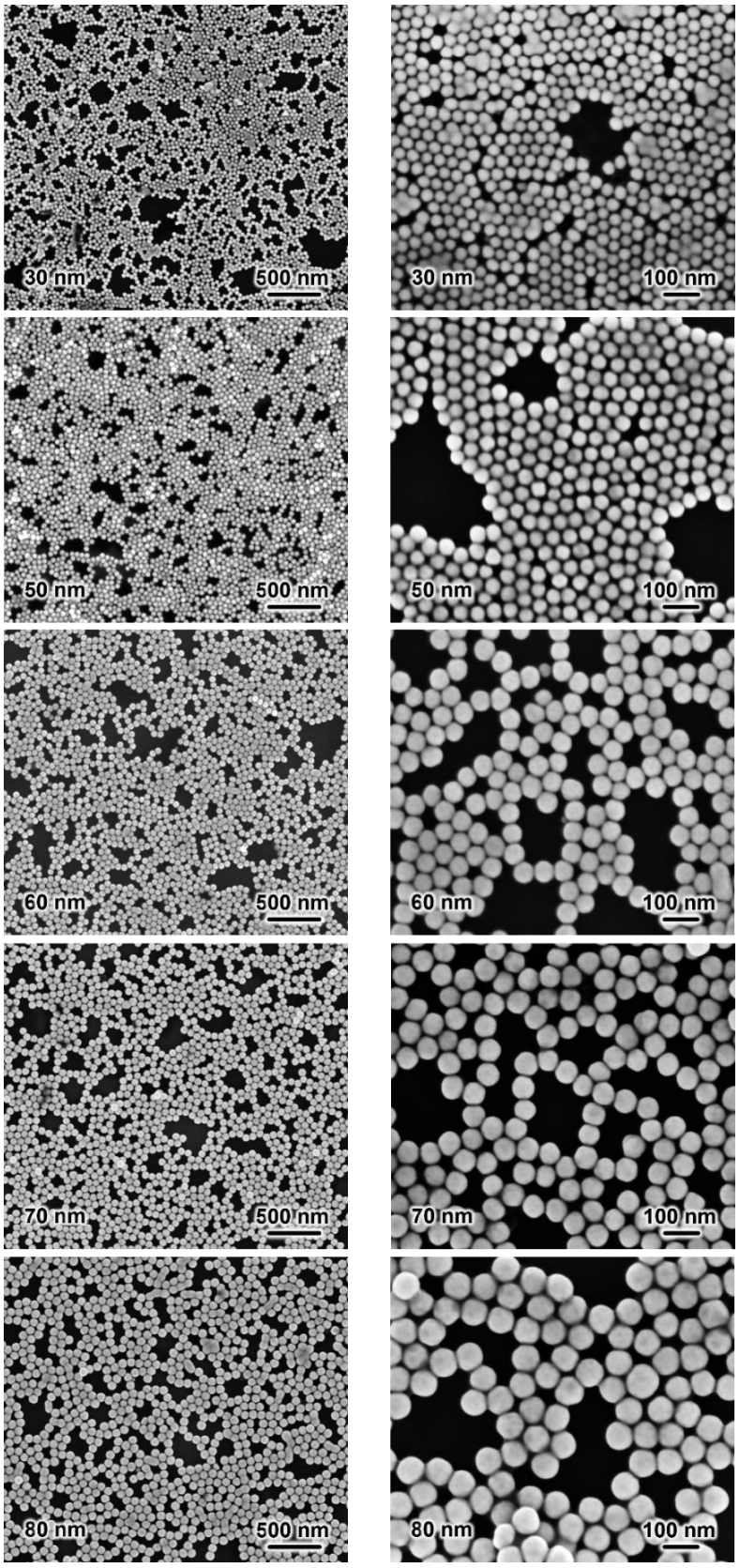

Figure 5.5. *SEM image of multi-sizes of Au NPs after phase interface assembly.*

5.3 Comparison of Au NPs sizes

In addition to their optical properties, the size and shape quality of Au NPs are crucial for their plasmonic properties. Therefore, it is essential to accurately determine the sizes of Au NPs before their application. While Section 5.1 focused on assessing the sizes through the DLS measurement of the Au NPs, this section details the determination of particle size using SEM images analyzed with ImageJ software.

The steps for obtaining the size distribution from SEM images using ImageJ are illustrated in Figure 5.6a-d. Firstly, the original SEM image is cropped to display evenly illuminated, non-overlapping particles. This step is essential for accurate analysis, as overlapping particles can lead to erroneous size estimations. Secondly, the nanoparticles are marked to set the threshold in the program, which involves adjusting the contrast and brightness to clearly distinguish the particles from the background. Finally, A size distribution histogram is created from the diameters of the outlined particles. This histogram provides a visual representation of the particle size distribution.

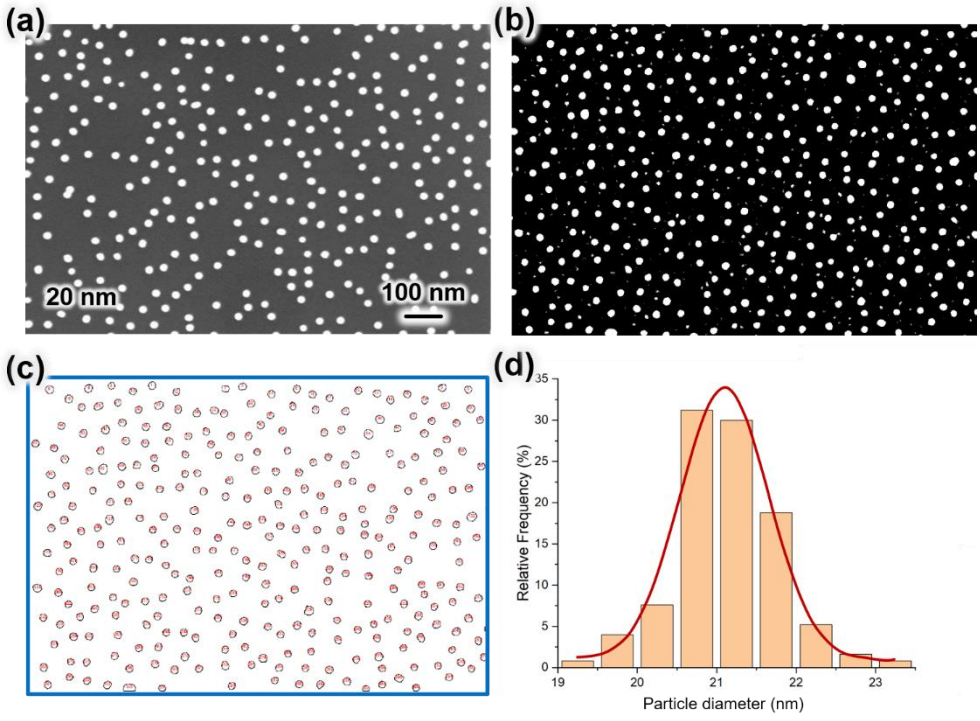

Figure 5.6. *Steps for obtaining the size distribution histogram. a) Select and crop the original SEM images. b) Particle set threshold to distinguish with the substrate. c) Marked all the particles and calculated their diameters. d) Size distribution histogram of calculated Au NPs.*

The diameters of the Au NPs calculated from the SEM images is given in Table 5.3. Compared to the diameters obtained from DLS, the diameters from SEM images show smaller size viewing due to the CTAB surface coating on the Au NPs leading to a large size conducted by DLS measurement.

Table 5.3. *Expected, DLS and SEM diameters of the Au NPs.*

Expected (nm)	DLS (nm)	SEM (nm)
10	12 ± 1	11 ± 1
20	23 ± 1	21 ± 1
30	32 ± 2	31 ± 1
50	52 ± 3	50 ± 2
60	63 ± 3	62 ± 2
70	73 ± 4	70 ± 3
80	82 ± 4	79 ± 3
100	98 ± 5	97 ± 4

5.4 Summary

In summary, this Chapter investigates the optical properties of synthesized Au NPs and analyzes the self-assembly outcomes of Au NPs using both electrostatic absorption and phase interface transfer methods. Initially, DLS is used to determine the diameters of synthesized Au NPs, ensuring the synthesis process is effective. Subsequent UV/Vis measurements are conducted to examine the plasmonic properties of the NPs. The results indicated that all sizes of Au NPs exhibited a distinct LSPR peak, confirming their uniformity and lack of aggregation.

To further explore the applications of synthesized Au NPs, two distinct assembly methods are utilized to fabricate Au nanoarrays: electrostatic adsorption and phase interface transfer. The electrostatically assembled NPs are evenly distributed across the substrate with minimal aggregation, demonstrating strong electrostatic interactions and uniform particle deposition. Conversely, the phase interface transfer method produced nanoarrays with characteristic pattern formations and tightly arranged NPs on the substrate. However, these nanoarrays did not fully cover the substrate and

exhibited less uniformity, particularly for larger Au NP samples.

For the application of self-assembled Au nanoarrays in plasmonic structures, a highly ordered arrangement is crucial. Uniform plasmonic resonance can generate periodic hot carriers, thereby enhancing the plasmonic properties of the structure. Additionally, our fabrication process revealed that the phase interface transfer method is limited to a very small area, necessitating a large-scale fabrication technique for further applications. Consequently, the electrostatic method is selected as the preferred self-assembly technique for subsequent projects in this thesis.

The particle sizes are also determined by SEM images analyzed with ImageJ software. The resulting particle size distribution histogram ideally followed a normal distribution, characterized by a specific mean value and standard deviation, indicating good uniformity of the synthesized Au NPs. With accurate size measurements, a suitable Au NP sizes can select for further applications.

6 Sputter deposition Ag on Au nanoarray

This chapter is based on the published article: High-power impulse magnetron sputter deposition of Ag on self-assembled Au nanoparticle arrays at low temperature dewetting conditions [23]. Reproduced with permission from (Guan, T.; Liang, S.; Kang, Y.; Pensa, E.; Li, D.; Liang, W.; Liang, Z.; Bulut, Y.; Drewes, J.; Reck, K. A.; Xiao, T.; Guo, R.; Drewes, J.; Strunskus, T.; Schwartzkopf, M.; Faupel, F.; Roth, S. V.; Cortés, E.; Jiang, L.; Müller-Buschbaum, P., ACS Appl Mater Interfaces 2024, 16(30), 40286-40296. DOI: 10.1021/acsami.4c10726). Copyright 2024 American Chemical Society.

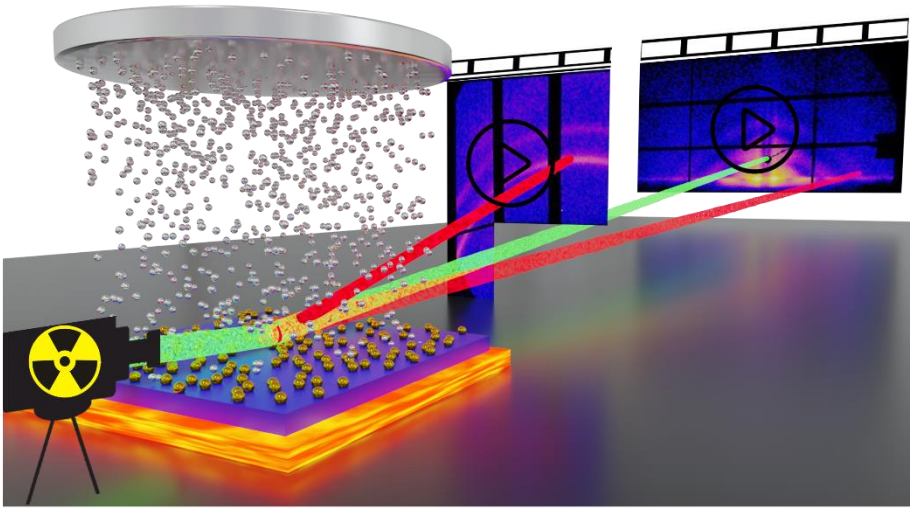

Plasmons have facilitated diverse analytical applications due to the boosting signal detectability by hot spots. In practical applications, it is crucial to fabricate straightforward, large-scale, and reproducible plasmonic substrates. Dewetting treatment, *via* applying a direct thermal annealing of metal films, has been used as a

straightforward method in the fabrication of such plasmonic nanostructures. However, tailoring the evolution of the dewetting process of metal films poses considerable experimental complexities, mainly due to nanoscale structure formation. In this Chapter, grazing incidence small- and wide-angle X-ray scattering are used for the *in situ* investigation of the high-power impulse magnetron sputter deposition of Ag on self-assembled Au nanoparticle arrays at low temperature dewetting conditions. This approach allows us to examine both, the direct formation of binary Au/Ag nanostructure and the consequential impact of the dewetting process on the spatial arrangement of the bimetallic nanoparticles. It is observed that the dewetting temperature at 100 °C is sufficient to favor the establishment of a homogenized structural configuration of bimetallic nanostructures (BMNs), which is beneficial for LSPRs. The fabricated metal nanostructures show potential application for the SERS detection of rhodamine 6G molecules. As SERS platform, BMNs formed with dewetting conditions turn out to be superior to those without dewetting conditions. The method in this work is envisioned as a facile strategy for the fabrication of plasmonic nanostructures.

6.1 Preface

Strongly enhanced light-matter interactions induced by LSPR originate from electromagnetic fields excited in the junctions between metallic nanostructures [78, 79]. A strategic structure design can tune the plasmonic properties, since the organization of metallic nanostructures offers the capacity to modulate plasmonic coupling interactions and thereby adjust their ability to enrich constructive hot spots [80, 81]. Due to these unique properties, metallic nanostructures are used for various applications such as solar conversion, analytics, data storage, and photocatalysis [82-86]. It is widely recognized that LSPR characteristics largely depend on the metal type and interparticle distance within the nanogaps formed by the metallic nanostructure [87-89]. To improve the plasmonic properties of these metallic nanostructures, an appropriate metallic composition and ensuring an optimal structural configuration are essential for enriching their applications.

Among the metals utilized in these applications, Au and Ag received significant interest due to their exceptional plasmonic properties [90, 91]. Both, Au and Ag exhibit minimal optical losses in the visible and near-infrared spectrums, high polarizability, biocompatibility, and versatility [92, 93]. Specifically, Ag is known for its superior enhancement properties, while Au is known for its excellent stability [94-96]. Another approach to enhancing the plasmonic properties involves integrating distinct metals onto a common substrate to construct a bimetallic or polymetallic plasmonic architecture [97-99]. Unlike monometallic systems, bimetallic Au/Ag configurations combine the advantages of each metal, thereby improving their

plasmonic properties [100]. Furthermore, creating periodic nanostructures is crucial for achieving consistent plasmonic properties, which enhances reliability and expands their capability for a wide array of applications [101, 102]. Thus, it is essential to pursue more efficient and scalable fabrication techniques for plasmonic metallic nanostructures.

The thermal annealing process of a metallic film, known as dewetting treatment, is widely utilized in various research areas to create plasmonic nanostructures [103, 104]. This method is particularly effective for generating metallic nanostructures over large areas. It also allows to produce bimetallic structures by annealing different metallic films together, leading to the development of multifunctional materials [105, 106]. However, controlling the morphology of the nanostructures precisely remains a challenge due to the random nature of the nucleation and growth processes involved in dewetting, which hinders the achievement of regular patterns [107, 108]. Despite these challenges, there has been significant focus on refining dewetting treatments to produce advanced plasmonic metal nanostructures. On the other hand, self-assembly offers a relatively simple alternative for crafting periodic nanostructures, with the additional possibility of forming multi-metallic structures by depositing various metal films on the self-assembled nanoarrays [9].

To optimize the use and potential applications of metal nanostructures, it is crucial to monitor their formation process. An *in situ* method with high-resolution is necessary to track the nanoscale growth process effectively. GIXS is a robust technique for analyzing nanoscale structures, offering high temporal resolution and exceptional data quality, making it a preferred choice for *in situ* analysis [70, 109]. GIXS is adept at determining the size, distribution, and crystal properties of metallic nanostructures during their formation and growth [110, 111]. It is particularly useful for observing the deposition of metal films and the subsequent development of nanostructures.

This chapter focus on creating BMNs on solid supports by using HiPIMS deposition of Ag onto Au nanoarray templates. Dewetting conditions are induced through moderate substrate heating during the sputtering process. The growth dynamics of these structures are examined using *in situ* GISAXS/GIWAXS. The effects of using 10 nm and 20 nm diameter Au NP arrays, with and without thermal annealing at 100 °C are explored. GISAXS/GIWAXS characterization discern the morphology and crystallographic features of the BMNs. The findings reveal that the structural organization and crystallinity of the Au/Ag composites are significantly improved under dewetting conditions. This study also allows us to meticulously track the evolution of Au/Ag nanostructures, assessing their size and distribution. For SERS applications, a deposition process that achieves a 2.5 nm gap is selected, with HiPIMS to deposit Ag for 10 s, achieving an effective thickness of approximately 3.06 nm. The SERS analysis shows that the 20 nm Au template under dewetting conditions offers the highest sensitivity for detecting R6G molecules, with a 49 % enhancement in

SERS intensity at the 1364 cm^{-1} peak compared to non-dewetted substrates. This research presents a viable method for fabricating binary or multi-component metal nanostructures with precise control over their dimensions and interparticle distances, offering innovative avenues for SERS platforms, color displays, catalysis, and other plasmonic-based applications. The approach and analytical techniques introduced here hold significant potential for broadening the scope of plasmonic research and enhancing the diversity of analytical methods in the field.

6.2 Morphology and crystallinity of Au nanoarrays

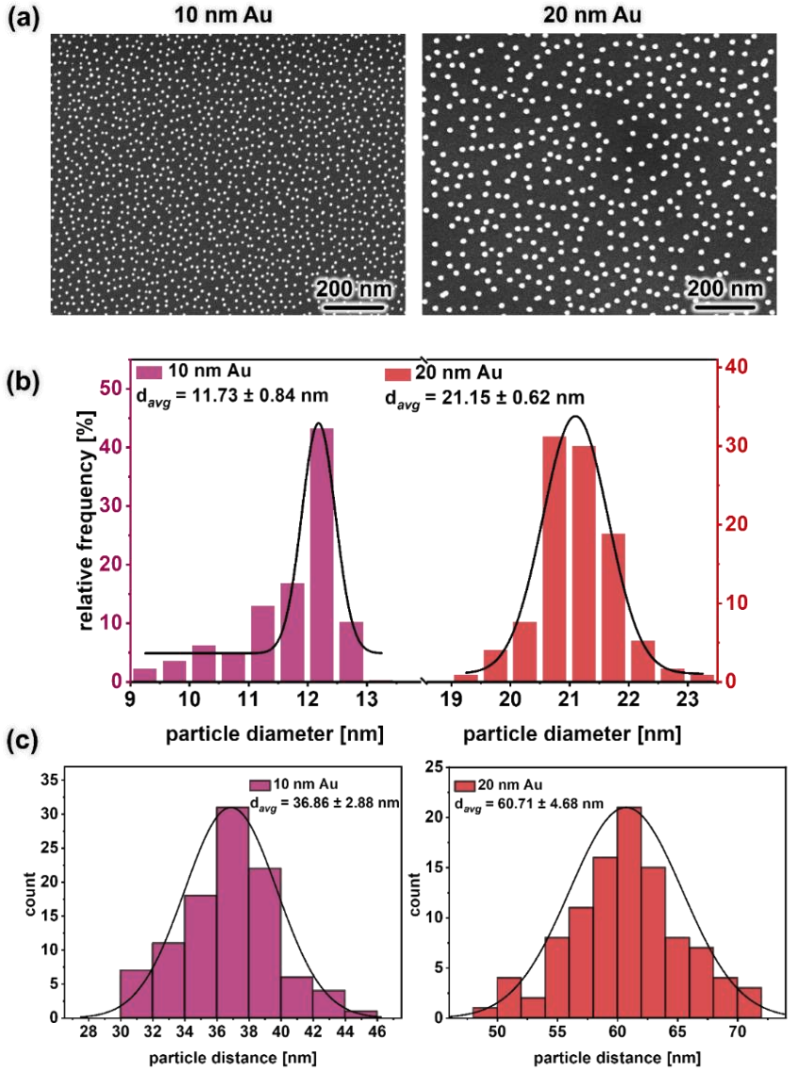

Figure 6.1. *(a) SEM images of self-assembled 10 nm and 20 nm Au NPs arrays. (b) Particle diameter distributions and (c) interparticle distance of the 10 nm and 20 nm NP arrays extracted from SEM images by ImageJ. Reproduced with permission from [23]. Copyright 2024 American Chemical Society.*

To investigate the impact of templates on the nanocomposites, the Au template with 10 nm and 20 nm Au nanoarrays on Si substrates are fabricated. The initial characterization of these Au NP arrays is conducted before delving into the analysis of the resultant Au/Ag bimetallic structures formed through HiPIMS. The organization of the Au NP arrays is assessed using SEM images (Figures 6.1a and b), which show a uniform distribution without noticeable clustering. Measurements derived from these images (Figure 6.1c) provide average particle diameters of (11.73 ± 0.84) nm for the 10 nm templates and (21.15 ± 0.62) nm for the 20 nm templates. This information is collected using the ImageJ software, as already discussed in Chapter 5. For clarity, refers to these templates by their nominal sizes of 10 nm and 20 nm in subsequent discussions.

The GISAXS data depicted in Figure 6.2a showcases periodic Bragg scattering signals in the horizontal direction at the Yoneda peak, corroborating the SEM findings and highlighting the exceptional size uniformity and spatial arrangement of the Au NP arrays. Additionally, the GIWAXS data in Figure 6.2b elucidates the crystalline characteristics of the Au NPs, with clear intensity rings at q_z positions around 2.64 $Å^{-1}$ and 3.05 $Å^{-1}$, which match the (111) and (200) crystal planes of gold. Intriguingly, the 10 nm Au NP arrays display a subtle peak near the (111) plane, hinting at less than optimal gold crystallization. In contrast, the 20 nm Au NP arrays demonstrate a significant crystalline presence, denoting enhanced crystallization. This evidence supports that the Au NP arrays formed through self-assembly are highly organized, making them excellent substrates for the creating of periodic BMNs, essential for further applications in various nanotechnology fields.

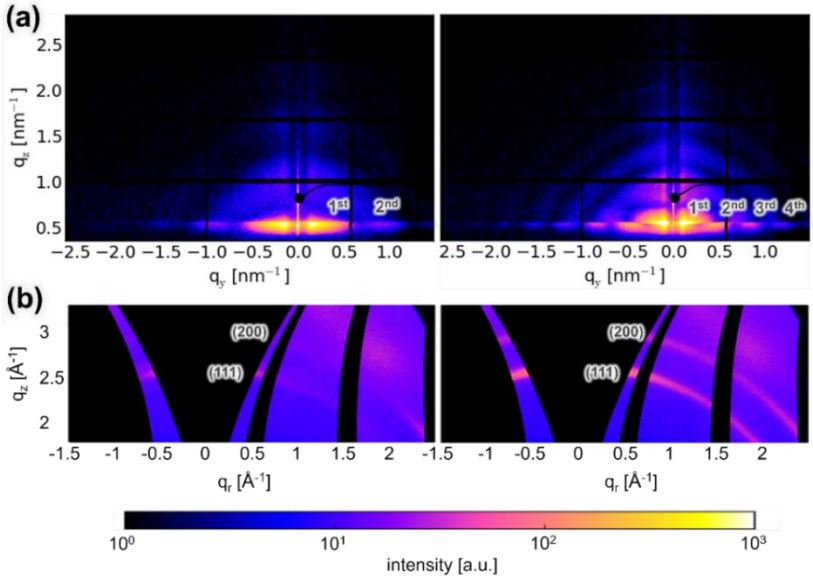

Figure 6.2. *2D (a) GISAXS and (b) GIWAXS data of both 10 nm and 20 nm Au NP arrays. Reproduced with permission from [23]. Copyright 2024 American Chemical Society.*

6.3 Set-up for *in situ* sputter deposition

The *in situ* GIWAXS/GISAXS analyses are conducted at the MiNaXS/P03 beamline of the PETRA III storage ring at DESY, Hamburg. Data acquisition is achieved using two detectors: a LAMBDA 9M, capturing 2 images per second with a pixel size of 55 µm (X-Spectrum, Germany), and a Pilatus 2M, capturing 20 images per second with a pixel size of 172 µm (Dectris Ltd., Switzerland). The sputter deposition process, with a rate of 0.306 nm/s and a substrate heating of 100 ℃, is executed using the HiPIMS system, with real-time monitoring through GIXS. To mitigate potential X-ray radiation damage, the sample is methodically moved perpendicular to the horizontal direction of the X-ray beam during the measurements. Illustrations detailing the configuration of the *in situ* measurement setup are displayed in Figure 6.3.

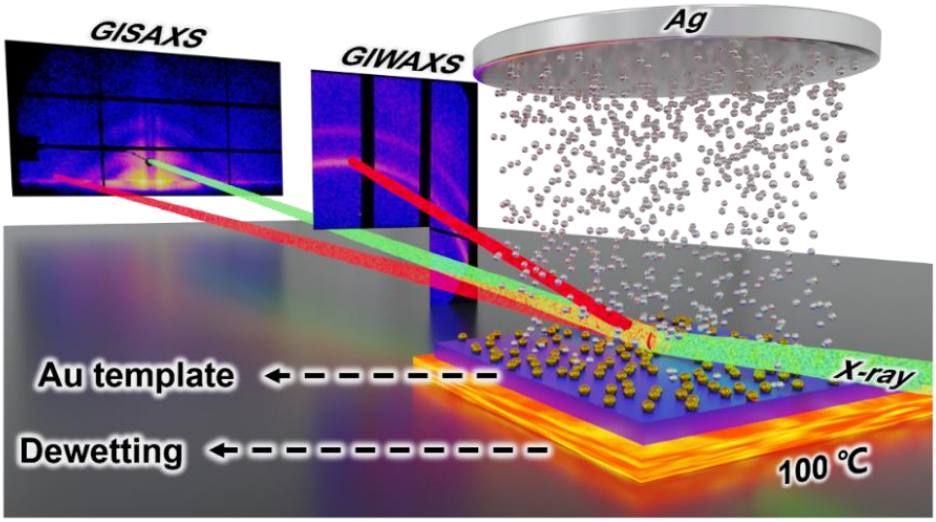

Figure 6.3. *Schematic of in situ HiPIMS deposition combined with in-situ GIWAXS/GISAXS measurements. Reproduced with permission from [23]. Copyright 2024 American Chemical Society.*

6.4 Crystallinity evolution of Au/Ag nanostructures

In addition to Au, Ag is another highly favored noble metal, celebrated for its exceptional plasmonic properties [112]. Therefore, Ag is selected as an additional metallic component to develop Au/Ag nanostructures using the HiPIMS deposition technique on the Au NP arrays, with a deposition rate of approximately 3.06 Å/s. To enhance the uniformity of the bimetallic plasmonic structure, an *in situ* thermal annealing step at a mild temperature of 100 ℃ during the sputter deposition process is

integrated. This method of using thermal dewetting conditions has been widely adopted in various studies for fabricating plasmonic nanostructures [113-115]. The moderate temperature used in our study for thermal annealing during deposition is sufficient to influence the structure formation.

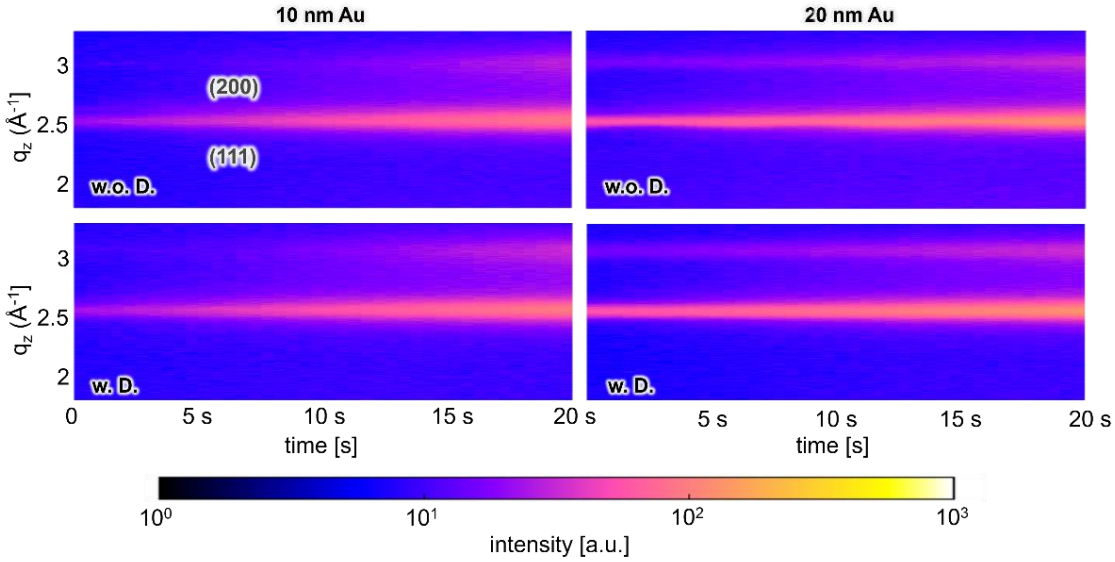

Figure 6.4. *Mapping of vertical line cuts from 2D GIWAXS data measured during the sputter deposition of Ag on 10 nm and 20 nm templates without and with dewetting conditions, respectively. Reproduced with permission from [23]. Copyright 2024 American Chemical Society.*

Figure 6.4 displays the GIWAXS temporal evolution for both 10 nm and 20 nm template samples under HiPIMS deposition. In comparison with the GIWAXS findings for pure Au NPs, the Au/Ag GIWAXS data exhibit two prominent intensity peaks, which are indicative of the (111) and (200) crystallographic planes of the Au/Ag structure. With the progression of Ag deposition, there is a noticeable increase in the intensity of these peaks, while the stability in their positions suggests the alignment of Ag crystal planes with those of Au, preventing any significant shifts in the peak positions.

The selected 2D GIWAXS data, shown in Figure 6.5, clearly demonstrates an increase in the intensity of two distinct crystalline rings, corresponding to the (111) and (200) planes, with increasing sputtering time. To provide a more intuitive comparison of the intensity changes, a cake cut is applied to the 2D GIWAXS data. As is shown in Figure 6.6, two prominent Bragg peaks corresponding to the (111) and (200) planes of Au/Ag are observed. As commonly reported, the intensity of the (111) peak surpasses that of the (200) peak. For the 10 nm template, the faint peak adjacent to the (111) diminishes with extended sputtering time, suggesting improved crystallization of the bimetallic structure [116]. Notably, under dewetting conditions during HiPIMS

deposition, these Bragg peaks exhibit increased intensity compared to those from samples without dewetting, indicating that thermal annealing enhances the crystallization process of the BMNs.

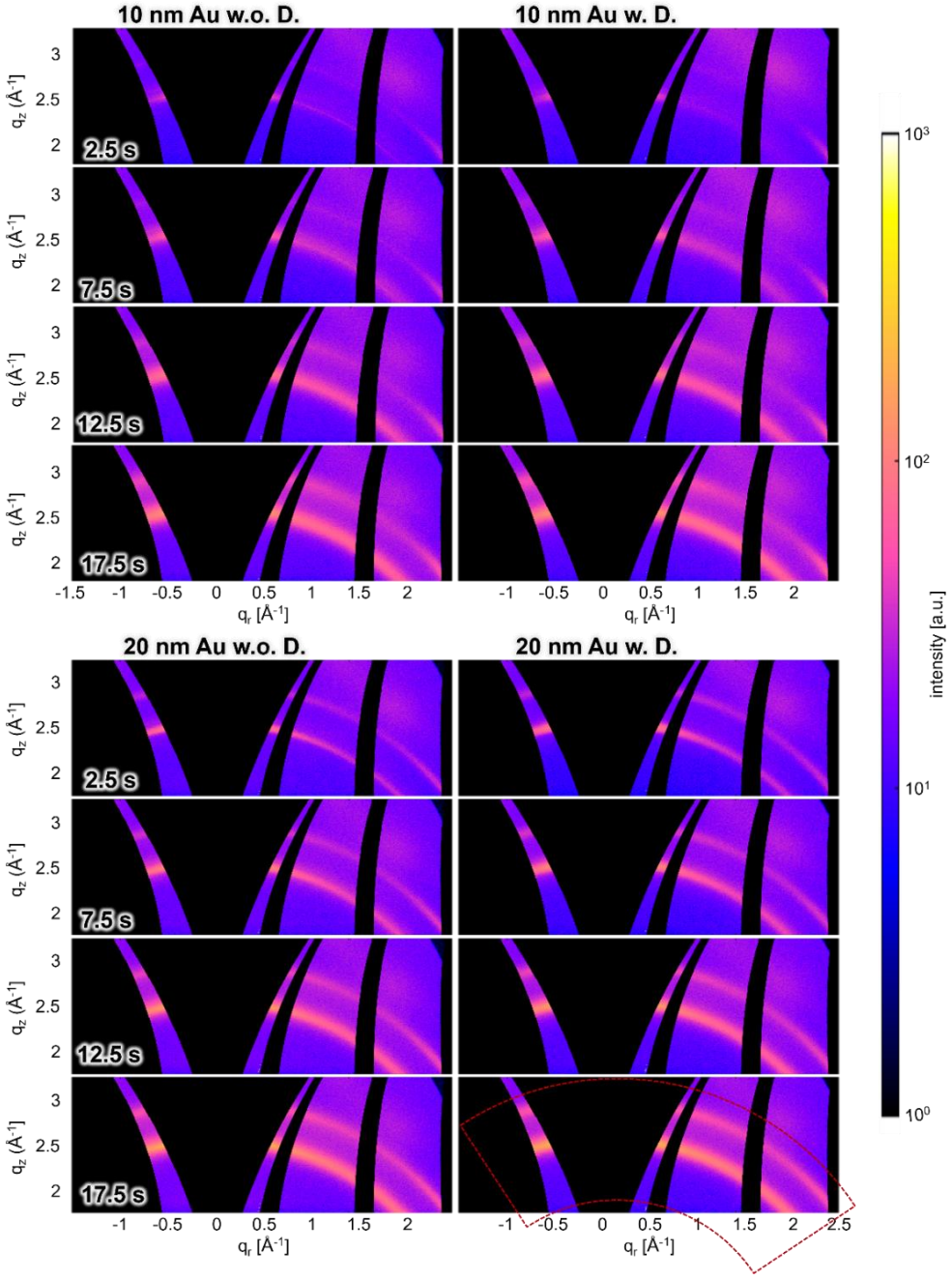

Figure 6.5. *Selected 2D GISAXS data of both 10 and 20 nm Au templates during the sputter deposition of Ag with and without dewetting conditions at selected Ag sputtering times as indicated. Reproduced with permission from [23]. Copyright 2024 American Chemical Society.*

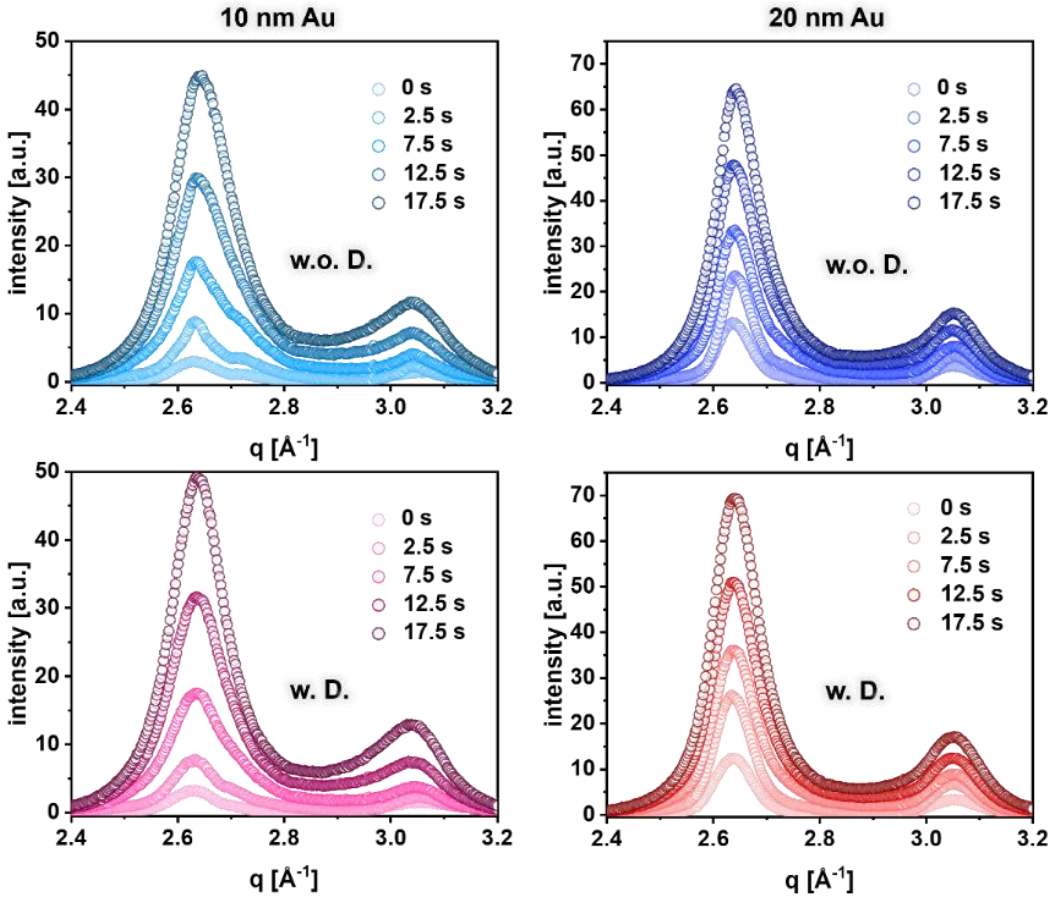

Figure 6.6. *Azimuthal integrations of selected 2D GIWAXS data collected during sputter deposition of Ag on both 10 nm and 20 nm templates without (w.o.) and with (w.) dewetting conditions at different sputtering times. Reproduced with permission from [23]. Copyright 2024 American Chemical Society.*

The sample subjected to sputter deposition with an Ag for 10 s is used as an example to examine the effects of dewetting treatment on crystallinity changes. Figure 6.7 presents the 2D GIWAXS data for 10 nm and 20 nm Au NP arrays post sputter deposition of Ag for 10 s (approximately 3.06 nm), both with and without dewetting treatments. Then the azimuthal integrations of the 2D GIWAXS data are evaluated. From Figure 6.7b, the increase in GIWAXS data intensity is noticeable, attributed to the thermal annealing process. The data peaks, fitted with a Gaussian function (indicated by the black line), demonstrate the high crystallinity of the (111) and (200) peaks. These findings clearly elucidate the enhanced crystallinity in the Au/Ag nanostructures due to thermal annealing, highlighting its significant impact on the stability and plasmonic properties of the materials. This underscores the benefit of using dewetting conditions in the synthesis of plasmonic nanostructures.

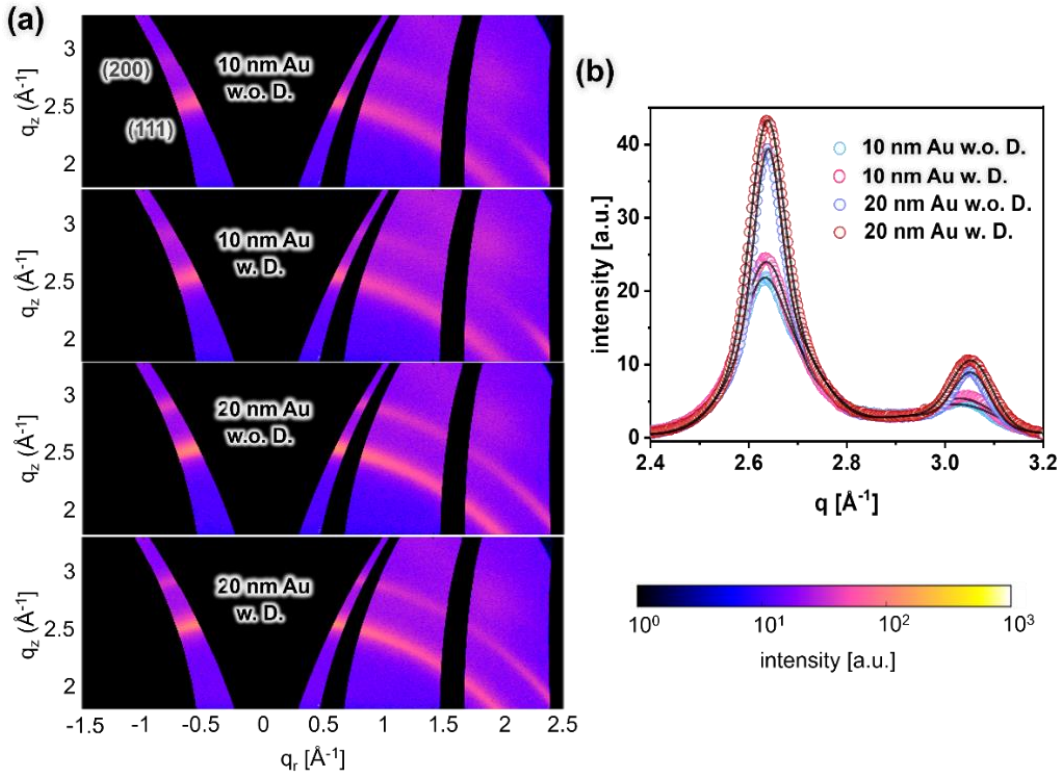

Figure 6.7. *(a) 2D GIWAXS data of both 10 nm and 20 nm Au NP arrays after sputter deposition of Ag for 10 s (ca. 3.06 nm) without (w.o.) and with (w.) dewetting conditions. (b) Azimuthal integrations of the 2D GIWAXS data shown in (a), the black line is the corresponding fits for both (111) and (200) peaks. Reproduced with permission from [23]. Copyright 2024 American Chemical Society.*

6.5 Morphology evolution of Au/Ag nanostructures

In addition to the crystallization characteristics, achieving precise spatial arrangement is essential for the development of superior plasmonic nanostructures. This precision is critically important for constructing SERS platforms, as detailed measurements of the dimensions and the spaces of the metallic structures between particles are crucial for establishing the most effective arrangement for interacting with target molecules [117, 118]. Therefore, it is necessary to conduct a methodical analysis of the growth of binary metallic nanostructures using advanced high-resolution techniques combined with computational models to accurately depict the form factor of the nanostructure. using GISAXS geometry stands out as a key method in this endeavor. A series of *in situ* GISAXS observations showcased collected at various HiPIMS deposition intervals, as demonstrated in Figure 6.8.

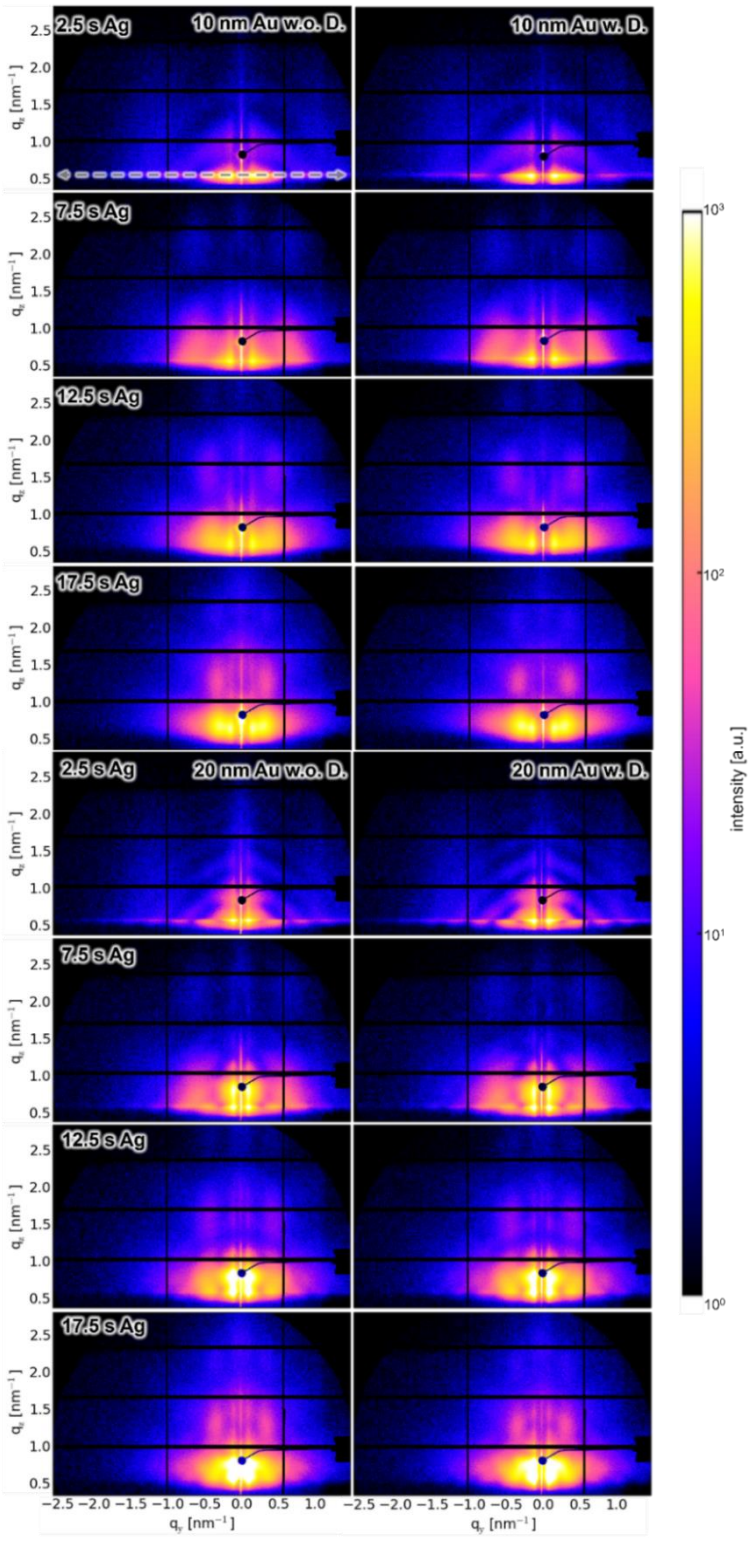

Figure 6.8. *Selected 2D GISAXS data of 10 and 20 nm Au templates during the sputter deposition of Ag without (w.o.) and with (w.) dewetting conditions at selected Ag sputtering times as indicated. Reproduced with permission from [23]. Copyright 2024 American Chemical Society.*

The analytical process for the Au/Ag BMN creation involves transforming the 2D GISAXS data into 1D plots through horizontal line cuts. Figure 6.9 presents time-resolved mappings generated from horizontal line cuts at the Yoneda peak for Au/Ag, illustrating the dynamic progression of significant scattering features and identifying two primary structural states: periodic and irregular regions. This comprehensive analysis not only enhances our understanding of nanostructure formation but also guides the optimization of nano-fabrication techniques to improve the efficiency and effectiveness of SERS platforms.

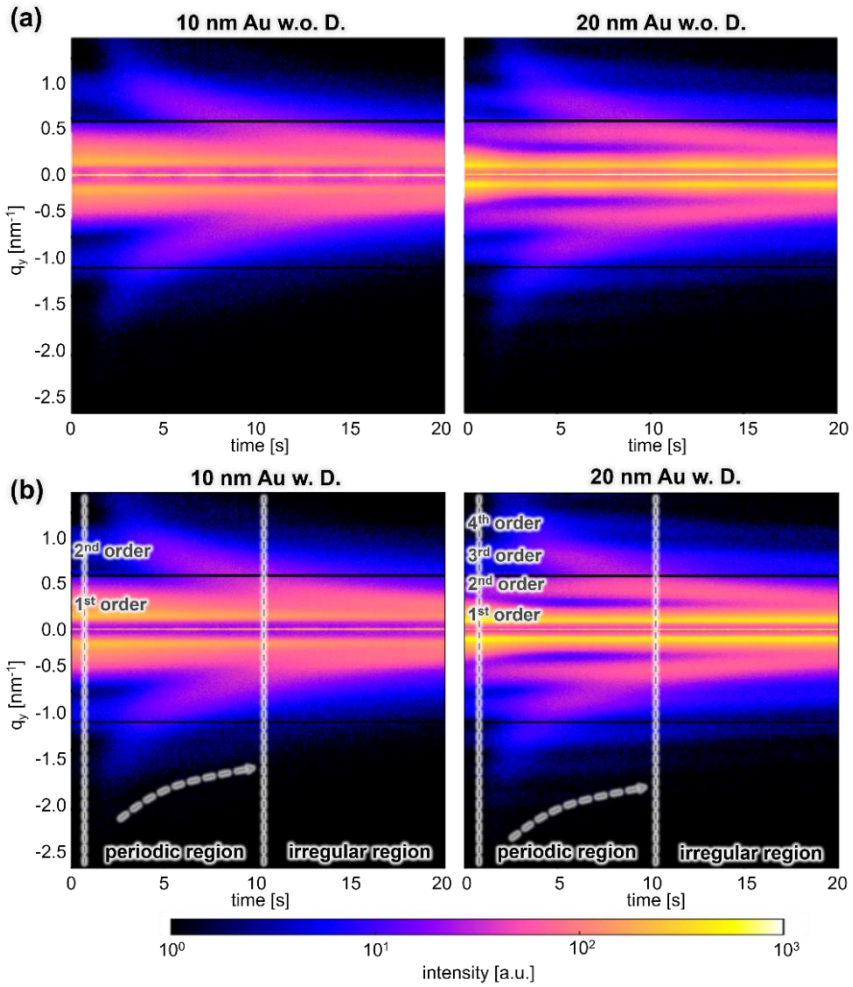

Figure 6.9. *Mappings of horizontal line cuts from 2D GISAXS data of 10 nm and 20 nm templates during the HiPIMS deposition of Ag (a) without and (b) with dewetting conditions. Reproduced with permission from [23]. Copyright 2024 American Chemical Society.*

From the commencement of the sputter deposition process, the mappings reveal uniformly spaced peaks across all the samples analyzed. Specifically, two distinct peaks are observed for the 10 nm Au NP arrays and four peaks for the 20 nm arrays. These peaks originate from the structured array of Au NPs and reflect the average

distance between particles within the Au nanostructure. As the deposition continues, a new Bragg peak feature, indicated by a dashed line, becomes apparent, primarily linked to the formation of Ag clusters. This peak associated with Ag clusters shifts towards lower q_y values as the deposition advances, indicating an increase in both the average distance between particles and the size of the particles. Moreover, the 1st order peak related to the Au NPs becomes narrower, suggesting that the Ag deposition contributes to the growth of the Au/Ag composite nanoparticles. After around 10 s of Ag sputter deposition (equivalent to an effective thickness of approximately 3.06 nm), the 2nd order peak of the 10 nm template merges into the 1st order peak.

A similar pattern is noted with the 20 nm sample, where the 3rd order peak progressively merges with the 2nd order peak during the Ag deposition, indicating a decrease in structural order within the BMN after about 10 s of Ag deposition. Thus, in this study, a 10 s HiPIMS deposition marks a critical transition in the periodicity of the Au/Ag BMNs, signaling a shift towards a less ordered structure. This observation is crucial for understanding the interplay between deposition time and nanostructure order, offering insights into optimizing the structural and functional properties of bimetallic nanoparticles for various applications.

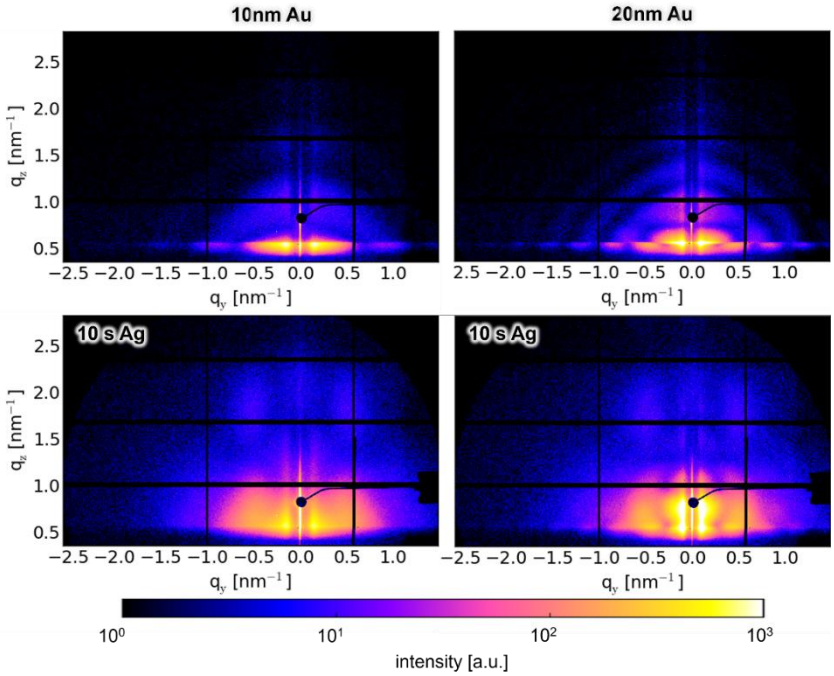

Figure 6.10. *2D GISAXS data of 10 nm and 20 nm Au templates with Ag sputter deposited for 10 s (effective thickness of ca. 3.06 nm) with dewetting conditions. Reproduced with permission from [23]. Copyright 2024 American Chemical Society.*

The 2D GISAXS data depicted in Figure 6.10 for the 10 nm and 20 nm templates, after Ag deposition for 10 s under dewetting conditions, supports the observed lack of periodic Bragg peaks compared to those seen in the bare Au NP arrays. Interestingly,

the GISAXS data for the 20 nm Au template shows more defined periodic intensity peaks than the 10 nm template, indicating a more ordered structure post 10 s Ag deposition. This increased orderliness in the 20 nm template is likely due to its larger size, which makes it less susceptible to alterations from Ag deposition, hence preserving its periodic structure. In SERS platform development, maintaining a structured nanoarchitecture is crucial as it facilitates consistent periodic signals, improving the sensitivity and stability of the platform [119, 120]. Moreover, minimizing the spacing between particles is vital for enhancing the performance of SERS platform [121, 122]. Thus, selecting an optimal nanostructure is key to achieving high-efficiency SERS detection. In this context, the 10 s Ag deposition timeframe is favored for its ability to produce the smallest interparticle distances in the periodic region, optimizing the HiPIMS deposition for effective SERS applications. This careful tuning of deposition time and nanostructure characteristics is instrumental in advancing the design and functionality of SERS platforms, potentially leading to breakthroughs in fields requiring sensitive molecular detection.

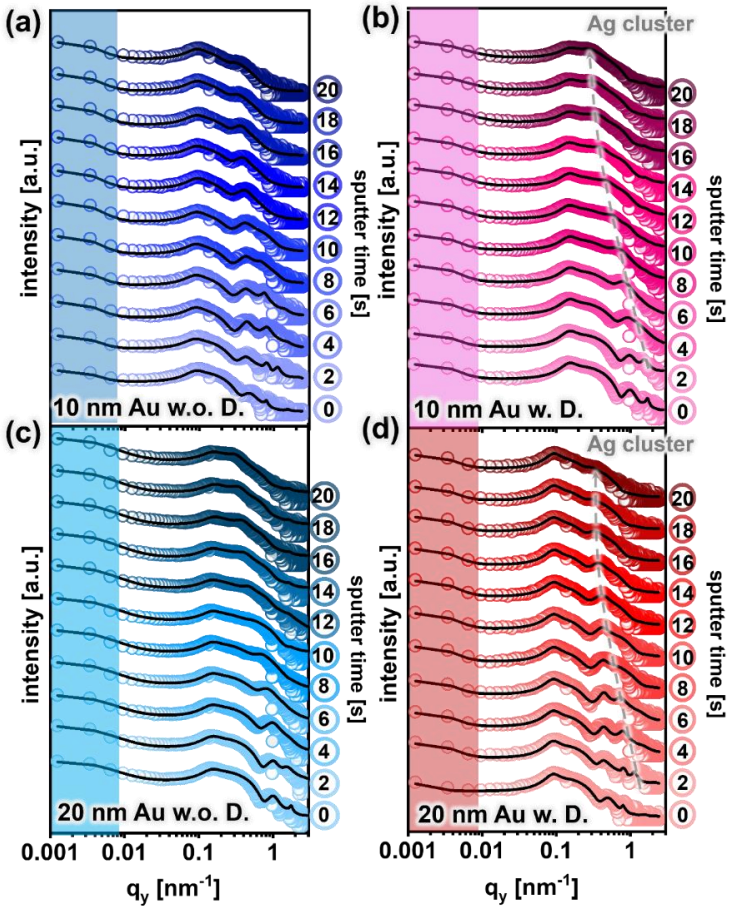

Figure 6.11. *Selected horizontal line cuts from 2D GISAXS data (symbols) are shown together with fits (lines) of both (a, b) 10 nm and (c, d) 20 nm Au templates during the in situ sputter deposition of Ag without (w.o.) and with (w.) dewetting conditions.*

For a detailed quantitative analysis of the spatial attributes of the Au/Ag BMNs, the GISAXS data are scrutinized using a theoretical model grounded in the DWBA as discussed in Chapter 2, which aids in precisely estimating the dimensions of particles and the gaps between them. Figure 6.11 showcase horizontal line cuts from the 2D GISAXS data, captured at 2 s intervals (corresponding to an effective thickness of about 0.61 nm). The experimental data (indicated by symbols) with the model fits (depicted by black lines) for both the 10 nm and 20 nm templates during Ag deposition are analyzed. The pristine Au NP arrays (illustrated in the bottom curves) display pronounced scattering peaks, indicative of a regular periodic structure. Shortly after the onset of the sputtering (as seen in the 2 s curve), a sharp peak emerges at a high q_y value (around 1.6 nm^{-1}), marking the scattering characteristic of the emerging Ag nanostructure. With ongoing sputter deposition, this Ag-related scattering peak gradually shifts to lower q_y values, reflecting the Ag clusters growth through coalescence (illustrated by a gray arrow). Additionally, the well-spaced peaks from the Au NP array blur, evolving from sharp peaks to broader, shoulder-like scattering features after 10 s of sputter deposition, indicating a loss of distinct periodicity in the binary structure with extended Ag deposition in HiPIMS.

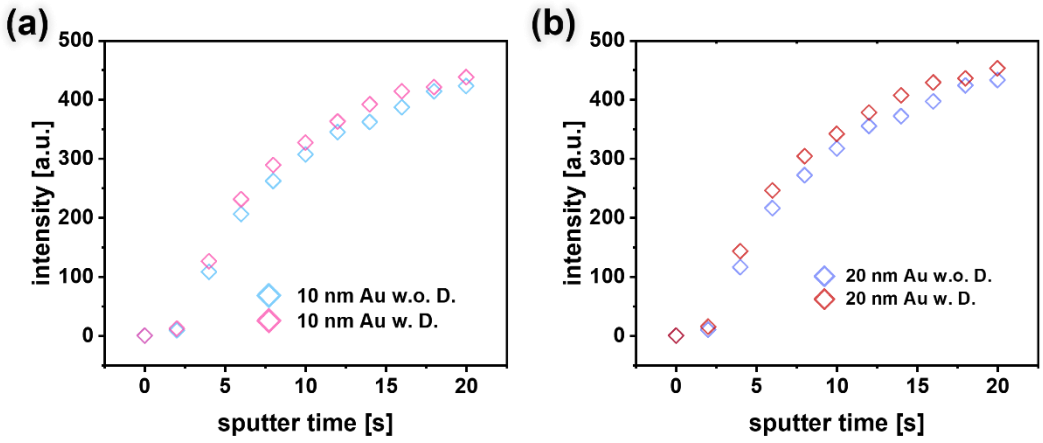

Figure 6.12. *Normalized intensities of the form factors used in the GISAXS modelling of Ag NPs between (a) 10 nm and (b) 20 nm Au NPs of the template during the sputter deposition of Ag with and without dewetting conditions. Reproduced with permission from [23]. Copyright 2024 American Chemical Society.*

Notably, under dewetting conditions, the scattering peak intensities from Ag clusters on both the 10 nm and 20 nm Au templates are markedly stronger (refer to Figure 6.12). These intensities in the GISAXS data primarily represent the scatterer count and their organization. Here, the heightened intensities denote an improved structural order, which is anticipated to favorably impact the SERS performance, enhancing the sensitivity and stability of the platform. This detailed structural analysis underscores the importance of precise deposition control and structural integrity in optimizing the

nanostructures for advanced SERS applications.

The progression of fit parameters, which include the dimensions and spacings between particles in the Au/Ag BMNs, is illustrated in Figures 6.13 and 6.14. These results reveal that the interparticle distances for both the 10 nm and 20 nm Au templates remain steady during the Ag deposition, implying that the Au nanoparticles act as regularly spaced nucleation points for the growth of bimetallic structure. Furthermore, an enlargement in the Au/Ag nanostructures size with prolonged sputtering time confirms the effective formation of the binary system. Under dewetting conditions, the Au/Ag structures are smaller than those formed without dewetting, indicating that substrate thermal annealing fosters a more orderly nanoparticle arrangement.

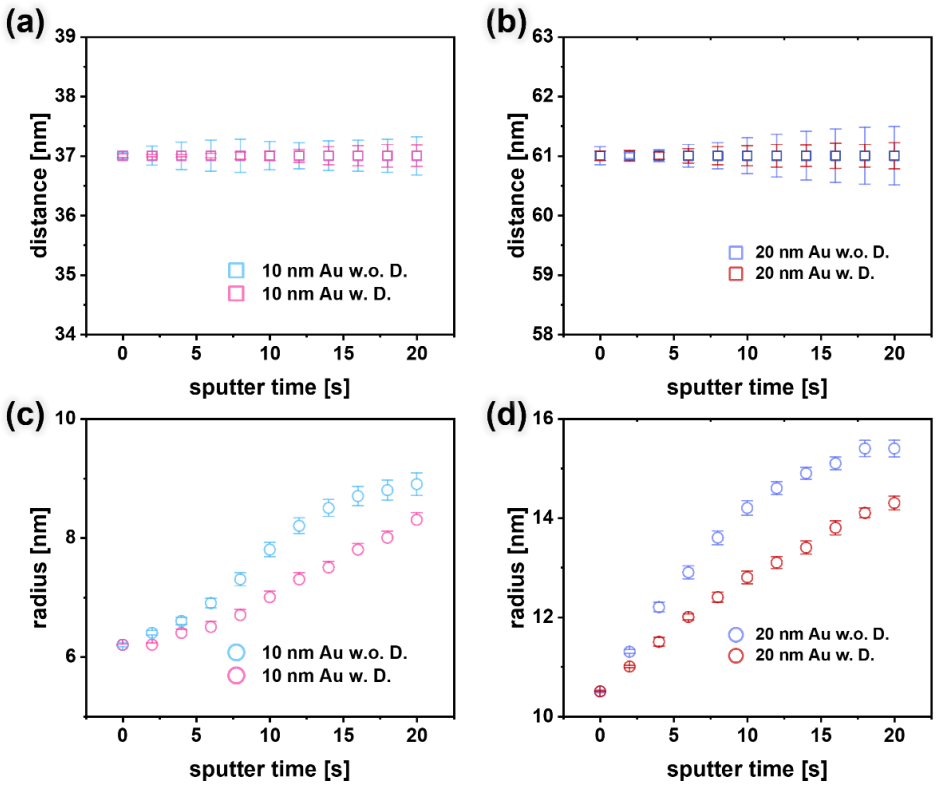

Figure 6.13. *(a, b) Interparticle distance and (c, d) radius of sputtered Au/Ag NPs on both 10 and 20 nm template extracted from GISAXS fit parameters. Reproduced with permission from [23]. Copyright 2024 American Chemical Society.*

Figure 6.14 detail the radius and center-to-center distances of isolated Ag nanoparticles situated amidst the larger Au/Ag structures. For both the 10 nm and 20 nm templates, the distance between these Ag nanoparticles expands with increased sputter duration. The Ag nanoparticles developed under dewetting conditions show a smaller radius and closer spacing compared to those formed without dewetting, a phenomenon attributed to the thermally driven surface diffusion of Ag nanoparticles. During the sputtering, Ag structures emerge from individual island grains, not from a

continuous film [123]. Due to a drive to reduce surface energy, Ag islands under dewetting conditions undergo a more uniform formation process, evolving into orderly nanoparticles. As a result, these nanoparticles are smaller in size compared to their non-dewetted counterparts and exhibit a higher density of nucleation sites, suggesting a more controlled and homogeneous growth.

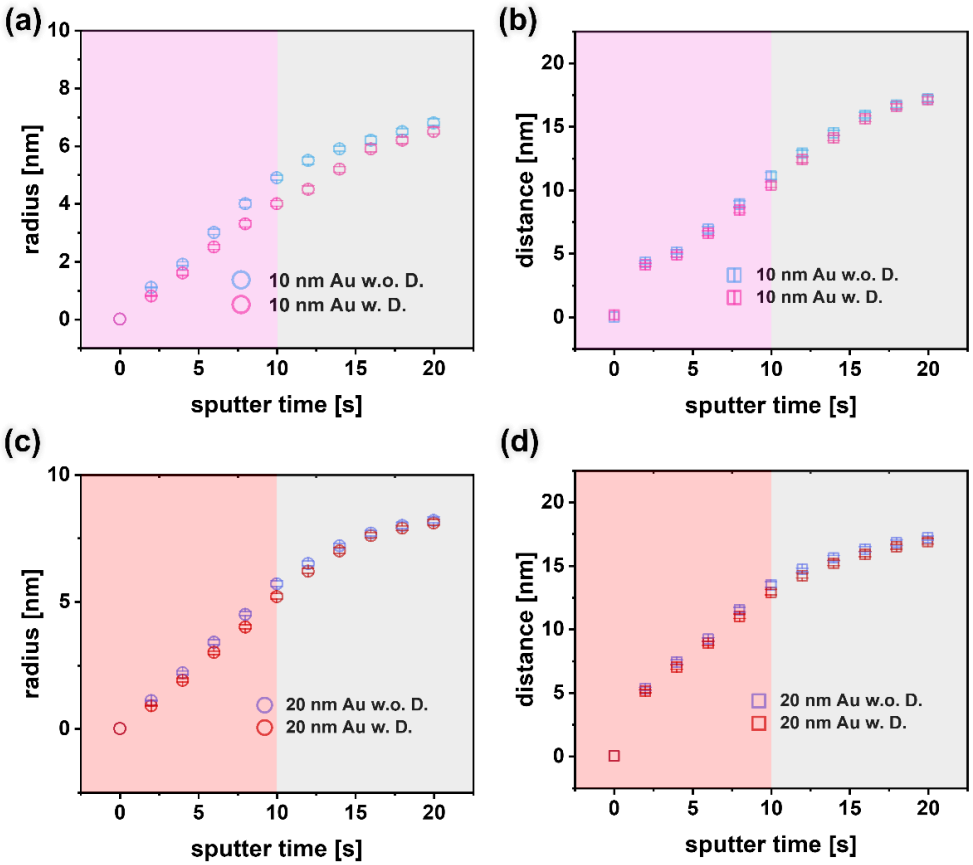

Figure 6.14. *(a, c) Radius and (b, d) interparticle distance of Ag NPs located between the Au NPs acting as template during the sputter deposition in case of the (a, b) 10 and (c, d) 20 nm templates as extracted from GISAXS fits. Reproduced with permission from [23]. Copyright 2024 American Chemical Society.*

In the realm of SERS platforms, the spaces between plasmonic structures are vital for the detection of target molecules. Figure 6.15 showcases the calculated interparticle gaps derived from our modeling parameters, where have achieved exceptionally narrow gaps, approximately 2.5 nm in width. This level of gap minimization is quite significant when compared to previous studies, as sub-3 nm gaps, like those achieved in our research, offer a competitive edge for SERS applications. Moreover, Figure 6.15b provides a top-view schematic of the model used in the GISAXS analysis, illustrating both the interparticle distances and the dimensions of a bare 20 nm Au nanoparticle array, along with its configuration after 10 s of Ag HiPIMS deposition.

The ability to achieve such narrow gaps is particularly crucial for enhancing the SERS

signal, as these small gaps can significantly increase the electromagnetic fields that boost the Raman signal of the target molecules [124, 125]. This enhancement is essential for the detection of low-concentration analytes, making our findings highly relevant for applications requiring high sensitivity and specificity. The detailed modeling and understanding of these nanostructures spatial characteristics pave the way for optimized SERS platforms that can be tailored for various analytical and diagnostic applications, potentially leading to advancements in plasmonic fields.

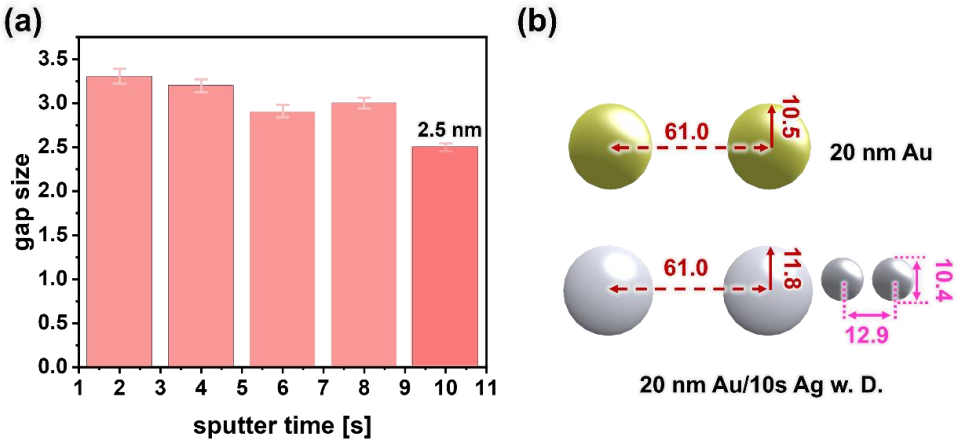

Figure 6.15. *(a) Gap sizes between Ag NPs of 20 nm template calculated from determined parameters. (b) Schematic structures (top view) of bare 20 nm Au NPs before (top) and after sputter deposition of Ag for 10 s Ag (bottom) as determined from the fit parameters. Reproduced with permission from [23]. Copyright 2024 American Chemical Society.*

6.6 Surface morphology of Au/Ag nanostructures

To validate our findings, *ex situ* SEM analyses are performed on Au templates with Ag deposited for durations of 5 s, 10 s, and 20 s. The SEM images display noticeable differences attributable to the dewetting conditions applied, indicating that our method of low-temperature thermal treatment at 100 °C effectively influences the results (as shown in Figures 6.16 and 6.17). Specifically, Figure 6.16 focus on the Au templates with 10 s of Ag deposition, and the images align with previous observations, showing a more organized structure for the Au/Ag BMNs under dewetting conditions compared to those not subjected to the thermal process. Moreover, the presence of a higher number density of Ag NPs interspersed among the larger Au/Ag nanoparticles is more pronounced under dewetting conditions. Notably, the 20 nm template demonstrates enhanced structural regularity compared to the 10 nm template, making it a preferable candidate for SERS applications.

Additionally, the geometry of a 20 nm Au template with a 10 s Ag deposition BMN is reverse schematic using the modeling parameters (illustrated in Figure 6.18b). The

modeling results align well with the SEM observations, reinforcing the accuracy and reliability of our GISAXS-based modeling approach. This congruence between the modeling and SEM data not only substantiates our methodological approach but also underscores the impact of controlled dewetting on achieving desirable nanostructural characteristics, which are crucial for optimizing the performance of SERS platforms. Such insights can significantly contribute to the advancement of nano-fabrication techniques tailored for sensitive and specific molecular detection.

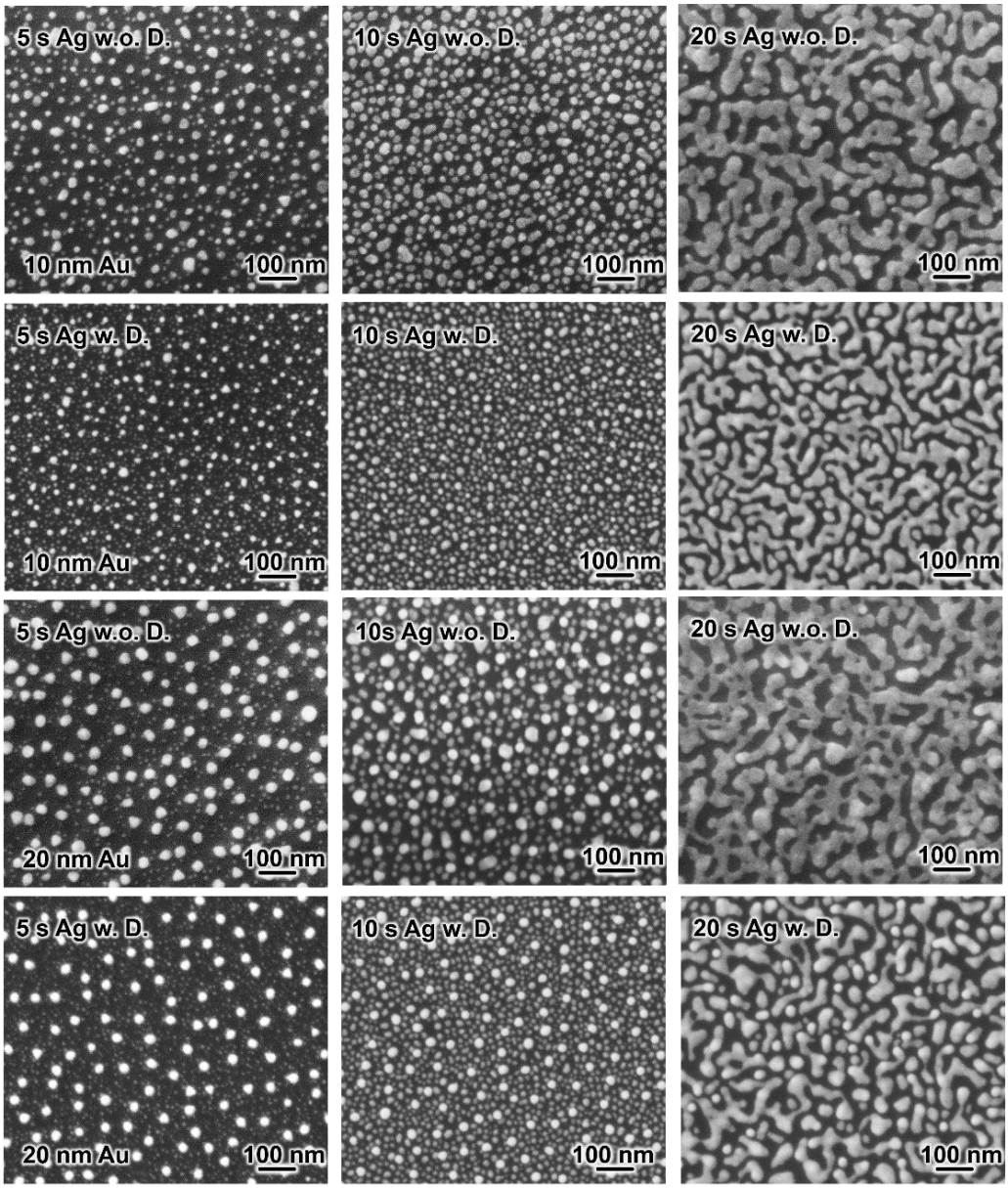

Figure 6.16. *SEM images of both 10 nm and 20 nm Au templates with Ag deposited for 5 s, 10 s, and 20 s Ag with and without dewetting conditions. Reproduced with permission from [23]. Copyright 2024 American Chemical Society.*

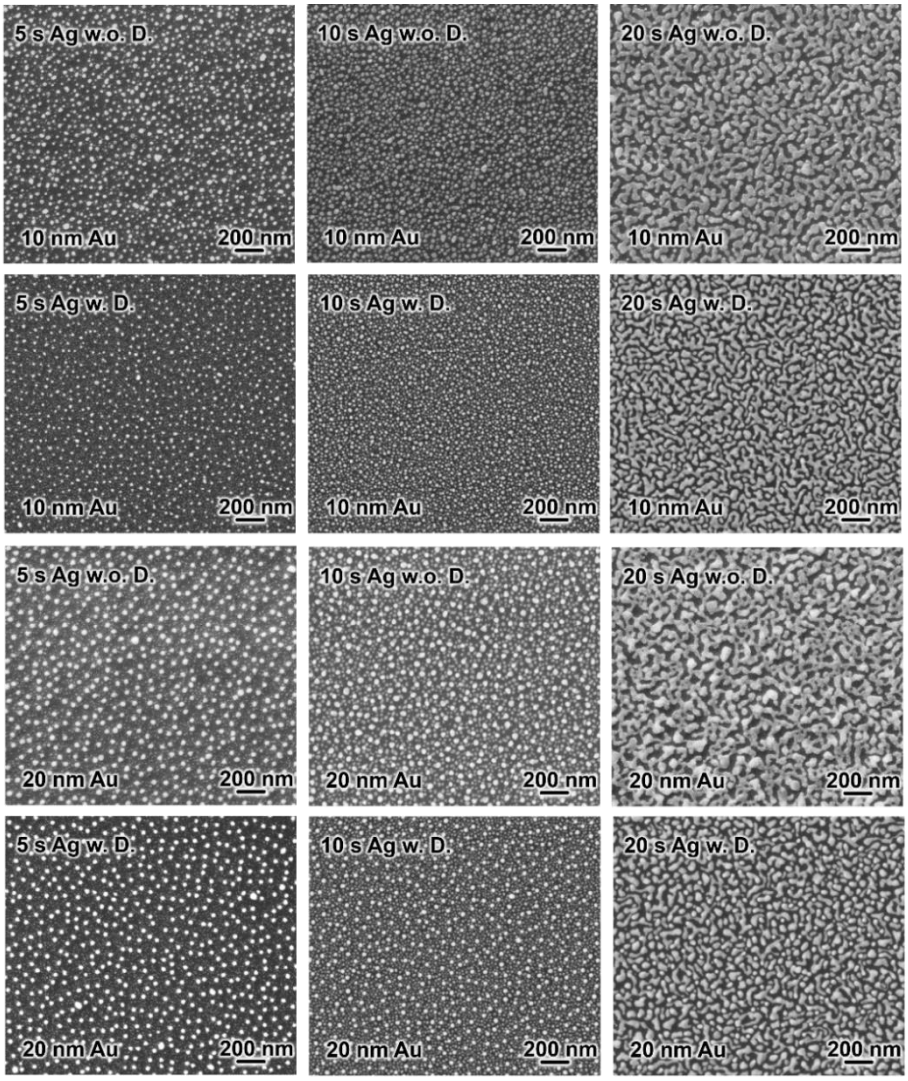

Figure 6.17. *SEM images of both 10 nm and 20 nm Au templates with Ag deposited for 5 s, 10 s, and 20 s Ag with and without dewetting conditions. Reproduced with permission from [23]. Copyright 2024 American Chemical Society.*

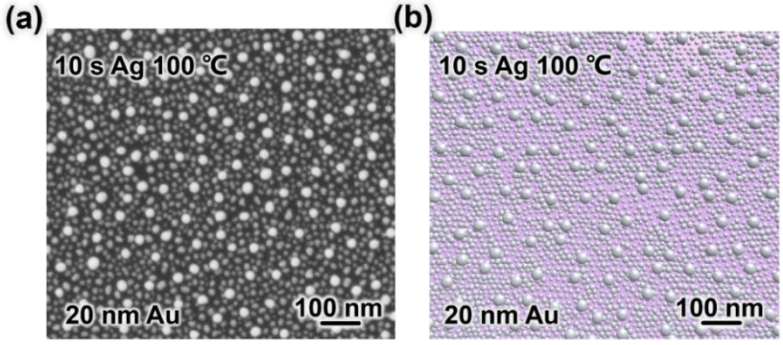

Figure 6.18. (a) SEM images and (b) *schematics of 20 nm Au template with 10 s Ag under 100 ℃ treatment. Reproduced with permission from [23]. Copyright 2024 American Chemical Society.*

6.7 SERS performance of Au/Ag nanostructures

To substantiate the potential use of the BMNs analyzed in this study, I conduct SERS measurements on the samples of Au template with HiPIMS deposition of Ag for 10 s. Rhodamine 6 G (R6G) is commonly used in SERS applications, with the detection method leveraging the technique's notable sensitivity and selectivity, offering rapid and non-destructive on-site analysis [126-129]. In this work, R6G is chosen as the target molecule for detection *via* SERS. The SERS spectral signals of R6G are clearly observed at a concentration of 10^{-4} M, as shown in Figure 6.19. Remarkably, the SERS signal from the samples subjected to the dewetting process showed an enhancement compared to those that are not heated. Specifically, the SERS intensity at the 1364 cm^{-1} peak for the 20 nm Au substrates treated with dewetting is enhanced by 49 % compared to the non-dewetted substrates. This result suggests that the dewetting conditions promote the formation of a more regular BMN, which in turn significantly improves the SERS performance.

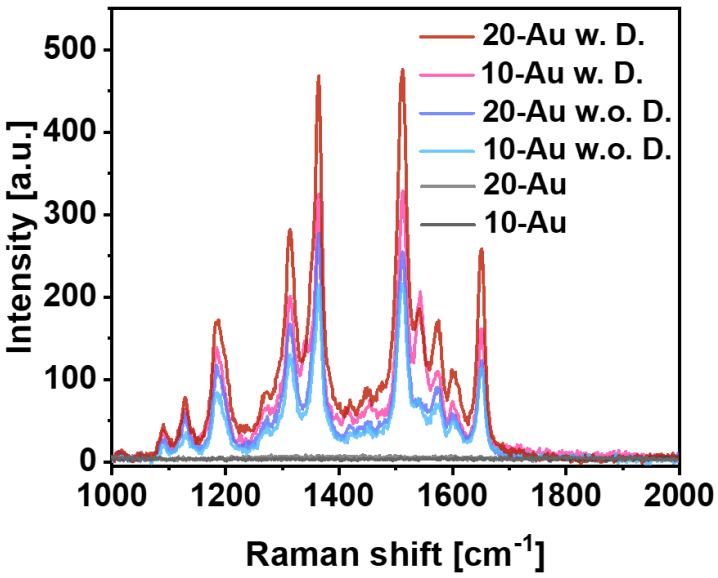

Figure 6.19. *SERS results of 10^{-4} M R6G molecule detected by 10 nm and 20 nm Au templates sputtered 10 s Ag with and without dewetting conditions. Reproduced with permission from [23]. Copyright 2024 American Chemical Society.*

Further, the relative standard deviation (RSD) for the 20 nm Au/10 s Ag substrates in relation to their SERS peak intensities at 1364 cm^{-1} and 1518 cm^{-1} are assessed. The substrates treated with dewetting conditions showed RSD values of 6.34 % and 5.96 %, respectively, as depicted in Figure 6.20. These values indicate a high degree of signal reproducibility compared to the substrates that did not undergo dewetting. This enhancement in signal reproducibility under dewetting conditions underscores the importance of controlled nanostructural formation for reliable SERS analysis.

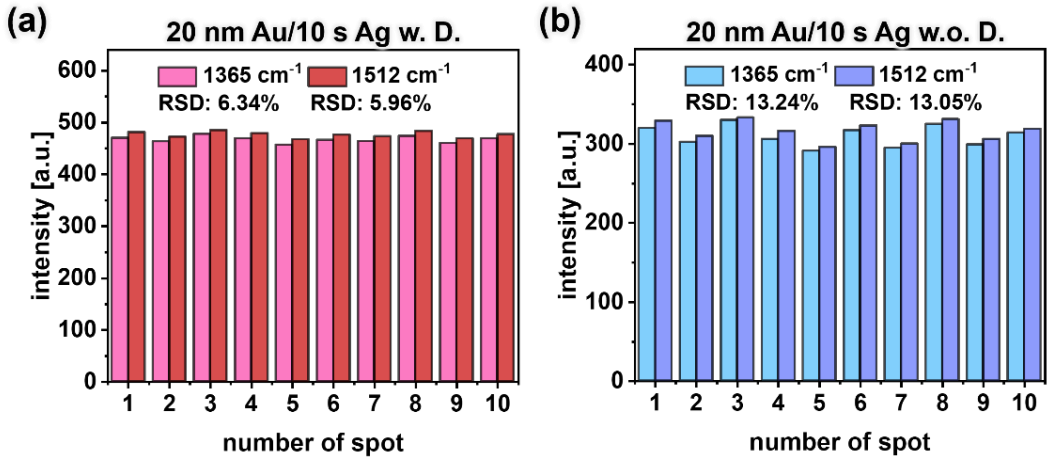

Figure 6.20. *20 nm Au template/10s Ag sputtering with dewetting treatment: RSD of both 1365 cm^{-1} and 1512 cm^{-1} signal of SERS as measured at 10 different spots. Reproduced with permission from [23]. Copyright 2024 American Chemical Society.*

6.8 Summary

In summary, this chapter details the creating of periodic binary metal nanostructures combining Au and Ag, achieved through HiPIMS Ag deposition onto a self-organized Au NP array under conditions promoting dewetting. The *in situ* X-ray scattering methods are applied to explore the formation processes of these BMNs. Analyzing the structure of 10 and 20 nm Au templates post HiPIMS Ag deposition, GIWAXS and GISAXS techniques are utilized to assess their morphology. The GIWAXS analysis highlighted an increase in crystallization within the Au/Ag structures, a result of the dewetting process induced by substrate heating. Further examination and modeling of GISAXS data provided insights into the nanostructure dimensions and interparticle spacing throughout the HiPIMS deposition stages. By modeling the interparticle distances, an optimal configuration is identified for SERS applications, involving a 10 s Ag deposition resulting in an approximate thickness of 3.06 nm. Utilizing these binary Au/Ag nanostructures for R6G detection demonstrated that the 20 nm Au NP array with a 10 s Ag deposition under dewetting conditions exhibited the most effective detectivity. This study not only introduces a novel method for constructing ordered binary plasmonic nanostructures but also significantly contributes to our understanding, aiding in the strategic design and evaluation of such structures for various applications. Consequently, our findings offer a robust framework for the advancement of binary plasmonic nanostructures, with potential applications in SERS platforms, color display technologies, catalysis, and beyond, indicating a significant technique in the field of plasmonic nanoengineering.

7 Hybrid Au/PbS nanostructure for photodetector

This chapter is based on the published article: High-power impulse magnetron sputter deposition of Ag on self-assembled Au nanoparticle arrays at low temperature dewetting conditions [28]. Reproduced with permission from (Guan, T.; Chen, W.; Tang, H.; Li, D.; Wang, X.; Weindl, C. L.; Wang, Y.; Liang, Z.; Liang, S.; Xiao, T.; Tu, S.; Roth, S. V.; Jiang, L.; Müller-Buschbaum, P., ACS Nano 2023, 17, 22, 23010-23019, DOI: 10.1021/acsnano.3c08526). Copyright 2023 American Chemical Society

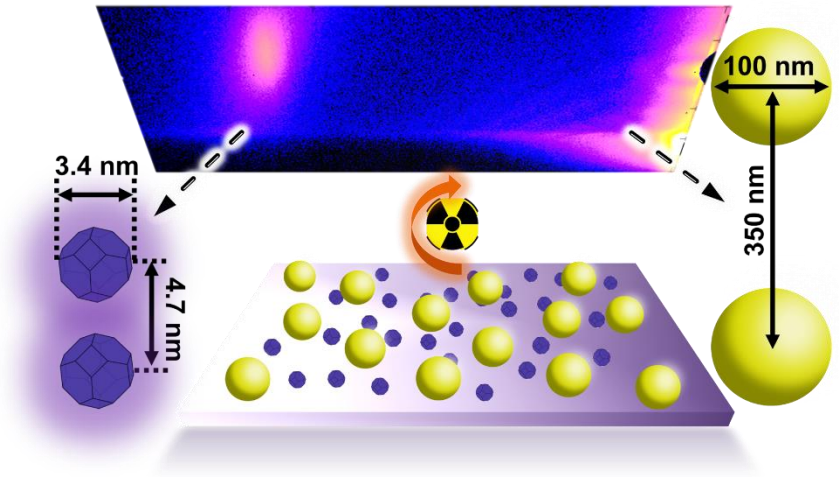

Hybrid plasmonic nanostructures have gained enormous attention in a variety of optoelectronic devices due to their surface plasmon resonance properties. Self-assembled hybrid metal/QD architectures offer a means of coupling the properties of plasmonics and QDs to photodetectors, thereby modifying their functionality. The arrangement and localization of hybrid nanostructures have an impact on exciton trapping and light harvesting. This chapter, presents a hybrid structure consisting of self-assembled Au NSs embedded in a solid matrix of PbS QDs for mapping the interface structures and the motion of charge carriers. Grazing-incidence small-angle X-ray scattering is utilized to analyze the localization and spacing of the Au NSs

within the hybrid structure. Furthermore, by correlating the morphology of the Au NSs in the hybrid structure with corresponding differences observed in the performance of photodetectors, the impact of interface charge carrier dynamics can determine in the coupling structure. From the perspective of architecture, this study provides insights into the performance improvement of optoelectronic devices.

7.1 Preface

The exploration of noble Au NPs has been widely studied in various optoelectronic devices [130-132]. The ability to independently tailor the sizes and inter-particle distances of the plasmonic arrangement enables a precise control of the optical and electrical properties, thereby enhancing the light-matter interaction resulting from LSPRs [133-136]. Of particular interest are integrated nanocomposites that combine photoactive materials with plasmonic metals to increase the overall properties of the hybrid films [137, 138]. The introduction of MNPs in photoactive materials results in the accumulation of incident photons around the particle, inducing both, near and far-field light scattering as well as electron transfer in the materials [139, 140]. Therefore, the light absorption and charge carrier efficiency as well as the local conductivity of the photoactive materials will improve and further enhance their optical and electrical performance [141, 142].

Recently, various optoelectronic materials including colloidal quantum dots (CQDs), organic polymers, and perovskite nanocrystals, have been studied in conjunction with plasmonic nanostructures to explore their high-performance capabilities [143-146]. The hybrid nanostructures offer numerous advantages such as high processability, spectral tunability, and compatibility through tuning the morphology and arrangement of the plasmonic NPs [147]. Moreover, the tunability of hybrid nanostructures guarantees an enhancement of the photonic and electronic properties of optoelectronic materials and improves the performance of the respective devices [148, 149]. Therefore, it is highly desirable to create hybrid systems that integrate photoactive materials with strong coupling plasmonic nanostructures for utilization in high-performance optoelectronic devices.

For the hybrid architectures in optoelectronic devices, the aggregation of NPs is an essential issue since it can hugely influence the film morphology and charge carrier efficiency [150, 151]. The self-assembly monolayer (SAM) coating of MNPs is a commonly used strategy for fabricating a large-area plasmonic organization and for preventing the aggregation of the MNPs [152]. With this approach, highly organized MNP arrays are expected to be feasible on larger scale. In addition, this approach facilitates the localized interaction between emitters and plasmonic cavities in the hybrid structures, which is notably helpful in improving the properties of the hybrid

systems [153].

It is widely acknowledged that the solution processing of CQDs holds various advantages for the development of optoelectronic devices [154, 155]. The surfactant organic linker molecules of CQDs influence the interdot distance and optical properties as well as the charge carrier transport in the CQD solids [156]. Thus, the arrangement of CQDs in the thin film is a significant issue for achieving high-efficiency optoelectronic devices. In addition, light management and electron transfer in such photo-sensitive devices extend from a single photoelectron level, necessitating a highly ordered photoactive structure [157, 158]. In this regard, the implementation of SAM plasmonic nanostructure hybrids with CQDs film can be an impressive way to enhance the performance of optoelectronic devices. Particularly, the investigation of interdot distances within CQDs solids influenced by the plasmonic nanostructures is a vital concern in controlling the film morphology and enabling large-scale application [159, 160].

Therefore, conducting an in-depth study of the hybrid plasmonic CQDs structure is essential for high-performance optoelectronic devices. GISAXS is a highly effective method to detect buried nanostructures and to probe film interfaces on a nanometer dimension [70]. Consequently, the distribution of CQDs and concealed localization of plasmonic structures in a hybrid nanostructure can be probed *via* GISAXS [161]. Recently, significant achievements have been made in the development of optoelectronic devices based on CQDs embedded with MNPs, owing to the ability of plasmonics to enable light-harvesting and enhance charge carrier transport [162-164]. However, these works are rarely focused on the construction of hybrid nanostructures and lack of an in-depth morphology investigation of the obtained architectures. It is critical to clarify the formation and composition of these nanostructures with more powerful characterization methods. Hence, a comprehensive investigation of the morphology and the impact of embedded MNPs on the hybrid system is urgently desired to fully explore their potential benefits.

To bring insights into complex hybrid structures, in this Chapter, a hybrid nanocomposite design is introduced where a PbS layer is deposited on a monolayer of Au NPs, created through self-assembly. This structure incorporates Au NPs with diameters of 20 nm and 100 nm, closely integrated with PbS CQDs to establish a direct interface between PbS and Au. GISAXS is use to examine the internal structure of the Au-PbS hybrid films and conduct a detailed analysis of their morphology. This study extends to evaluate the optical characteristics and charge carrier efficiency of the hybrid films, varying with the size of the Au NPs. By developing interdigital photodetectors using this hybrid approach can analyze how the plasmonic nanostructures influence device performance. In this contribution, I demonstrate a potential strategy to enhance the performance of photodetectors through the utilization of plasmonic nanostructures in PbS QDs.

7.2 Morphology of Au nanoarray and simulation

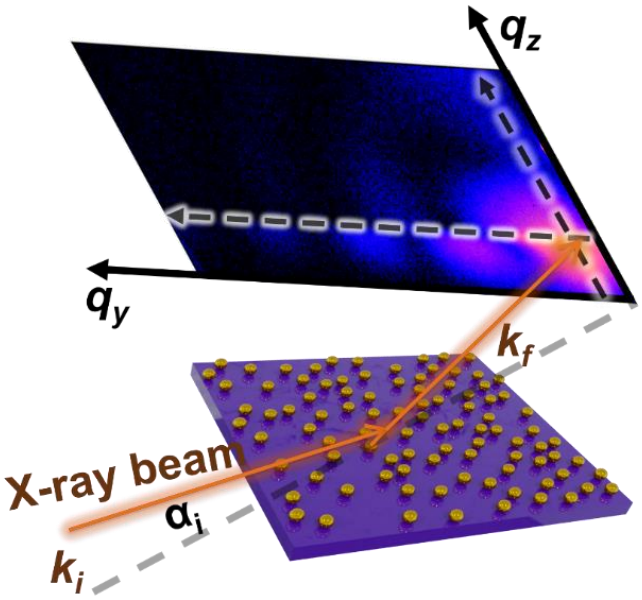

Figure 7.1. *Schematic geometry of the GISAXS setup utilized in this Chapter. Reproduced with permission from [28]. Copyright 2023 American Chemical Society.*

Controlling the morphology of plasmonic-based hybrid nanostructure requires a robust strategy for the in-depth understanding of the arrangement of the plasmonic structures [165]. Therefore, a combination of experimental and simulation techniques is needed to gain insights into the complex hybrid systems. In this regard, GISAXS is currently one of the most powerful techniques for studying plasmonic hybrid architectures, given that it furnishes statistically relevant information in the nano-range as well as enables the exploration of a large area and the inner morphology of the films [166, 167].

Moreover, the use of a synchrotron radiation source allows collecting high-quality data by the acquisition of exceptional signal-to-noise ratio measurements. This synergistic use of advanced experimental and simulation methods holds the promise of advancing our understanding and control of plasmonic-based hybrid nanostructures significantly. Figure 7.1 illustrates the schematic geometry of the GISAXS setup utilized in this study, enabling the analysis of both laterally (in the q_y direction) and vertically (in the q_z direction) structure of the samples.

In this study, Au NPs of two distinct sizes is fabricated, 20 nm and 100 nm, on Si substrates using a SAM technique. A thorough analysis of the spatial arrangement of the Au NSs are conducted. To enhance the plasmonic characteristics and investigate the possible uses of the Au NP monolayer, understanding its structural model is

crucial. This model encompasses the dimensions, form, and spatial distribution of the monolayer. To examine the configuration of the Au NS monolayer, a geometric model (illustrated in Figure 7.2) and conduct corresponding simulation using the BornAgain software are developed [74].

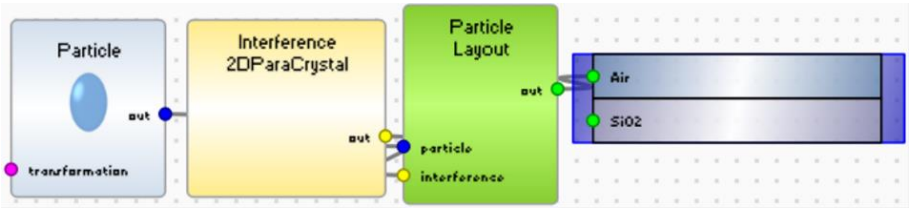

Figure 7.2. *Geometric model for simulations of the GISAXS data. Reproduced with permission from [28]. Copyright 2023 American Chemical Society.*

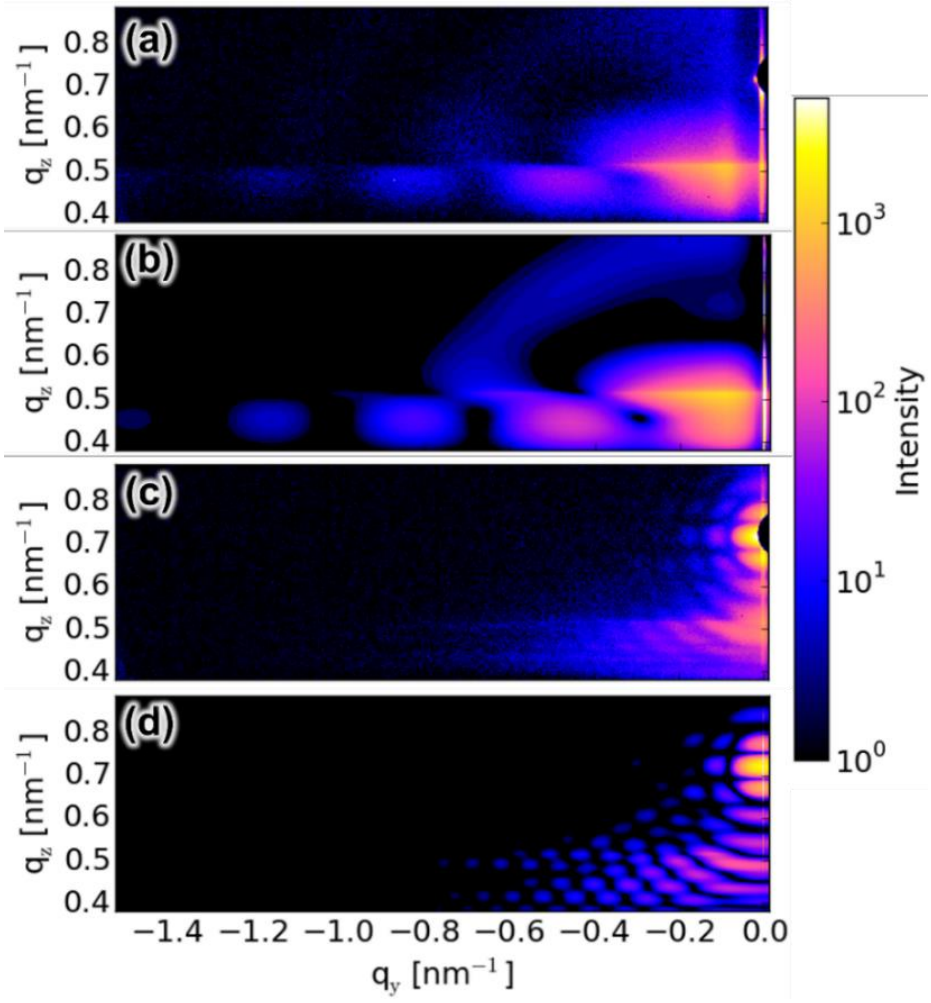

Figure 7.3. *2D GISAXS data of (a) 20 nm and (c) 100 nm Au NS monolayers and corresponding simulation results via BornAgain (b) and (d). Reproduced with permission from [28]. Copyright 2023 American Chemical Society.*

The GISAXS analysis of the Au NP monolayer (as shown in Figures 7.3a and c) reveals periodic Bragg scattering patterns for both the 20 nm and 100 nm Au NS samples. This observation exhibits not only exceptional size uniformity but also a well-ordered spatial arrangement over a large area. Additionally, the 2D GISAXS simulation results for our Au NS monolayer (depicted in Figures 7.3b and d) display a Bragg scattering pattern that aligns with the experimental data. The results confirm the high degree of structural order and uniformity in the Au NP monolayer, which are crucial for the plasmonic properties. This level of uniformity and order is essential for manipulating surface plasmon resonances, achieving consistent and reproducible plasmonic responses, and making it highly effective for potential applications.

To enhance the credibility of the simulation, line cuts (indicated by the black dashed line in Figure 7.1) from both the simulated and experimental GISAXS data are applied. The vertical line cuts off-center at q_y = 0.05 nm^{-1} and horizontal line cuts at the Yoneda peak are took, which corresponds to the peak of the Fresnel transmission function [168]. The 1D results (shown in Figure 7.4) demonstrate a strong correlation between the Bragg peak positions in the experimental and simulated data, validating the precision of our simulation model.

However, the discrepancies in intensity are attributed to the simplicity of the GISAXS model used for simulating the Au NS monolayers. These differences in intensity are relatively minor and can be overlooked, as they mainly reflect the quantity of scatterers and their arrangement. The consistency between the simulation and experimental results underscores the reliability of the modeling approach which facilities to the further analysis of the hybrid nanostructures.

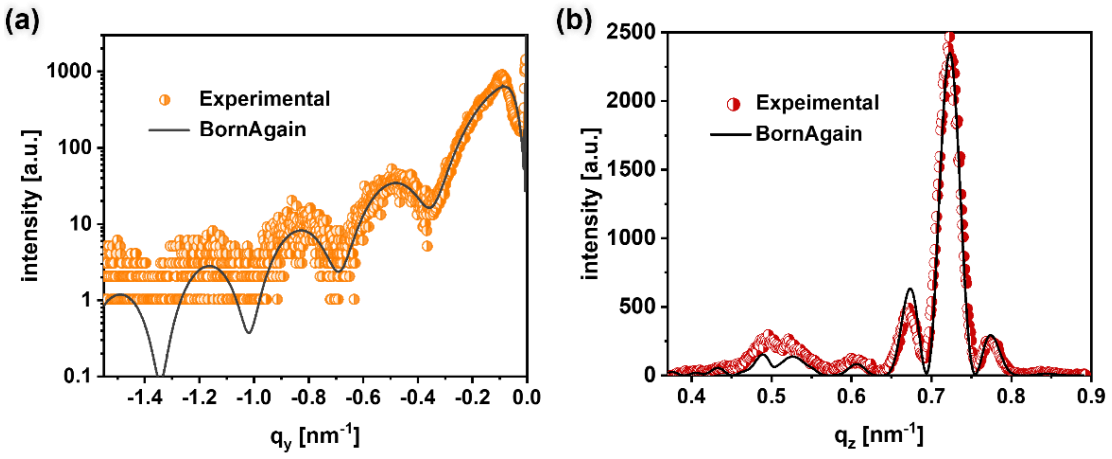

Figure 7.4. *GISAXS data (symbols) and BornAgain simulation results (lines) of line cuts of 2D GISAXS data from the (a) 20 nm and (b) 100 nm Au NS monolayer samples. The line cut position is performed as shown in Figure 7.1. Reproduced with permission from [28]. Copyright 2023 American Chemical Society.*

The real-space representation of our Au NP model (shown in Figure 7.5a) aligns well with the SEM images, providing further confirmation of the validity of our simulation. Additionally, the BornAgain modeling framework allows us to determine the domain sizes and center-to-center spacings of the Au NPs (illustrated in Figure 7.5b).

The simulation results for the GISAXS analysis indicate that the smaller Au NPs have a diameter of (20.4 ± 0.2) nm with an interparticle gap of (71.0 ± 0.5) nm. In contrast, the larger NSs have a diameter of (100.0 ± 0.5) nm with a (350.0 ± 1) nm interparticle distance. These findings are in line with the statistical analysis derived from the SEM image frequency distributions (Figure 7.6).

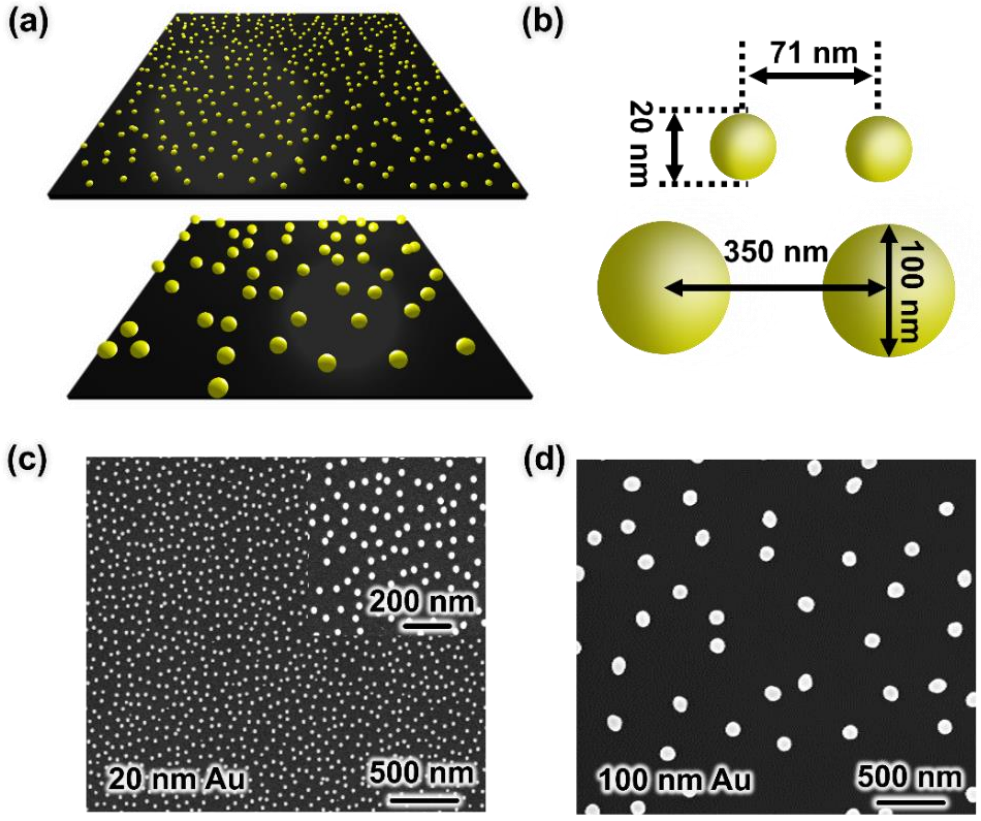

Figure 7.5. *(a, b) Visualization of 20 nm and 100 nm Au NSs modeling set up. SEM images of (c) 20 nm and (d) 100 nm Au monolayers. Reproduced with permission from [28]. Copyright 2023 American Chemical Society.*

Through systematic analysis, the dimensions and interparticle distances of the Au NP monolayers are verified. The successful application of the SAM method highlights its potential in creating extensive high-order plasmonic nanostructures. Such structures are advantageous for optimizing optical and electrical characteristics by adjusting their sizes and spatial arrangements [169].

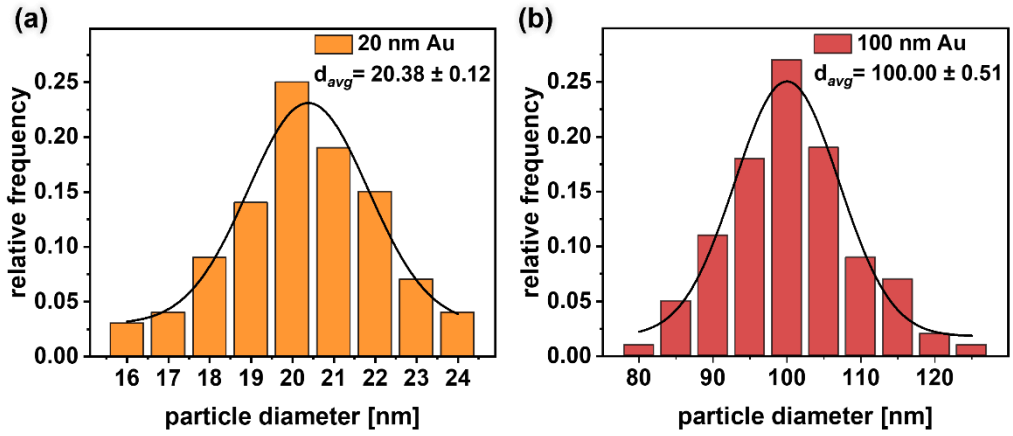

Figure 7.6. *Statistical frequency distribution and average size of (a) 20 nm and (b) 100 nm Au NSs as extracted from the SEM images via ImageJ. Reproduced with permission from [28]. Copyright 2023 American Chemical Society.*

7.3 Surface morphology of Au/PbS hybrid structures

Integrating plasmonic nanostructures with photoactive materials creates a versatile platform that can be precisely tuned for improved performance. In this study, a hybrid system by combining the Au NP monolayer with PbS quantum dots is developed. This configuration aims to explore the potential of such a system in optoelectronic device applications, leveraging the unique properties of both components to enhance device functionality.

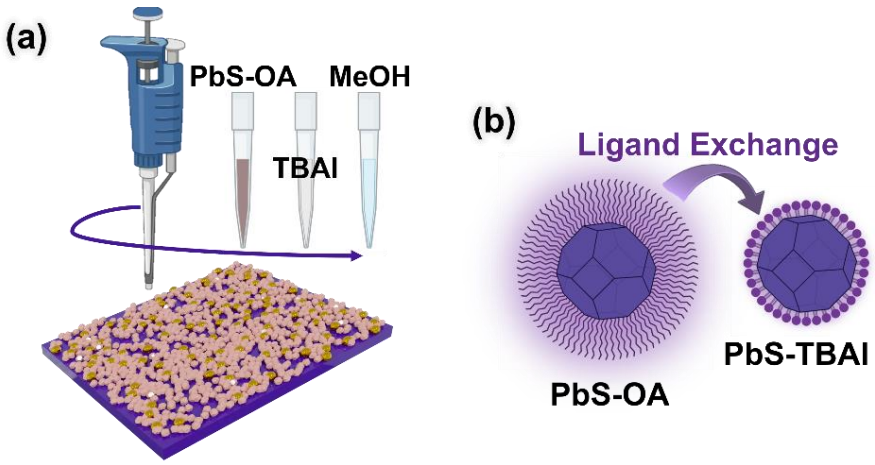

Figure 7.7. *(a) Schematic diagram of Au NSs/PbS hybrid nanostructure fabrication process. (b) Schematic of ligand replacement of PbS QDs from long ligand OA to shorter TBAI ligands. Reproduced with permission from [28]. Copyright 2023 American Chemical Society.*

Figure 7.7a presents a diagram outlining the creation of the hybrid system. The process begins by spin-coating a PbS-OA solution onto the Au NS monolayer to form Au/PbS OA films. Next, the QD surface ligands are switched from OA to TBAI by treating the PbS-OA film with a TBAI solution. This is followed by a layer-by-layer deposition process, repeated three times, to produce the PbS-TBAI solid layers. Figure 7.7b depicts the substitution of the QDs long OA ligands with shorter TBAI ionic ligands. This modification aims to reduce the distance between the quantum dots, enhancing their stability and electronic interaction, which in turn facilitates more efficient charge carrier transport [170].

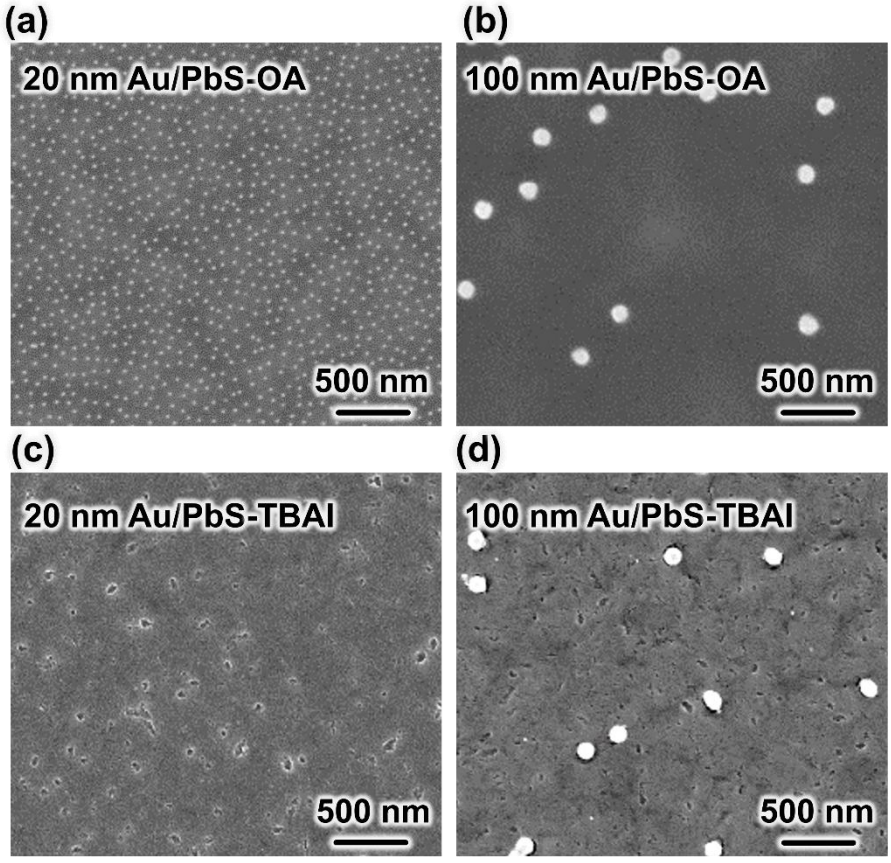

Figure 7.8. *SEM images of (a) 20 nm Au/PbS-OA film and (b) 100 nm Au /PbS-OA hybrid film; (c) 20 nm Au/PbS-TBAI film and (d) 100 nm Au /PbS-TBAI hybrid film. Reproduced with permission from [28]. Copyright 2023 American Chemical Society.*

The structural characteristics of the hybrid films are examined using SEM, as depicted in Figure 7.8. When comparing these films with the initial Au NP monolayers (shown in Figure 7.5), it is evident that the PbS QDs are uniformly coated over the Au NPs, forming integrated hybrid components. Importantly, the arrangement of the 20 nm and 100 nm Au NSs remains unchanged after the PbS OA QDs application (seen in Figures 7.8a and b), signifying the stability of Au NP monolayer. Following the TBAI

treatment, the PbS-OA films transition to a densely packed structure, as shown in Figures 7.8c and d. Specifically, the 20 nm Au/PbS TBAI film (Figure 7.8c) demonstrates that the QD layer completely covers the Au NSs, with the PbS-TBAI film thickness exceeding 20 nm due to successive coatings. In contrast, the 100 nm Au/PbS-TBAI structure illustrates QDs closely packed around the Au NSs, which remain visible at the sphere tops.

7.4 Inner morphology of Au/PbS hybrid structures

The LSPR characteristics of the Au NPs are influenced by their size, distribution, and the dielectric environment, our configurations offer a unique platform to assess how these parameters affect the properties of Au/PbS QDs hybrid system. This also allows for the investigation of the impact of 20 nm and 100 nm Au NPs on the morphology of PbS QDs film. While SEM images provide insights into the Au NPs configuration, their resolution limits the detailed analysis of QDs smaller than 5 nm in diameter. Furthermore, understanding the internal structure and interfacial interactions within the hybrid system is crucial, prompting an in-depth examination using GISAXS. This technique is used to scrutinize the behavior of both 20 nm and 100 nm Au NSs within the PbS QDs layered architecture, offering a more comprehensive understanding of the intricacies of hybrid structure.

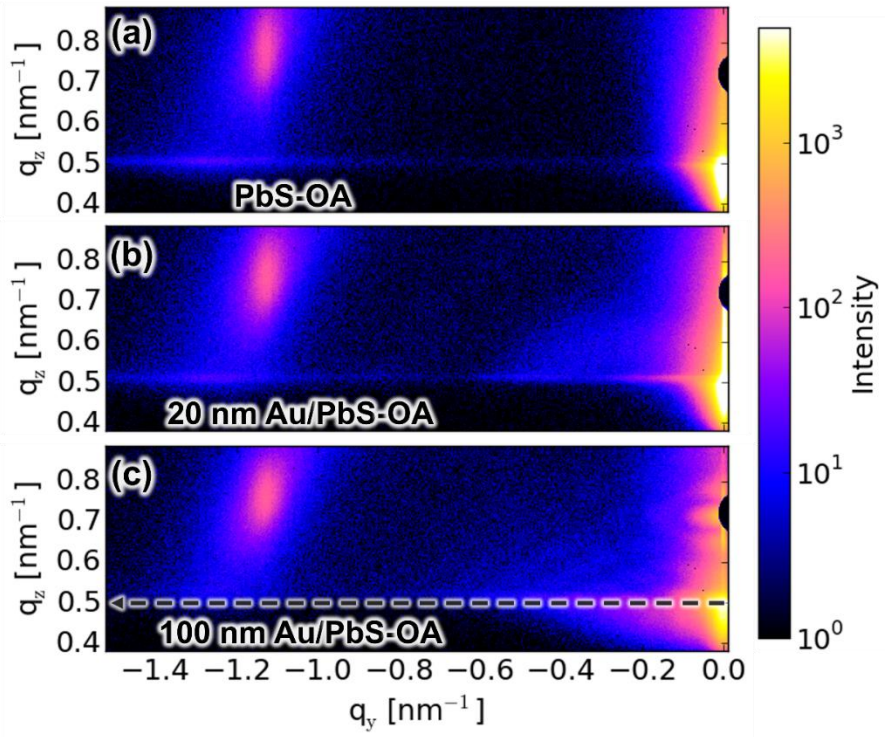

Figure 7.9. *2D GISAXS data of the samples based on (a-c) PbS-OA QDs. Reproduced with permission from [28]. Copyright 2023 American Chemical Society.*

Figure 7.9 presents the 2D GISAXS data for both bare PbS films and their corresponding Au/PbS hybrid counterparts, offering insights into their structure characteristics. The scattering pattern of PbS-OA film demonstrates a clear structural signal at a higher q_y value (around 1.30 nm^{-1}) near the Yoneda peak (around 0.50 nm^{-1}, indicative of the PbS-OA QDs structural factors. This specific signal is also observable in the Au/PbS-OA hybrid films (seen in Figures 7.9b and c), indicating that the inclusion of Au NPs does not significantly alter the QDs structure. The Au NSs is still detectable at a lower q_y value (around -0.40 nm^{-1} after the PbS OA film application, consistent with the SEM findings (Figures 7.8a and b) and confirming their integrity post-deposition.

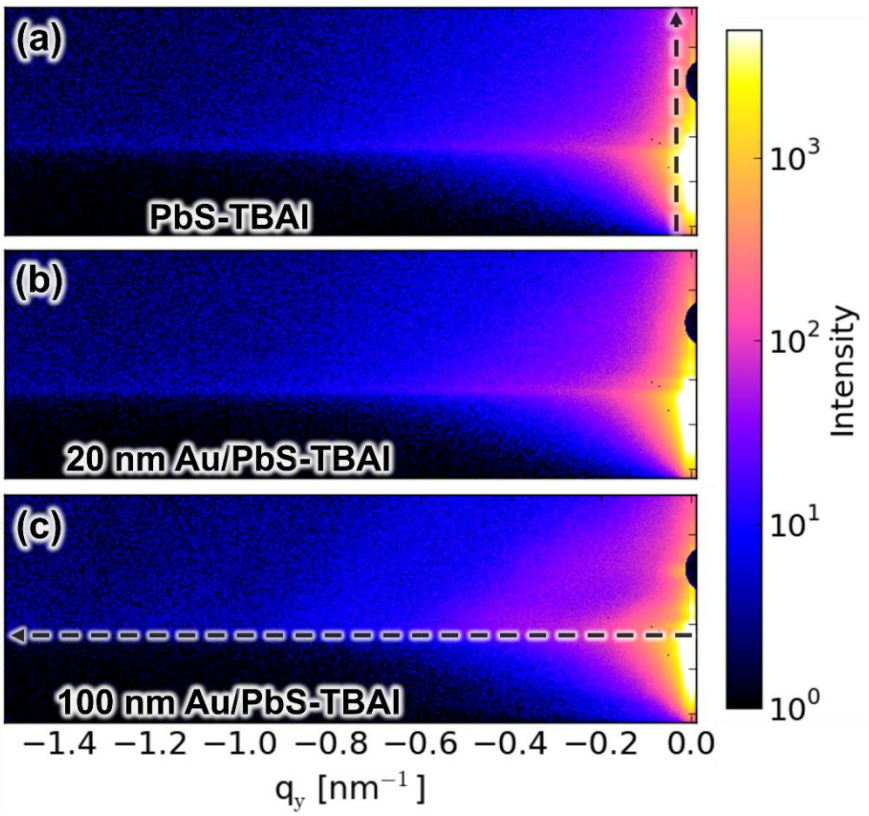

Figure 7.10. *2D GISAXS data of the samples based on (a-c) PbS-TBAI QDs. Reproduced with permission from [28]. Copyright 2023 American Chemical Society.*

After ligand exchange (shown in Figures 7.10a-c), it is noteworthy that the Yoneda peak for the PbS-TBAI film shifts to a higher q_z value (around 0.57 nm^{-1}, while the high q_y value structural signals vanish, indicating a transition to a more densely packed structure in the PbS-TBAI QDs, as inferred from the increased scattering length density. Moreover, the structural data for only the 100 nm Au NSs remains discernible at a lower q_y value (around -0.40 nm^{-1}, with the 20 nm Au NSs being completely masked by the PbS QDs. To further dissect the hybrid nanostructures,

horizontal (at the *Yoneda* peak) and vertical line cuts (around -0.05 nm^{-1} at the structural signal location are used in the GISAXS data analysis (indicated by a black dashed line), enhancing the detailed examination of our devised architectures.

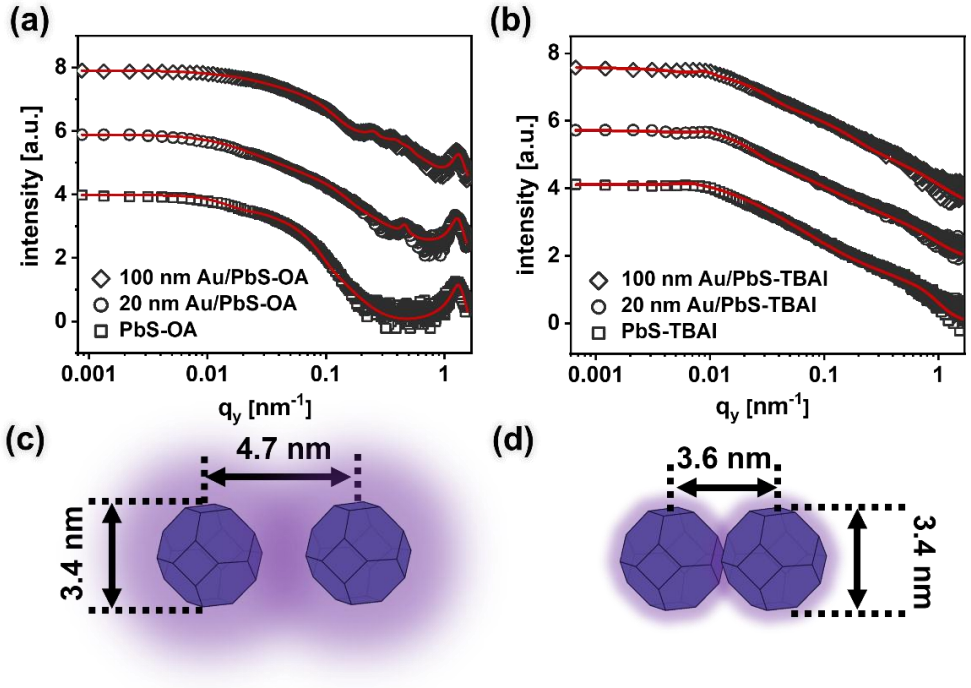

Figure 7.11. *Horizontal line cuts of 2D GISAXS data (black dots) and corresponding modelling (redline) of samples based on (a) PbS-OA QDs and (b) PbS-TBAI QDs. Schematic (c) and (d) of the arrangement of PbS QDs. Reproduced with permission from [28]. Copyright 2023 American Chemical Society.*

Figures 7.11a and b showcase the horizontal line cuts (represented by black dots) alongside the fitted modeling outcomes using a spherical model (depicted by the red line) for our films. A sphere-based model is applied to analyze the GISAXS line cuts quantitatively, deriving a QD radius of approximately (3.4 ± 0.1) nm, as illustrated in Figures 7.11c and d. Furthermore, I calculated the interdot spacing for the PbS-OA QDs to be (4.7 ± 0.1) nm, which reduces to (3.6 ± 0.1) nm following the TBAI-mediated ligand swap. The precise measurement of the q_y parameters sheds light on the lateral structural characteristics of the PbS QDs when subjected to different ligands. Importantly, these lateral structural arrangement of the QDs minimally affected by the presence of either 20 nm or 100 nm Au NSs. I further delve into the vertical structural analysis of the hybrid films, as illustrated in Figure 7.12. The most intense sharp peaks correspond to the Yoneda peak of the films. For the PbS-OA QDs (indicated by gray dots in Figure 7.12a), a notable shift in the critical angle from 0.12° to 0.17° is observed post the TBAI ligand substitution (shown by gray dots in

Figure 7.12b). This alteration is likely due to the more compact arrangement of PbS QDs with a reduced average interdot distance, creating a denser film and altering the SLD of the QD film. Consequently, this results in the higher angular positioning of the *Yoneda* peak. Furthermore, while the Yoneda peak for the Au/PbS-OA films shifts to a higher angle, the Au/PbS-TBAI films peaks do not exhibit any significant change. These findings imply that Au NSs significantly impact the vertical structure of the PbS-OA films, whereas their effect on the densely packed PbS-TBAI structure appears to be minimal [171].

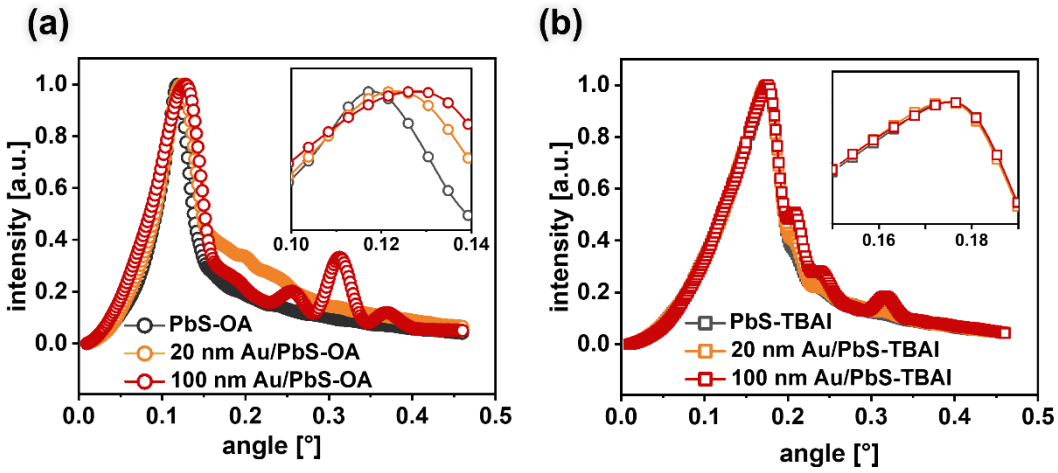

Figure 7.12. *Vertical line cuts of GISAXS data of samples based on PbS-OA (a) QDs and (b) PbS-TBAI QDs. The insets show a zoom-in to the Yoneda peaks. Reproduced with permission from [28]. Copyright 2023 American Chemical Society.*

The structural analysis of our hybrid films indicates that the incorporation of Au NPs does not significantly alter the lateral structure of the PbS-OA QDs or the overall arrangement of the PbS-TBAI film, both laterally and vertically. Nonetheless, the plasmonic nanostructures influence the vertical structure of PbS QDs with longer ligands. The observed changes in the morphology of PbS-OA film can be attributed to the instability of the longer ligands surrounding the PbS QDs, making them susceptible to alterations when combined with other nanostructures. In contrast, PbS QDs with shorter ligands exhibit a more compact and stable structure, maintaining their stability upon integration. These findings highlight the importance of understanding the impact of plasmonic nanostructures on the structural properties of hybrid PbS films, which is essential for the development of scalable monolayer or multilayer hybrid architectures. To enhance the utility of these hybrid PbS films further, it is crucial to investigate how Au NSs influence their optical and electrical characteristics. Such properties will provide valuable insights into optimizing the performance of these materials for their potential applications.

7.5 Optical properties

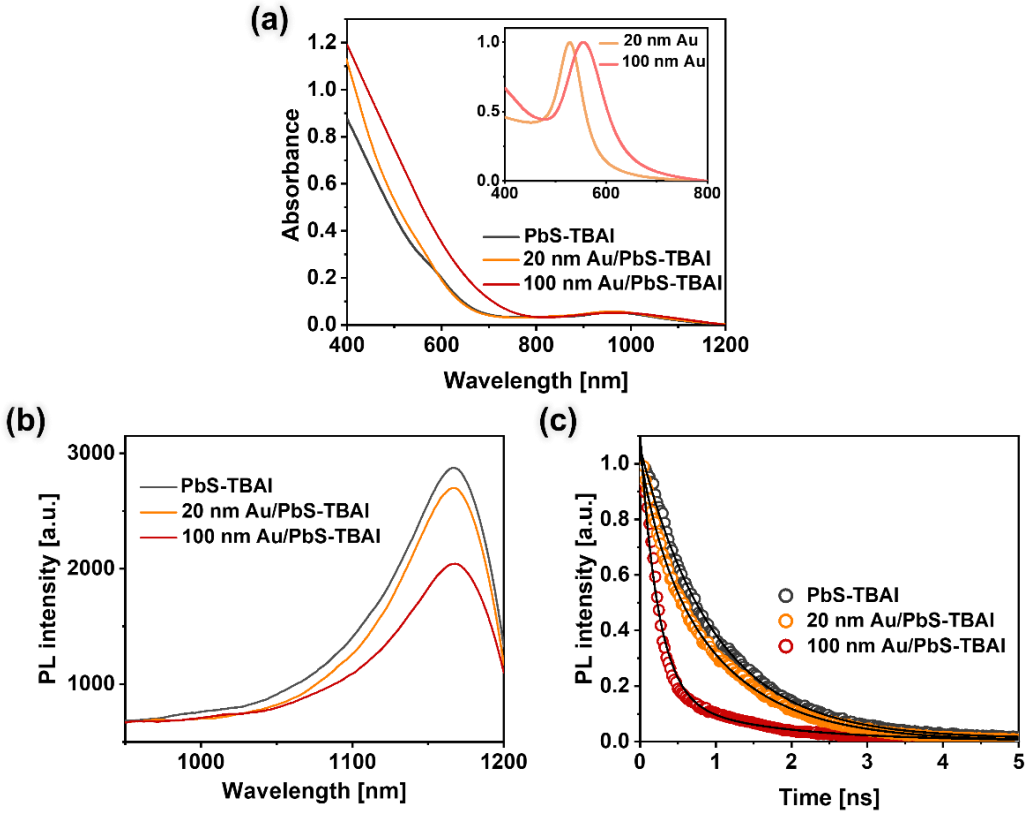

Figure 7.13. *(a) Absorbance of bare PbS-TBAI film and Au NPs/PbS-TBAI films and the insert image is the absorbance of Au NSs in solution. (b) PL and (c) TRPL emission spectra of bare PbS-TBAI film and Au NSs/PbS-TBAI films. Reproduced with permission from [28]. Copyright 2023 American Chemical Society.*

To investigate the optical characteristics of our hybrid structures, both the absorbance and PL spectra in the Vis-NIR range are analyzed. Figure 7.13a displays the normalized absorbance spectra for the films and Au NP solutions. An observation from the inset image reveals a red shift in the absorbance peaks of the Au NPs from 520 nm to 580 nm with an increase in particle size, aligning with previous findings [172]. The films maintain a consistent absorption edge around 950 nm and exhibit marked absorbance enhancement in the spectral range corresponding to the Au NPs. This enhancement in the Au/PbS hybrid films absorbance is likely due to the spectral overlap of the components, enhancing the films optical attributes [173].

The steady-state and time-resolved PL (TRPL) analyses are conducted to delve into the photoinduced charge carrier dynamics in the films. The incorporation of 100 nm

Au NPs diminishes the PbS emission, as shown in Figure 7.13b, signifying boosted charge carrier extraction and reduced recombination. TRPL decay data for pure PbS and Au/PbS hybrid films are depicted in Figure 7.13c, with associated decay kinetics detailed in Table 7.1. Consistent with the PL data, the 100 nm Au/PbS film demonstrates the shortest PL decay time, indicating enhanced charge carrier transport due to the Au NPs. The PL and TRPL results suggest that Au NSs, especially the 100 nm size, significantly improve the charge extraction efficiency of the PbS film. Considering the morphology, the PbS film thickness ranges between 20 nm and 100 nm for all photodetector samples, implying that 100 nm Au NPs exert a greater impact on charge carrier efficiency across the entire thickness of PbS film than 20 nm Au NPs. Consequently, the 100 nm Au NPs/PbS hybrid film exhibits superior optical characteristics and enhanced charge carrier efficiency.

Table 7.1. *TRPL fast and slower decay kinetics parameters.*

Sample	PbS-TBAI	20 nm Au /PbS-TBAI	100 nm Au /PbS-TBAI
τ_1 (ns)	0.97	0.27	0.23
τ_2 (ns)	6.99	1.02	1.45
A_1 (%)	99.61	21.36	85.58
A_2 (%)	0.39	78.64	14.41
τ_{avg} (ns)	1.16	0.98	0.85

7.6 Electrical properties

As previously discussed, the prepared hybrid structure has the potential to enhance optical performance. Consequently, it is essential to further validate the performance of this structure. A photodetector, which is a common light-responsive semiconductor device, will be used for this purpose. Subsequently, to explore their applications in optoelectronic devices, an Au/PbS hybrid film is constructed specifically designed for photodetectors.

The design of this photodetector is depicted in Figure 7.14a. The process involves initially positioning both 20 nm and 100 nm Au NPs on the channel of the IDE chip, followed by the deposition of PbS QDs using a TBAI ligand exchange treatment on the Au Np monolayer. The SEM images in Figure 7.14b and c display the 20 nm Au NPs arranged on the IDE substrate and the subsequent coverage with PbS-TBAI QDs, respectively.

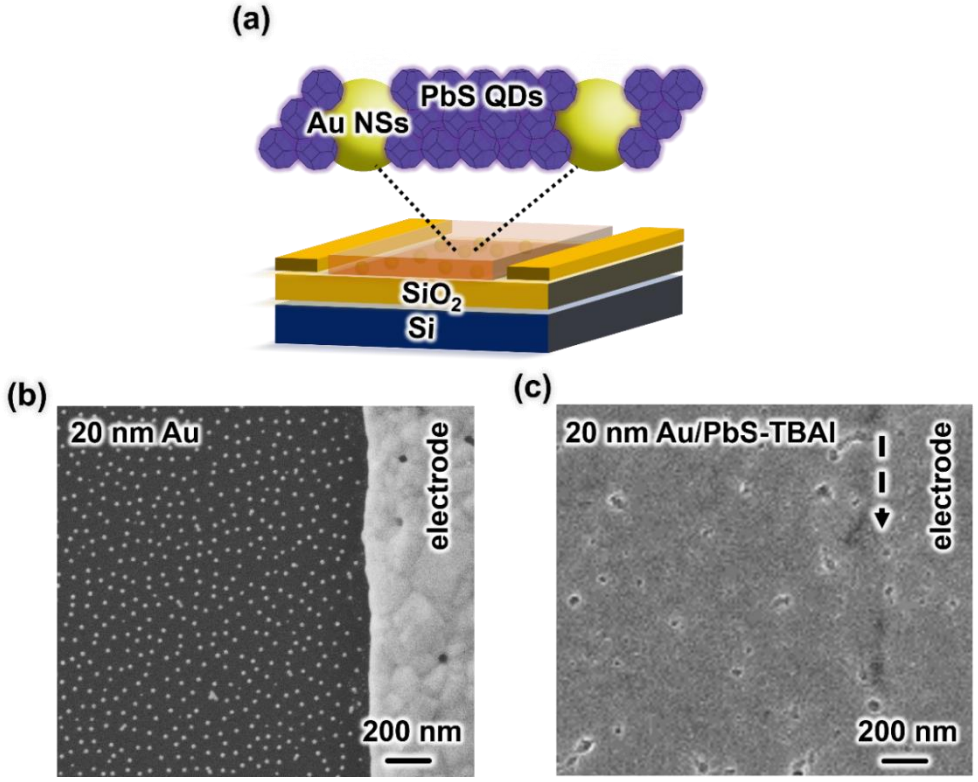

Figure 7.14. *(a) Schematic illustration of Au NSs/PbS based photodetector configuration. Golden sphere represents Au NSs, and purple polyhedron represents PbS QDs. SEM images of (b) 20 nm Au NP monolayer and (c) 20 nm Au/PbS-TBAI hybrid film on IDE substrate. Reproduced with permission from [28]. Copyright 2023 American Chemical Society.*

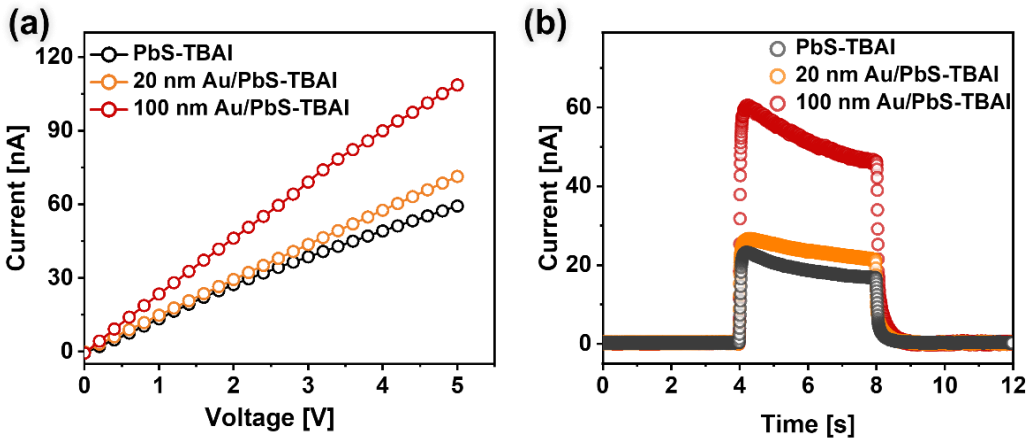

Figure 7.15. *Illuminated (a) currents and (b) on-off signal of PbS-TBAI, 20 nm Au/PbS-TBAI, and 100 nm Au/PbS-TBAI devices. On-off signals derived from the devices with the illumination wavelength of 960 nm, the intensity of 420.8 mW cm^{-2} and the applied voltage of 5 V. Reproduced with permission from [28]. Copyright 2023 American Chemical Society.*

Following this, the photodetector devices is evaluated to assess the electrical characteristics of our setup, as illustrated in Figure 7.15. The current-voltage (I-V) characteristics, shown in Figure 7.15a, reveal that devices incorporating plasmonics exhibit a higher photocurrent compared to the device with only PbS, likely due to enhanced charge carrier mobility and light absorption in the PbS film [174]. Notably, the device incorporating 100 nm Au NPs displays the most significant photocurrent, aligning with the exceptional optical attributes of this hybrid film.

Then the detection consistency of the devices is assessed using light on-off cycles, shown in Figure 7.15b. In alignment with the I-V findings, the photocurrent for the device with 100 nm Au NPs outperforms the 20 nm Au/PbS and the bare PbS devices, indicative of the superior charge carrier transport facilitated by the 100 nm Au NPs. Furthermore, the rise time for the devices with plasmonic elements indicates quicker response time to light exposure, suggesting that the plasmonic configuration enhances the device sensitivity to light. Moreover, the rise time of the plasmonic-based devices shows a faster photo-rise time (Table 7.2), depicting that the plasmonic structure makes the device more sensitive to photo-illumination.

Table 7.2. *Photo-response on-off characteristics of the devices.*

Sample	PbS-TBAI	20 nm Au /PbS-TBAI	100 nm Au /PbS-TBAI
T_{rise}	21.85	17.82	12.90
T_{fall}	27.27	28.79	27.19

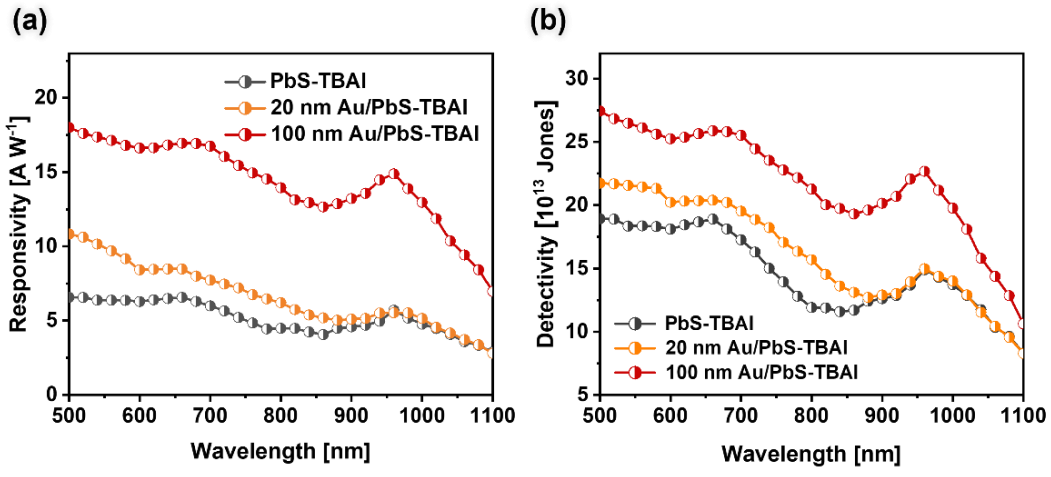

Figure 7.16. *(a) Responsivity and (b) detectivity of the photodetector devices being illuminated under 323.3 μW cm^{-2} with an applied voltage of 5 V. Reproduced with permission from [28]. Copyright 2023 American Chemical Society.*

To assess the light response performance of the photodetectors, their responsivity and detectivity spectra across different wavelengths are analyzed, as shown in Figure 7.16. All devices exhibit wavelength-dependent responses that align with the absorption characteristics of PbS QDs, typically centered around 950 nm. However, the 100 nm Au/PbS device demonstrates notably higher intensity values across the entire spectrum tested, indicating superior light-absorption efficiency compared to the other devices.

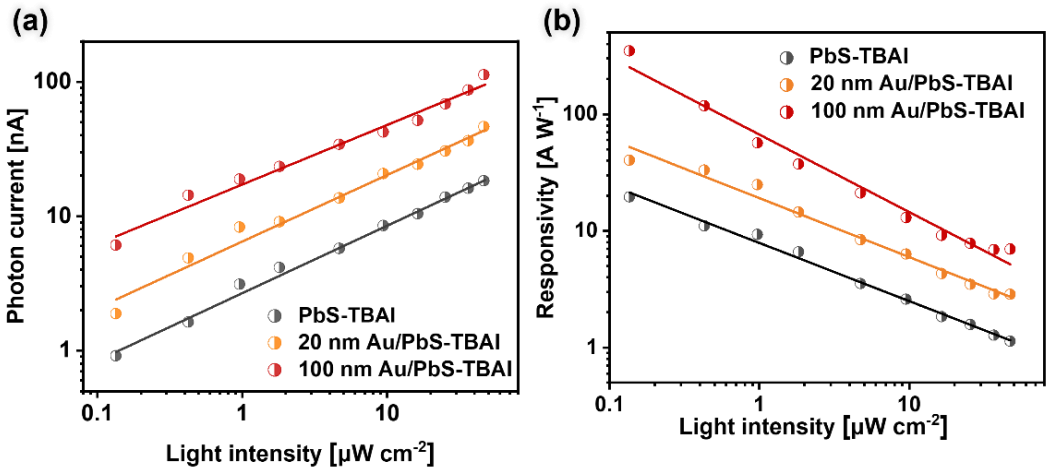

Figure 7.17. *(a) Current and (b) responsivity evolutions of the devices with increasing of the illumination light intensity from 63.5 μW cm^{-2} to 6.3 mW cm^{-2} with the illumination wavelength of 960 nm. Reproduced with permission from [28]. Copyright 2023 American Chemical Society.*

The varying light intensities effects on the performance of the devices are investigated by analyzing photocurrent and responsivity under illumination power densities ranging from 63.5 μW cm^{-2} to 6.3 mW cm^{-2}, as depicted in Figure 7.17. As the power density of the light increases, the responsivity of the devices tends to decrease, which due to the saturation of photogenerated charge carriers [175]. Remarkably, under identical device configurations and test conditions, the 100 nm Au/PbS device demonstrates the highest photocurrent and responsivity, surpassing the performance of both the bare PbS and the 20 nm Au/PbS devices.

7.7 Mechanism of plasmonic enhancement in hybrid system

The enhancement in the performance of the photodetectors under light exposure is largely due to the LSPRs stimulated by the incorporation of plasmonic Au NPs in the hybrid structure. Particularly, when the frequency of the incident light aligns with that of the Au NPs within the hybrid film, a congregation of "hot electrons" forms

oscillating electron clouds on the surface of Au NPs, as shown in Figure 7.18. These energized hot electrons, acquiring enough energy from the external bias, overcome the Schottky barrier at the Au NPs/PbS interface and move into the conduction band of PbS [176]. Consequently, this electron transfer boosts the charge density and photoresponsivity in the PbS film, thereby enhancing the devices overall performance.

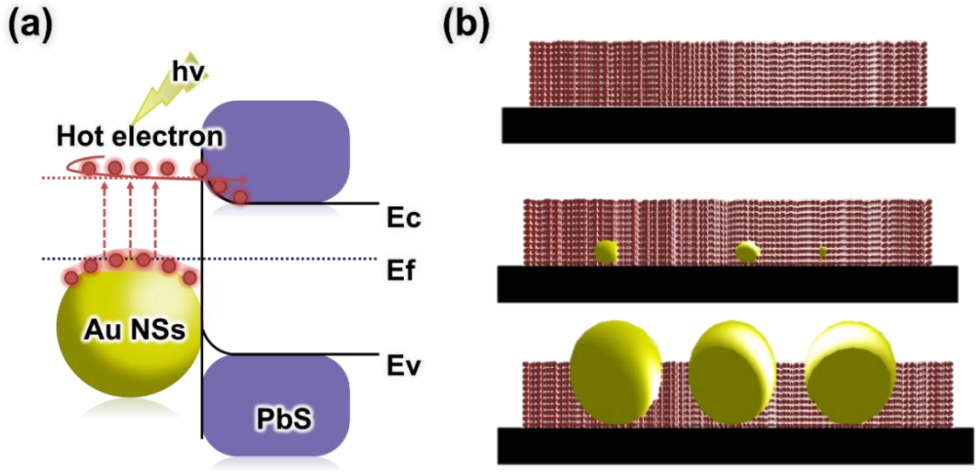

Figure 7.18. *(a) Schematics of the energy band diagram of the Au/PbS photodetectors under light illumination. (b) Structure configuration of the hybrid systems. Reproduced with permission from [28]. Copyright 2023 American Chemical Society.*

7.8 Summary

In conclusion, this work developed a hybrid structure by depositing PbS QDs onto a self-assembled monolayer of Au NPs and thoroughly examined both the structural formation of the hybrid nanostructures and their use in photodetectors. By utilized the BornAgain software to analyze the GISAXS data of the Au NP monolayers, determining the sizes and interparticle distances of these plasmonic layers. The integration of 20 nm and 100 nm Au NPs with PbS QDs revealed minimal impact on the lateral structure of PbS-OA QDs and the lateral and vertical configurations of PbS-TBAI film. Nonetheless, these nanoparticles influence the vertical alignment of PbS-OA QDs. Such morphological insights are crucial for advancing the development of large-scale, monolayered, or multilayered hybrid films. Optical assessments using PL and TRPL show that the plasmonic nanostructures enhance the optical attributes of the PbS film, with the 100 nm Au NPs/PbS film exhibiting superior optical properties. When integrating this hybrid system into interdigital photodetector devices, an enhancement in photocurrent for the plasmonic devices compared to the plain PbS device, as evidenced by the I-V curve and light on-off experiments. Moreover, the devices incorporating the Au NP monolayer displayed improved responsivity and

detectivity. Particularly, the photodetector with 100 nm Au NPs showcased the most impressive performance, aligning with the optical characterization results. Our research indicates that the enhanced optical and electrical properties of the hybrid film are likely due to increased charge carrier efficiency, with the effective inclusion of 100 nm Au NPs enhancing performance throughout the PbS film. Thus, our study on the precise control of spacing in the Au-PbS system offers valuable insights for the design of hybrid systems and presents a promising approach for optoelectronic device development.

8 Conclusion and outlook

Strongly enhanced light-matter interactions induced by LSPR originate from the electromagnetic fields excited at the junctions between metallic nanostructures. One effective strategy for optimizing the plasmonic properties of these nanostructures is the fabrication of hybrid nanostructures. Hybrid nanostructures offer numerous advantages, such as high processability, spectral tunability, and compatibility, by tuning the morphology and arrangement of plasmonic NPs. By constructing BMN composites with two distinct metals, one can leverage the advantages of both metals. Additionally, integrating metallic nanostructures with optoelectronic semiconductor materials enhances both electrical and optical performance. Therefore, creating a hybrid system with strongly coupled plasmonic nanostructures is highly desirable for various applications. However, in hybrid architectures, the aggregation of NPs is a critical issue since it can significantly influence film morphology and charge carrier efficiency.

A commonly used strategy to address this issue is the self-assembly monolayer method, which facilitates the fabrication of large-area plasmonic arrays and prevents the aggregation of MNPs. This approach is expected to realize highly ordered metal nano-arrays over large areas. This thesis first investigates two distinct self-assembly methods for fabricating Au nanoarrays: electrostatic adsorption and phase interface transfer. Compared to the phase interface transfer method, the electrostatic assembly method resulted in NPs being evenly distributed across the substrate with minimal aggregation, demonstrating a uniform particle arrangement. This highly ordered arrangement is crucial for the application of self-assembled Au nanoarrays in plasmonic structures. Uniform plasmonic resonance can generate periodic hot carriers, thereby enhancing the plasmonic properties of the structure. Therefore, the electrostatic adsorption method is selected as the preferred self-assembly technique for subsequent projects.

To fully maximize the functionality and application potential of hybrid nanostructures, it is crucial to conduct an in-depth study of their arrangement and inner morphology. Therefore, a high-resolution technique is urgently needed to thoroughly analyze the hybrid systems. GIXS is an ideal technology for examining nanostructures at the nanoscale. Its high temporal resolution and robust penetration detection capabilities

make it a widely favored method for *in situ* experiments. GIXS can be used to investigate the dimensions, spatial distribution, and crystalline characteristics of hybrid plasmonic structures. Consequently, it is feasible to use GIXS to monitor hybrid plasmonic nanostructures based on self-assembled Au nanoarrays, enabling a detailed investigation into the crystallization and evolution of these hybrid nanostructures.

The first study proposes a hybrid Au/Ag nanostructure achieved by sputter depositing Ag metal onto Au NP substrates under low-temperature dewetting conditions, while concurrently monitoring the process with *in situ* GISAXS/GIWAXS. Specifically, Ag NPs are deposited using HIPIMS on 10 nm and 20 nm Au NP templates, both with and without thermal annealing at 100°C. To elucidate the structural configuration of the hybrid Au/Ag composite, the bimetallic nanostructures are tailored using GISAXS/GIWAXS and meticulously examine the morphology and crystalline characteristics of the nanostructures. The study demonstrates that the Au/Ag composite exhibits an increased structural organization and enhanced crystalline properties when subjected to dewetting treatment. Additionally, the development of Au/Ag nanostructures are accurately trace by examining their size and distribution through our analytical approach. For SERS applications, the deposition to achieve appropriately sized gaps are optimized, selecting an optimal deposition stage. The SERS results reveal that the 20 nm Au template with dewetting treatment exhibits the highest sensitivity in detecting R6G molecules. This study illustrates a promising approach for producing hybrid binary or multi-component metallic nanostructures while precisely monitoring their dimensions and interparticle spacing. The findings represent a potential advancement in creating SERS platforms, color display technologies, catalysts, and other applications rooted in plasmonics.

Further work introduces a hybrid nanocomposite architecture by depositing a PbS layer onto a highly ordered array of Au NSs fabricated via a self-assembly method. Specifically, 20 nm and 100 nm Au NSs are assembled and coupled them with PbS CQDs using OA and TBAI ligands, achieving direct interfacing between PbS and Au. To understand the behavior of Au NSs in PbS films, the hybrid films are probed using GISAXS and systematically investigated the inner morphology of hybrid Au-PbS nanostructures at the nanometer level. Our findings indicate that the size of the Au NSs has weak impact on the lateral structure of the PbS-OA film but indeed affect the vertical structure. Conversely, the Au NPs do not influence either the lateral or vertical arrangement of the PbS-TBAI film. Additionally, the hybrid film exhibits enhanced optical properties, with the 100 nm Au/PbS hybrid film showing superior optical properties and a significant positive impact on charge carrier efficiency. By fabricating interdigital photodetectors, the behavior of plasmonic nanostructures are examined in device performance. Characterization results of the devices revealed that the incorporation of Au NPs improves the photocurrent and photoresponsivity of the

photodetectors, consistent with the enhanced optical properties observed. This study demonstrated a potential strategy to enhance photodetector performance through the utilization of plasmonic nanostructures in PbS QDs. The exploration of spacer control in plasmonic-photoactive materials architecture provides a promising guideline for constructing such hybrid systems. This finding will significantly influence the development of optoelectronic devices.

Overall, in this thesis, Au/PbS and Au/Ag hybrid nanostructures are fabricated based on self-assembled Au nanoarrays. Using advanced scattering techniques, the hybrid nanostructures are thoroughly characterized, by analyzing their morphology and correlating these findings with their optical and electrical properties. Then the application of these fabricated hybrid nanostructures is investigated in photodetectors and SERS. The results demonstrate the potential applications of fabrication and analysis methods in the field of plasmonics and contribute to the advancement of analysis techniques within this field.

Since the present thesis focused on spherical Au NPs and examined their properties and applications. For future work, I intend to explore Au NPs of various shapes, such as nanorods and nanocubes, and to characterize their structural properties using scattering techniques. Additionally, I plan to employ alternative self-assembly methods, such as the template method, to construct different types of plasmonic arrays. Furthermore, presented results opens opportunities to explore other hybrid plasmonic systems using various metals and semiconductor materials. For instance, fabricating bimetallic nanostructures based on Au nanoarray with metals like Pt, Cu, and Al could be investigated for their applications in SERS, catalysis, imaging, and photonics. Additionally, incorporating plasmonic metals with other semiconductor materials, such as polymers, perovskites, and 2D materials, can expand their applications in various optoelectronic devices, including photovoltaics, transistors, and LEDs.

Bibliography

[1] Lal, S.; Link, S.; Halas, N. J. Nano-Optics from Sensing to Waveguiding. *Nat. Photonics* **2007**, 1, 641-648.

[2] Cortie, M. B.; McDonagh, A. M. Synthesis and Optical Properties of Hybrid and Alloy Plasmonic Nanoparticles. *Chem. Rev.* **2011**, 111, 3713−3735.

[3] Mayer, K. M.; Hafner, J. H., Localized Surface Plasmon Resonance Sensors. *Chem. Rev.* **2011**, *111* (6), 3828-3857.

[4] Jiang, N. N.; Zhuo, X. L.; Wang, J. F. Active Plasmonics: Principles, Structures, and Applications. *Chem. Rev.* **2018**, *118* (6), 3054-3099.

[5] Xia, Y.; Gilroy, K. D.; Peng, H. C.; Xia, X. Seed-Mediated Growth of Colloidal Metal Nanocrystals. *Angew. Chem., Int. Ed.* **2017**, 56, 60−95.

[6] Llevot, A.; Astruc, D. Applications of Vectorized Gold Nanoparticles to the Diagnosis and Therapy of Cancer. *Chem. Soc. Rev.* **2012**, *41*, 242-257.

[7] Halas, N. J.; Lal, S.; Chang, W.-S.; Link, S.; Nordlander, P. Plasmons in Strongly Coupled Metallic Nanostructures. *Chem. Rev.* **2011**, 111, 3913-3961.

[8] Ha, M.; Kim, J.-H.; You, M.; Li, Q.; Fan, C.; Nam, J.-M. Multicomponent Plasmonic Nanoparticles: From Heterostructured Nanoparticles to Colloidal Composite Nanostructures. *Chem. Rev.* **2019**, *119* (24), 12208-12278.

[9] Yang, K.; Yao, X.; Liu, B.; Ren, B., Metallic Plasmonic Array Structures: Principles, Fabrications, Properties, and Applications. *Adv. Mater.* **2021**, *33* (50), e2007988.

[10] Kahraman, M.; Daggumati, P.; Kurtulus, O.; Seker, E.; Wachsmann-Hogiu, S. Fabrication and Characterization of Flexible and Tunable Plasmonic Nanostructures. *Sci. Rep.* **2013**, 3, 3396.

[11] Kang, H.; Lee, D.; Yang, Y.; Kyo Oh, D.; Seong, J.; Kim, J.; Jeon, N.; Kang, D.; Rho, J., Emerging Low-Cost, Large-Scale Photonic Platforms with Soft Lithography and Self-Assembly. *Photon. Insig.* **2023**, 2 (2).

[12] Li, Z.; Liu, R.; Xing, G.; Wang, T.; Liu, S. A Novel Fluorometric and

Colorimetric Sensor for Iodide Determination Using DNA-Templated Gold/Silver Nanoclusters. *Biosens. Bioelectron.* **2017**, 96, 44-48.

[13] Alexander, K. D.; Skinner, K.; Zhang, S. P.; Wei, H.; Lopez, R. Tunable SERS in Gold Nanorod Dimers through Strain Control on an Elastomeric Substrate. *Nano Lett.* **2010**, 10, 4488-4493.

[14] Kang, M.; Kim, J.-J.; Oh, Y.-J.; Park, S.-G.; Jeong, K.-H. A Deformable Nanoplasmonic Membrane Reveals Universal Correlations between Plasmon Resonance and Surface Enhanced Raman Scattering. *Adv. Mater.* **2014**, 26, 4510-4514.

[15] Smith, J. G.; Faucheaux, J. A.; Jain, P. K. Plasmon Resonances for Solar Energy Harvesting: A Mechanistic Outlook. *Nano Today* **2015**, *10*, 67-80.

[16] Yeh, Y. C.; Creran, B.; Rotello, V. M. Gold Nanoparticles: Preparation, Properties, and Applications in Bionanotechnology. *Nanoscale* **2012**, *4*(6), 1871-1880.

[17] Guo, L. H.; Jackman, J. A.; Yang, H.-H.; Chen, P.; Cho, N.-J.; Kim, D.-H. Strategies for Enhancing the Sensitivity of Plasmonic Nanosensors. *Nano Today* **2015**, 10, 213-239.

[18] Fang, Z.; Liu, Z.; Wang, Y.; Ajayan, P. M.; Nordlander, P.; Halas, N. J. Graphene-Antenna Sandwich Photodetector. *Nano Lett.* **2012**, 12, 3808-3813.

[19] Grandidier, J.; des Francs, G. C.; Massenot, S.; Bouhelier, A.; Markey, L.; Weeber, J.-C.; Finot, C.; Dereux, A. Gain-Assisted Propagation in a Plasmonic Waveguide at Telecom Wavelength. *Nano Lett.* **2009**, 9, 2935-2939.

[20] Shi, X.; Gong, H.; Li, Y.; Wang, C.; Cheng, L.; Liu, Z. Graphene-Based Magnetic Plasmonic Nanocomposite for Dual Bioimaging and Photothermal Therapy. *Biomaterials* **2013**, 34, 4786-4793.

[21] Cortes, E.; Xie, W.; Cambiasso, J.; Jermyn, A. S.; Sundararaman, R.; Narang, P.; Schlucker, S.; Maier, S. A. Plasmonic Hot Electron Transport Drives Nano-Localized Chemistry. *Nat. Commun.* **2017**, *8*, 14880.

[22] Nguyen, L. B. T.; Leong, Y. X.; Koh, C. S. L.; Leong, S. X.; Boong, S. K.; Sim, H. Y. F.; Phan-Quang, G. C.; Phang, I. Y.; Ling, X. Y. Inducing Ring Complexation for Efficient Capture and Detection of Small Gaseous Molecules Using SERS for Environmental Surveillance. *Angew. Chem., Int. Ed.* **2022**, *61* (33), No. e202207447.

[23] Guan, T.; Liang, S.; Kang, Y.; Pensa, E.; Li, D.; Liang, W.; Liang, Z.; Bulut, Y,; Drewes, J.; Reck, K. A.; Xiao, T.; Guo, R.; Drewes, J.; Strunskus, T.; Schwartzkopf, M.; Faupel, F.; Roth, S. V.; Cortés, E.; Jiang, L.; Müller-Buschbaum, P., High-power Impulse Magnetron Sputter Deposition of Ag on

Self-assembled Au Nanoparticle Arrays at Low-Temperature Dewetting Conditions. *ACS Appl Mater Interfaces* **2024,** *16*(30), 40286-40296.

[24] Zhan, C.; Wang, Z. Y.; Zhang, X. G.; Chen, X. J.; Huang, Y. F.; Hu, S.; Li, J. F.; Wu, D. Y.; Moskovits, M.; Tian, Z. Q. Interfacial Construction of Plasmonic Nanostructures for the Utilization of the Plasmon-Excited Electrons and Holes. *J. Am. Chem. Soc.* **2019**, *141* (20), 8053-8057.

[25] Konstantatos, G. Current Status and Technological Prospect of Photodetectors based on Two-Dimensional Materials. *Nat. Commun.* **2018**, *9*, 5266.

[26] Wang, H.; Li, Z.; Li, D.; Chen, P.; Pi, L.; Zhou, X.; Zhai, T. Van der Waals Integration Based on Two-Dimensional Materials for High Performance Infrared Photodectors. *Adv. Funct. Mater.* **2021**, *31* (30), 2103106.

[27] Zhang, C.; Wu, K.; Giannini, V.; Li, X. F. Planar Hot-Electron Photodetection with Tamm Plasmons. *ACS Nano* **2017**, *11*, 1719-1727.

[28] Guan, T.; Chen, W.; Tang, H.; Li, D.; Wang, X.; Weindl, C. L.; Wang, Y.; Liang, Z.; Liang, S.; Xiao, T.; Tu, S.; Roth, S. V.; Jiang, L.; Müller-Buschbaum, P., Decoding the Self-Assembly Plasmonic Interface Structure in a PbS Colloidal Quantum Dot Solid for a Photodetector. *ACS Nano* **2023,** *17* (22), 23010-23019.

[29] Li, N.; Pratap, S.; Korstgens, V.; Vema, S.; Song, L.; Liang, S.; Davydok, A.; Krywka, C.; Müller-Buschbaum, P. Mapping Structure Heterogeneities and Visualizing Moisture Degradation of Perovskite Films with Nano-Focus WAXS. *Nat. Commun.* 2022, *13*, No. 6701.

[30] Müller-Buschbaum, P. Grazing Incidence Small-Angle X-Ray Scattering: An Advanced Scattering Technique for the Investigation of Nanostructured Polymer Films. *Anal. Bioanal. Chem.* **2003**, *376*, 3-10.

[31] Giannini, V.; Fernandez-Domínguez, A. I.; Heck, S. C.; Maier, S. A.́ Plasmonic Nanoantennas: Fundamentals and Their Use in Controlling the Radiative Properties of Nanoemitters. *Chem. Rev.* **2011**, *111*, 3888-3912.

[32] Li, M.; Cushing, S. K.; Wu, N., Plasmon-enhanced optical sensors: a review. *Analyst* **2015,** *140* (2), 386-406.

[33] Mie, G. Beitrage Zur Optik Truber Medien, Speziell Kolloidaler Metallosungen. *Ann. Phys. (Berlin, Ger.)* **1908**, *330*, 377-445.

[34] Xavier, J.; Vincent, S.; Meder, F.; Vollmer, F., Advances in Optoplasmonic Sensors Combining Optical Nano/Microcavities and Photonic Crystals with Plasmonic Nanostructures and Nanoparticles. *Nanophotonics* **2018,** *7* (1), 1-38.

[35] Gans, R. Uber Die Form Ultramikroskopischer Goldteilchen. *Ann. Phys. (Berlin, Ger.)* **1912**, *342*, 881-900.

[36] Shao, L.; Fang, C. H.; Chen, H. J.; Man, Y. C.; Wang, J. F.; Lin, H.-Q. Distinct Plasmonic Manifestation on Gold Nanorods Induced by the Spatial Perturbation of Small Gold Nanospheres. *Nano Lett.* **2012**, *12*, 1424-1430.

[37] Shedbalkar, U.; Singh, R.; Wadhwani, S.; Gaidhani, S.; Chopade, B. A. Microbial Synthesis of Gold Nanoparticles: Current Status and Future Prospects. *Adv. Colloid Interface Sci.* **2014**, *209*, 40-48.

[38] Link, S.; El-Sayed, M. A. Spectral Properties and Relaxation Dynamics of Surface Plasmon Electronic Oscillations in Gold and Silver Nanodots and Nanorods. *J. Phys. Chem. B* **1999**, *103* (40), 8410-8426.

[39] Aftenieva, O.; Schletz, D.; Meyer, A.; Kühne, T.; Schmalzriedt, S.; Niethammer, M.; König, T. A. F., Development of a Teaching Platform about Plasmonics Based on the Color Perception of Colloidal Gold. *Journal of Chemical Education* **2021,** *98* (8), 2566-2573.

[40] Bastus, N. G.; Comenge, J.; Puntes, V., Kinetically Controlled Seeded Growth Synthesis of Citrate-Stabilized Gold Nanoparticles of Up to 200 nm: Size Focusing Versus Ostwald Ripening. *Langmuir* **2011**, *27* (17), 11098-105.

[41] Jain, P. K.; Huang, X.; El-Sayed, I. H.; El-Sayed, M. A. Noble Metals on the Nanoscale: Optical and Photothermal Properties and Some Applications in Imaging, Sensing, Biology, and Medicine. *Acc. Chem. Res.* **2008**, *41* (12), 1578-1586.

[42] Lee, K.; Conboy, M.; Park, H. M.; Jiang, F.; Kim, H. J.; Dewitt, M. A.; Mackley, V. A.; Chang, K.; Rao, A.; Skinner, C.; Shobha, T.; Mehdipour, M.; Liu, H.; Huang, W.-c.; Lan, F.; Bray, N. L.; Li, S.; Corn, J. E.; Kataoka, K.; Doudna, J. A.; Conboy, I.; Murthy, N. Nanoparticle Delivery of Cas9 Ribonucleoprotein and Donor DNA In Vivo Induces Homology-Directed DNA repair. *Nat. Biomed. Eng.* **2017**, *1* (11), 889-901.

[43] Gibbs, J. W. On the Equilibrium of Heterogeneous Substances. *Transations Connect. Acad. Arts Sci.* **1878**, *3*, 343−524.

[44] Thanh, N. T. K.; Maclean, N.; Mahiddine, S. Mechanisms of Nucleation and Growth of Nanoparticles in Solution. *Chem. Rev.* **2014**, *114*, 7610−7630.

[45] Carbone, L.; Cozzoli, P. D. Colloidal Heterostructured Nanocrystals: Synthesis and Growth Mechanisms. *Nano Today* **2010**, *5*, 449-493.

[46] Ofir, Y.; Samanta, B.; Rotello, V. M. Biopolymer Mediated Self-Assembly of Gold Nanoparticle. *Chem. Soc. Rev.* **2008**, *37*, 1814-1825.

[47] Li, D.; Sun, Y.; Wang, Y.; Liu, Y.; Zhao, B.; Liang, W.; Gao, H.; Jiang, L., Facile Fabrication of a Single-Particle Platform with High Throughput via

Substrate Surface Potential Regulated Large-Spacing Nanoparticle Assembly. *Nano Research* **2022,** *15* (7), 6713-6720.

[48] Zhao, Y.; Jing, X.; Zheng, F.; Liu, Y.; Fan, Y., Surface-Enhanced Raman Scattering-Active Plasmonic Metal Nanoparticle-Persistent Luminescence Material Composite Films for Multiple Illegal Dye Detection. *Anal Chem* **2021,** *93* (25), 8945-8953.

[49] Yadav, A.; Gerislioglu, B.; Ahmadivand, A.; Kaushik, A.; Cheng, G. J.; Ouyang, Z.; Wang, Q.; Yadav, V. S.; Mishra, Y. K.; Wu, Y.; Liu, Y.; RamaKrishna, S., Controlled Self-Assembly of Plasmon-Based Photonic Nanocrystals for High Performance Photonic Technologies. *Nano Today* **2021,** *37*.

[50] Chen, W.; Tang, H.; Chen, Y.; Heger, J. E.; Li, N.; Kreuzer, L. P.; Xie, Y.; Li, D.; Anthony, C.; Pikramenou, Z.; Ng, K. W.; Sun, X. W.; Wang, K.; Müller-Buschbaum, P. Spray-Deposited PbS Colloidal Quantum Dot Solid for Near-Infrared Photodetectors. Nano Energy 2020, 78, 105254.

[51] Kershaw, S. V.; Susha, A. S.; Rogach, A. L. Narrow Bandgap Colloidal Metal Chalcogenide Quantum Dots: Synthetic Methods, Heterostructures, Assemblies, Electronic and Infrared Optical Properties. *Chem. Soc. Rev.* **2013**, *42*, 3033-3087.

[52] Cushing, S. K., Plasmonic Hot Carriers Skip Out in Femtoseconds. *Nature Photonics* **2017,** *11* (12), 748-749.

[53] Strelow, C.; Theuerholz, T. S.; Schmidtke, C.; Richter, M.; Merkl, J. P.; Kloust, H.; Ye, Z.; Weller, H.; Heinz, T. F.; Knorr, A.; et al. Metal-Semiconductor Nanoparticle Hybrids Formed by Self-Organization: A Platform to Address Exciton-Plasmon Coupling. *Nano Lett.* **2016**, *16*, 4811-4818.

[54] Sun, J.; Hu, H.; Zheng, D.; Zhang, D.; Deng, Q.; Zhang, S.; Xu, H. Light-Emitting Plexciton: Exploiting Plasmon-Exciton Interaction in the Intermediate Coupling Regime. *ACS Nano* **2018**, *12*, 10393-10402.

[55] Jin, Y.; Gao, X. Plasmonic Fluorescent Quantum Dots. *Nat. Nanotechnol.* **2009**, *4*, 571-576.

[56] Haldar, K. K.; Sinha, G.; Lahtinen, J.; Patra, A. Hybrid Colloidal Au-CdSe Pentapod Heterostructures Synthesis and Their Photocatalytic Properties. *ACS Appl. Mater. Interfaces* **2012**, *4*, 6266-6272.

[57] Yu, Y.; Ji, Z. H.; Zu, S.; Du, B. W.; Kang, Y. M.; Li, Z. W.; Zhou, Z. K.; Shi, K. B.; Fang, Z. Y. Ultrafast Plasmonic Hot Electron Transfer in Au Nanoantenna/MoS_2 Heterostructures. *Adv. Funct. Mater.* **2016**, *26*, 6394-6401.

[58] Shankar, S. S.; Rai, A.; Ahmad, A.; Sastry, M. Rapid Synthesis of Au, Ag, and Bimetallic Au Core-Ag Shell Nanoparticles using Neem (Azadirachta indica)

Leaf Broth. *J. Colloid Interface Sci.* **2004**, *275*, 496-502.

[59] Lin, M.; Kim, G. H.; Kim, J. H.; Oh, J. W.; Nam, J. M. Transformative Heterointerface Evolution and Plasmonic Tuning of Anisotropic Trimetallic Nanoparticles. *J. Am. Chem. Soc.* **2017**, *139*, 10180-10183.

[60] Wang, F.; Li, C. H.; Chen, H. J.; Jiang, R. B.; Sun, L. D.; Li, Q.; Wang, J. F.; Yu, J. C.; Yan, C. H. Plasmonic Harvesting of Light Energy for Suzuki Coupling Reactions. *J. Am. Chem. Soc.* **2013**, *135*, 5588-5601.

[61] Deng, S.; Zhang, B.; Choo, P.; Smeets, P. J. M.; Odom, T. W. Plasmonic Photoelectrocatalysis in Copper-Platinum Core-Shell Nanoparticle Lattices. *Nano Lett.* **2021**, *21*, 1523-1529.

[62] Sytwu, K.; Vadai, M.; Dionne, J. A. Bimetallic Nanostructures: Combining Plasmonic and Catalytic Metals for Photocatalysis. *Adv. Phys. X* **2019**, *4*, 1619480.

[63] Zhang, N.; Liu, S.; Fu, X.; Xu, Y. J. Synthesis of M@TiO_2 (M = Au, Pd, Pt) Core-Shell Nanocomposites with Tunable Photoreactivity. *J. Phys. Chem. C* **2011**, *115*, 9136-9145.

[64] Zhu, C.; Zeng, J.; Tao, J.; Johnson, M. C.; Schmidt-Krey, I.; Blubaugh, L.; Zhu, Y. M.; Gu, Z. Z.; Xia, Y. N. Kinetically Controlled Overgrowth of Ag or Au on Pd Nanocrystal Seeds: From Hybrid Dimers to Nonconcentric and Concentric Bimetallic Nanocrystals. *J. Am. Chem. Soc.* **2012**, *134*, 15822-15831.

[65] Liu, K.; Bai, Y.; Zhang, L.; Yang, Z.; Fan, Q.; Zheng, H.; Yin, Y.; Gao, C. Porous Au-Ag Nanospheres with High-Density and Highly Accessible Hotspots for SERS Analysis. *Nano Lett.* **2016**, *16*, 3675-3681.

[66] Tolan M.; and Tolan M. X-ray Scattering from Soft-Matter Thin Films: Materials Science and Basic Research, *Springer*, **1999**, 148.

[67] Foster M. D. X-ray Scattering Methods for the Study of Polymer Interfaces, *Crit. Rev. Anal. Chem.*, **1993,** *24* (3), 179–241.

[68] Sun, Y. Anomalous Small-Angle X-ray Scattering for Materials Chemistry. *Trends Chem.* **2021**, *3*, 1045-1060.

[69] Gommes, C. J.; Jaksch, S.; Frielinghaus, H. Small-Angle Scattering for Beginners. *J. Appl. Crystallogr.* **2021**, *54*, 1832-1843.

[70] Yoneda, Y. Anomalous Surface Reflections of X-Rays. *Phys. Rev.* **1963**, *131*, 2010.

[71] Gilbert, J. A.; Kariuki, N. N.; Subbaraman, R.; Kropf, A. J.; Smith, M. C.; Holby, E. F.; Morgan, D.; Myers, D. J. *In Situ* Anomalous Small-Angle X-ray Scattering

Studies of Platinum Nanoparticle Fuel Cell Electrocatalyst Degradation. *J. Am. Chem. Soc.* **2012**, *134*, 14823-14833.

[72] Rocha, F. S.; Gomes, A. J.; Lunardi, C. N.; Kaliaguine, S.; Patience, G. S., Experimental Methods in Chemical Engineering: Ultraviolet Visible Spectroscopy UV-Vis. *The Canadian J. Chem. Engineer.* **2018,** *96* (12), 2512-2517.

[73] Campanella, B.; Palleschi, V.; Legnaioli, S., Introduction to Vibrational Spectroscopies. *Chem. Texts* **2021,** *7* (1).

[74] Pospelov, G.; Van Herck, W.; Burle, J.; Carmona Loaiza, J. M.; Durniak, C.; Fisher, J. M.; Ganeva, M.; Yurov, D.; Wuttke, J. BornAgain: Software for Simulating and Fitting Grazing-Incidence Small-Angle Scattering. *J. Appl. Crystallogr.* **2020**, *53*, 262-276.

[75] Wang, C.; Zhao, X.-P.; Xu, Q.-Y.; Nie, X.-G.; Younis, M. R.; Liu, W.-Y.; Xia, X.-H. Importance of Hot Spots in Gold Nanostructures on Direct Plasmon-Enhanced Electrochemistry. *ACS Appl. Nano Mater.* **2018**, *1*, 5805-5811.

[76] Zhu, C.; Yang, G.; Li, H.; Du, D.; Lin, Y. Electrochemical Sensors and Biosensors Based on Nanomaterials and Nanostructures. *Anal. Chem.* **2015**, *87*, 230-249.

[77] Jiang, R.; Li, B.; Fang, C.; Wang, J. Metal/Semiconductor Hybrid Nanostructures for Plasmon-Enhanced Applications. *Adv. Mater.* **2014**, *26*, 5274-5309.

[78] Azzam, S. I.; Kildishev, A. V.; Ma, R. M.; Ning, C. Z.; Oulton, R.; Shalaev, V. M.; Stockman, M. I.; Xu, J. L.; Zhang, X. Ten Years of Spasers and Plasmonic Nanolasers. *Light Sci. Appl.* **2020**, *9*, 90.

[79] Zhang, J.; Wang, Y.; Li, D.; Sun, Y.; Jiang, L. Engineering Surface Plasmons in Metal/Nonmetal Structures for Highly Desirable Plasmonic Photodetectors. *ACS Mater. Lett.* **2022**, *4* (2), 343-355.

[80] Boltasseva, A.; Atwater, H. A.; Low-Loss Plasmonic Metamaterials. *Science* **2011**, *331*, 290-291.

[81] Guo, C.; Yu, J.; Deng, S. Hybrid Metasurfaces of Plasmonic Lattices and 2D Materials. *Adv. Funct. Mater.* **2023**, *33*, 2302265

[82] Yang, H.; Li, D.; Zheng, X.; Zuo, J.; Zhao, B.; Li, D.; Zhang, J.; Liang, Z.; Jin, J.; Ju, S.; Peng, M.; Sun, Y.; Jiang, L. High Freshwater Flux Solar Desalination via a 3D Plasmonic Evaporator with an Efficient Heat-Mass Evaporation Interface. *Adv. Mater.* **2023**, *35*, e2304699.

[83] Itoh, T.; Prochazka, M.; Dong, Z. C.; Ji, W.; Yamamoto, Y. S.; Zhang, Y.; Ozaki, Y. Toward a New Era of SERS and TERS at the Nanometer Scale: From

Fundamentals to Innovative Applications. *Chem. Rev.* **2023**, *123*, 1552-1364.

[84] Yang, J.; Zhang, X.; Zhang, X.; Wang, L.; Feng, W.; Li, Q. Responsive Soft Actuators with MXene Nanomaterials. *Adv. Mater.* **2021**, *33*, e2004754.

[85] Gao, Y.; Cheng, F.; Fang, W.; Liu, X.; Wang, S.; Nie, W.; Chen, R.; Ye, S.; Zhu, J.; An, H.; Fan, C.; Fan, F.; Li, C. Probing of Coupling Effect Induced Plasmonic Charge Accumulation for Water Oxidation. *Nati. Sci. Rev.* **2021**, *8*, nwaa151.

[86] Stefancu, A.; Gargiulo, J.; Laufersky, G.; Auguié, B.; Chiş, V.; Le Ru, E. C.; Liu, M.; Leopold, N.; Cortés, E. Interface-Dependent Selectivity in Plasmon-Driven Chemical Reactions. *ACS Nano* **2023**, *17*, 3119-3127.

[87] Lim, D. K.; Jeon, K. S.; Hwang, J. H.; Kim, H.; Kwon, S.; Suh, Y. D.; Nam, J. M. Highly Uniform and Reproducible Surface-enhanced Raman Scattering from DNA-tailorable Nanoparticles with 1-nm Interior Gap. *Nat. Nanotechnol.* **2011**, *6*, 452-460.

[88] Bell, S. E. J.; Charron, G.; Cortés, E.; Kneipp, J.; Chapelle, M. L.; Langer, J.; Procházka, M.; Tran, V.; Schlgcker, S. Towards Reliable and Quantitative Surface-Enhanced Raman Scattering (SERS): From Key Parameters to Good Analytical Practice. *Angew. Chem. Int. Ed.* **2020**, *59*, 5454.

[89] Chen, Y.; Zhu, D.; Zhong, H.; Gan, Z.; Zong, S.; Wang, Z.; Cui, Y.; Wang, Y. Ultrasensitive Detection of Matrix Metalloproteinase 2 Activity Using a Ratiometric Surface-Enhanced Raman Scattering Nanosensorwith a Core-Satellite Structure. *ACS Appl. Mater. Interfaces* **2024**, *16*, 3, 4160–4168.

[90] Peng, J.; Lin, Q.; Foldes, T.; Jeong, H. H.; Xiong, Y.; Pitsalidis, C.; Malliaras, G. G.; Rosta, E.; Baumberg, J. J. In-Situ Spectro-Electrochemistry of Conductive Polymers Using Plasmonics to Reveal Doping Mechanisms. *ACS Nano* **2022**, *16*, 21120-21128.

[91] Juang, R.-S.; Wang, K.-S.; Cheng, Y.-W.; Fu, C.-C.; Chen, W.-T.; Liu, C.-M.; Chien, C.-C.; Jeng, R.-J.; Chen, C.-C.; Liu, T.-Y., Floating SERS Substrates of Silver Nanoparticles-Graphene Based Nanosheets for Rapid Detection of Biomolecules and Clinical Uremic Toxins. Colloids and Surfaces A: Physicochem. *Eng. Aspects* **2019**, *576*, 36-42.

[92] Son, W. K.; Choi, Y. S.; Han, Y. W.; Shin, D. W.; Min, K.; Shin, J.; Lee, M. J.; Son, H.; Jeong, D. H.; Kwak, S. Y. In Vivo Surface-enhanced Raman Scattering Nanosensor for the Real-time Monitoring of Multiple Stress Signalling Molecules in Plants. *Nat. Nanotechnol.* **2023**, *18*, 205-216.

[93] Chen, Y. W.; Liu, T. Y.; Chen, P. J.; Chang, P. H.; Chen, S. Y., A High-Sensitivity and Low-Power Theranostic Nanosystem for Cell SERS Imaging and Selectively

Photothermal Therapy Using Anti-EGFR-Conjugated Reduced Graphene Oxide/Mesoporous Silica/AuNPs Nanosheets. *Small* **2016**, *12* (11), 1458-1468.

[94] Zhu, R.; Feng, H.; Li, Q.; Su, L.; Fu, Q.; Li, J.; Song, J.; Yang, H. Asymmetric Core–Shell Gold Nanoparticles and Controllable Assemblies for SERS Ratiometric Detection of MicroRNA. *Angew Chem. Int. Ed. Engl.* **2021**, *60*, 12560-12676.

[95] Yang, M.-C.; Hardiansyah, A.; Cheng, Y.-W.; Liao, H.-L.; Wang, K.-S.; Randy, A.; Harito, C.; Chen, J.-S.; Jeng, R.-J.; Liu, T.-Y., Reduced Graphene Oxide Nanosheets Decorated with Core-Shell of Fe_3O_4-Au Nanoparticles for Rapid SERS Detection and Hyperthermia Treatment of Bacteria. *Spectrochim. Acta Part A: Molecular and Biomolecular Spectroscopy* **2022**, 281.

[96] Chen, Y.-F.; Wang, C.-H.; Chang, W.-R.; Li, J.-W.; Hsu, M.-F.; Sun, Y.-S.; Liu, T.-Y.; Chiu, C.-W., Hydrophilic–Hydrophobic Nanohybrids of AuNP-Immobilized Two-Dimensional Nanomica Platelets as Flexible Substrates for High-Efficiency and High-Selectivity Surface-Enhanced Raman Scattering Microbe Detection. *ACS Appl. Bio Mater.* **2022**, *5* (3), 1073-1083.

[97] Liang, S.; Schwartzkopf, M.; Roth, S. V.; Müller-Buschbaum, P. State of the Art of Ultra-thin Gold Layers: Formation Fundamentals and Applications. *Nanoscale Adv.* **2022**, *4*, 2533-2560.

[98] Skorikov, A.; Albrecht, W.; Bladt, E.; Xie, X.; van der Hoeven, J. E. S.; van Blaaderen, A.; Van Aert, S.; Bals, S. Quantitative 3D Characterization of Elemental Diffusion Dynamics in Individual Ag@Au Nanoparticles with Different Shapes. *ACS Nano* **2019**, *13*, 13421-13429.

[99] Wang, G.; Hao, C.; Ma, W.; Qu, A.; Chen, C.; Xu, J.; Xu, C.; Kuang, H.; Xu, L. Chiral Plasmonic Triangular Nanorings with SERS Activity for Ultrasensitive Detection of Amyloid Proteins in Alzheimer's Disease. *Adv. Mater.* **2021**, *33*, e2102337.

[100] Li, L.; Jiang, R.; Shan, B.; Lu, Y.; Zheng, C.; Li, M. Near-infrared II Plasmonic Porous Cubic Nanoshells for in Vivo Noninvasive SERS Visualization of Sub-millimeter Microtumors. *Nat. Commun.* **2022**, *13*, 5249.

[101] Wang, J.; Coillet, A.; Demichel, O.; Wang, Z.; Rego, D.; Bouhelier, A.; Grelu, P.; Cluzel, B. Saturable plasmonic metasurfaces for laser mode locking. *Light Sci. Appl.* **2020**, *9*, 50.

[102] Vinnacombe-Willson, G. A.; Conti, Y.; Stefancu, A.; Weiss, P.S.; Cortés, E.; Scaramella, L. Direct Bottom-Up *In Situ* Growth: A Paradigm Shift for Studies in Wet-Chemical Synthesis of Gold Nanoparticles. *Chem. Rev.* **2023**, *123*, 8488-8529.

[103] Zheng, D.; Pisano, F.; Collard, L.; Balena, A.; Pisanello, M.; Spagnolo, B.; Mach-Batlle, R.; Tantussi, F.; Carbone, L.; De Angelis, F.; Valiente, M.; de la Prida, L. M.; Ciraci, C.; De Vittorio, M.; Pisanello, F. Toward Plasmonic Neural Probes: SERS Detection of Neurotransmitters through Gold-Nanoislands-Decorated Tapered Optical Fibers with Sub-10 nm Gaps. *Adv. Mater.* **2023**, *35*, e2200902.

[104] Khitous, A.; Molinaro, C.; Gree, S.; Haupt, K.; Soppera, O. Plasmon-Induced Photopolymerization of Molecularly Imprinted Polymers for Nanosensor Applications. *Adv. Mater. Interfaces* **2023**, *10*, 2201651.

[105] Awasthi, V.; Malik, P.; Goel, R.; Srivastava, P.; Dubey, S. K. Nanogap-Rich Surface-Enhanced Raman Spectroscopy-Active Substrate Based on Double-Step Deposition and Annealing of the Au Film over the Back Side of Polished Si. *ACS Appl. Mater. Interfaces* **2023**, *15*, 10250−10260.

[106] Kozioł, R.; Łapiński, M.; Syty, P.; Sadowski, W.; Sienkiewicz, J. E.; Nurek, B.; Maraloiu, V. A.; Kościelska, B. Experimental Tuning of AuAg Nanoalloy Plasmon Resonances Assisted by Machine Learning Method. *Appl. Surf. Sci.* **2021**, *567*, 15082.

[107] Yasuhara, A.; Sannomiya, T. Atomically Localized Ordered Phase and Segregation at Grain Boundaries in Au-Ag-Cu Ternary Alloy Nanoparticles. *J. Phys. Chem. C* **2022**, *126*, 1160−1167.

[108] Gentili, D.; Giulia, F.; Francesco, V.; Massimiliano, C.; Fabio, B. Applications of Dewetting in Micro and Nanotechnology. *Chem. Soc. Rev.* **2012**, *41*, 4430−4443.

[109] Abelson, A.; Qian, C.; Salk, T.; Luan, Z.; Fu, K.; Zheng, J. G.; Wardini, J. L.; Law, M. Collective Topo-epitaxy In the Self-assembly of a 3D Quantum Dot Superlattice. *Nat. Mater.* **2020**, 19, 49-55.

[110] Guo, R.; Han, D.; Chen, W.; Dai, L.; Ji, K.; Xiong, Q.; Li, S.; Reb, L. K.; Scheel, M. A.; Pratap, S.; Li, N.; Yin, S.; Xiao, T.; Liang, S.; Oechsle, A. L.; Weindl, C. L.; Schwartzkopf, M.; Ebert, H.; Gao, P.; Wang, K.; Yuan, M.; Greenham, N. C.; Stranks, S. D.; Roth, S. V.; Friend, R. H.; Müller-Buschbaum, P. Degradation Mechanisms of Perovskite Solar Cells Under Vacuum and One Atmosphere of Nitrogen. *Nat. Energy* **2022**, *7*, 459.

[111] Gao, L.; Quan, L. N.; García de Arquer, F. P.; Zhao, Y.; Munir, R.; Proppe, A.; Quintero-Bermudez, R.; Zou, C.; Yang, Z.; Saidaminov, M. I.; Voznyy, O.; Kinge, S.; Lu, Z.; Kelley, S. O.; Amassian, A.; Tang, J.; Sargent, E. H. Efficient Near-infrared Light-emitting Diodes Based on Quantum Dots in Layered Perovskite. *Nat. Photonics* **2020**, *14*, 227-233.

[112] Mitra, S.; Basak, M. Diverse Bio-sensing and Therapeutic Applications of Plasmon Enhanced Nanostructures. *Mater. Today* **2022**, *57*, 225-261

[113] Pekdemir, S.; Torun, I.; Sakir, M.; Ruzi, M.; Rogers, J. A.; Onses, M. S. Chemical Funneling of Colloidal Gold Nanoparticles on Printed Arrays of End-Grafted Polymers for Plasmonic Applications *ACS Nano* **2020**, *14*, 8276-8286.

[114] Atlan, C.; Chatelier, C.; Martens, I.; Dupraz, M.; Viola, A.; Li, N.; Gao, L.; Leake, S. J.; Schulli, T. U.; Eymery, J.; Maillard, F.; Richard, M. I. Imaging the Strain Evolution of a Platinum Nanoparticle Under Electrochemical Control. *Nat. Mater.* **2023**, *22*, 754-761.

[115] Li, Q.; Chen, F.; Kang, J.; Su, J.; Huang, F.; Wang, P.; Yang, X.; Hou, Y. Physical Unclonable Anticounterfeiting Electrodes Enabled by Spontaneously Formed Plasmonic Core-Shell Nanoparticles for Traceable Electronics. *Adv. Funct. Mater.* **2021**, *31*, 2010537.

[116] Schwartzkopf, M.; Rothkirch, A.; Carstens, N.; Chen, Q.; Strunskus, T.; Löhrer, F. C.; Xia, S.; Rosemann, C.; Bießmann, L.; Körstgens, V.; Ahuja, S.; Pandit, P.; Rubeck, J.; Frenzke, S.; Hinz, A.; Polonskyi, O.; Müller-Buschbaum, P.; Faupel, F.; Roth S. V. *In Situ* Monitoring of Scale Effects on Phase Selection and Plasmonic Shifts during the Growth of AgCu Alloy Nanostructures for Anticounterfeiting Applications. *ACS Appl. Nano Mater.* **2022**, *5*, 3832-3842.

[117] Wei, W.; Bai, F.; Fan, H. Oriented Gold Nanorod Arrays: Self-Assembly and Optoelectronic Applications. *Angew Chem. Int. Ed. Engl.* **2019**, *58*, 11956-11966

[118] Santoro, G.; Yu, S.; Schwartzkopf, M.; Zhang, P.; Vayalil, S. K.; Risch, J. F. H.; Rübhausen, M. A.; Hernández, M.; Domingo, C.; Roth, S. V. Silver Substrates for Surface Enhanced Raman Scattering: Correlation Between Nanostructure and Raman Scattering Enhancement. *Appl. Phys. Lett.* **2014**, *104*, 243107.

[119] Park, S. G.; Xiao, X.; Min, J.; Mun, C.; Jung, H. S.; Giannini, V.; Weissleder, R.; Maier, S. A.; Im, H.; Kim, D. H. Self-Assembly of Nanoparticle-Spiked Pillar Arrays for Plasmonic Biosensing. *Adv. Funct. Mater.* **2019**, *29*, 1904257.

[120] Tian, L.; Gandra, N.; Singamaneni, S. Monitoring Controlled Release of Payload from Gold Nanocages Using Surface Enhanced Raman Scattering. *ACS Nano* **2013**, *7*, 4252-4260.

[121] Qian, H.; Anwer, S.; Bharath, G.; Iqbal, S.; Chen, L. Nanoporous Ag-Au Bimetallic Triangular Nanoprisms Synthesized by Galvanic Replacement for Plasmonic Applications. *J. Nanomater.* **2018**, 1-7.

[122] Yang, Y.; Liu, J.; Fu, Z. W.; Qin, D. Galvanic ReplacementFree Deposition of

Au on Ag for Core-Shell Nanocubes with Enhanced Chemical Stability and SERS Activity. *J. Am. Chem. Soc.* **2014**, *136*, 8153-8156.

[123] Mao, S.; Liu, J.; Pan, Y.; Lee, J.; Yao, Z.; Pandey, P.; Kunwar, S.; Zhu, Z.; Shen, W.; Belfiore, L. A.; Tang, J. Morphological and Optical Evolution of Metallic Oxide/Au Nanoparticle Hybrid Thin Film: High Absorption and Reflectance by Plasmonic Enhancement. *Appl. Surf. Sci.* **2019**, *495*, 143575.

[124] Zhang, T.; Sun, Y.; Hang, L.; Li, H.; Liu, G.; Zhang, X.; Lyu, X.; Cai, W.; Li, Y. Periodic Porous Alloyed Au-Ag Nanosphere Arrays and Their Highly Sensitive SERS Performance with Good Reproducibility and High Density of Hotspots. *ACS Appl. Mater. Interfaces* **2018**, *10*, 9792-9801.

[125] Deriu, C.; Morozov, A. N.; Mebel, A. M. Direct and Water-Mediated Adsorption of Stabilizers on SERS-Active ColloidalBimetallic Plasmonic Nanomaterials: Insight into Citrate-AuAg Interactions from DFT Calculations. *J. Phys. Chem. A* **2022**, *126*, 5236−5251.

[126] Shao, M.; Ji, C.; Tan, J.; Du, B.; Zhao, X.; Yu, J.; Man, B.; Xu, K.; Zhang, C.; Li, Z., Ferroelectrically Modulate the Fermi Level of Graphene Oxide to Enhance SERS Response. *Opto-Electron. Adv.* **2023**, *6* (11), 230094-230094.

[127] Bai, S.; Ren, X.; Obata, K.; Ito, Y.; Sugioka, K., Label-Free Trace Detection of Bio-Molecules by Liquid-Interface Assisted Surface-Enhanced Raman Scattering Using a Microfluidic Chip. *Opto-Electron. Adv.* **2022**, *5* (10), 210121-210121.

[128] Pei, Z.; Li, J.; Ji, C.; Tan, J.; Shao, Z.; Zhao, X.; Li, Z.; Man, B.; Yu, J.; Zhang, C., Flexible Cascaded Wire-in-Cavity-in-Bowl Structure for High-Performance and Polydirectional Sensing of Contaminants in Microdroplets. *J. Phys. Chem. Lett.* **2023**, *14* (25), 5932-5939.

[129] Peng, G.-Z.; Hardiansyah, A.; Lin, H.-T.; Lee, R.-Y.; Kuo, C.-Y.; Pu, Y.-C.; Liu, T.-Y., Photocatalytic Degradation and Reusable SERS Detection by Ag Nanoparticles Immobilized on g-C_3N_4/Graphene Oxide Nanosheets. *Surf. Coat. Tech.* **2022**, 435.

[130] Ahmed, I.; Shi, L.; Pasanen, H.; Vivo, P.; Maity, P.; Hatamvand, M.; Zhan, Y. There is Plenty of Room at the Top: Generation of Hot Charge Carriers and Their Applications in Perovskite and Other Semiconductor-Based Optoelectronic Devices. *Light Sci. Appl.* **2021**, *10*, 174.

[131] Ueno, K.; Oshikiri, T.; Sun, Q.; Shi, X.; Misawa, H., Solid-State Plasmonic Solar Cells. *Chem. Rev.* **2018**, *118*, 2955-2993.

[132] Li, S.; Chui, K. K.; Shen, F.; Huang, H.; Wen, S.; Yam, C.; Shao, L.; Xu, J.;

Wang, J. Generation and Detection of Strain-Localized Excitons in WS_2 Monolayer by Plasmonic Metal Nanocrystals. *ACS Nano* **2022**, *16*, 10647-10656.

[133] Li, X.; Liu, X.; Liu, X. Self-assembly of Colloidal Inorganic Nanocrystals: Nanoscale Forces, Emergent Properties and Applications. *Chem. Soc. Rev.* **2021**, *50*, 2074-2101.

[134] Langer, J.; Jimenez de Aberasturi, D.; Aizpurua, J.; Alvarez-Puebla, R. A.; Auguie, B.; Baumberg, J. J.; Bazan, G. C.; Bell, S. E. J.; Boisen, A.; Brolo, A. G.; Choo, J.; Cialla-May, D.; Deckert, V.; Fabris, L.; Faulds, K.; Garcia de Abajo, F. J.; Goodacre, R.; Graham, D.; Haes, A. J.; Haynes, C. L.; et al. Present and Future of Surface-Enhanced Raman Scattering. *ACS Nano* **2020**, *14*, 28-117.

[135] Park, C.; Han, S. H.; Jin, H. J.; Hong, W.; Choi, S. Y. Plasmonic Nanoparticles on Graphene Absorber for Broadband High Responsivity 2D/3D Photodiode. *ACS Nano* **2023**, *17*, 9262−9271.

[136] Konstantatos, G.; Sargent, E. H. Nanostructured Materials for Photon Detection. *Nat. Nanotechnol.* **2010**, *5*, 391-400.

[137] Collins, S. S. E.; Searles, E. K.; Tauzin, L. J.; Lou, M.; Bursi, L.; Liu, Y.; Song, J.; Flatebo, C.; Baiyasi, R.; Cai, Y. Y.; Foerster, B.; Lian, T.; Nordlander, P.; Link, S.; Landes, C. F. Plasmon Energy Transfer in Hybrid Nanoantennas. *ACS Nano* **2021**, *15*, 9522-9530.

[138] Linic, S.; Chavez, S.; Elias, R. Flow and Extraction of Energy and Charge Carriers in Hybrid Plasmonic Nanostructures. *Nat. Mater.* **2021**, *20*, 916-924.

[139] Zada, A.; Muhammad, P.; Ahmad, W.; Hussain, Z.; Ali, S.; Khan, M.; Khan, Q.; Maqbool, M. Surface Plasmonic-Assisted Photocatalysis and Optoelectronic Devices with Noble Metal Nanocrystals: Design, Synthesis, and Applications. *Adv. Funct. Mater.* **2019**, *30*, 1906744.

[140] Elbanna, A.; Jiang, H.; Fu, Q. D.; Zhu, J. F.; Liu, Y. D.; Zhao, M.; Liu, D. J.; Lai, S. M.; Chua, X. W.; Pan, J. S.; Shen, Z. X.; Wu, L.; Liu, Z.; Qiu, C. W.; Teng, J. H. 2D Material Infrared Photonics and Plasmonics. *ACS Nano* **2023**, *17*, 4134-4179.

[141] Lin, K.-T.; Lin, H.; Jia, B. Plasmonic Nanostructures in Photodetection, Energy Conversion and Beyond. *Nanophotonics* **2020**, *9*, 3135-3163.

[142] Zheng, M. F.; Fang, G. J. Luminescence Enhancement of Lead Halide Perovskite Light-Emitting Diodes with Plasmonic Metal Nanostructures. *Nanoscale* **2021**, *13*, 16427-16447.

[143] Chen, M.; Lu, L.; Yu, H.; Li, C.; Zhao, N. Integration of Colloidal Quantum Dots with Photonic Structures for Optoelectronic and Optical Devices. *Adv. Sci.*

2021, *8*, e2101560.

[144] Lavrentiev, V.; Chvostova, D.; Pokorny, J.; Lavrentieva, I.; Vacik, J.; Dejneka, A. Tuneable Interplay of Plasmonic and Molecular Excitations in Self-assembled Silver-Fullerene Nanocomposites. *Carbon* **2021**, *184*, 34-42.

[145] Park, J. E.; Lopez-Arteaga, R.; Sample, A. D.; Cherqui, C. R.; Spanopoulos, I.; Guan, J.; Kanatzidis, M. G.; Schatz, G. C.; Weiss, E. A.; Odom, T. W. Polariton Dynamics in Two-Dimensional Ruddlesden-Popper Perovskites Strongly Coupled with Plasmonic Lattices. *ACS Nano* **2022**, *16*, 3917-3925.

[146] Wang, T.; Zheng, D.; Zhang, J.; Qiao, J.; Min, C.; Yuan, X.; Somekh, M.; Feng, F. High-Performance and Stable Plasmonic-Functionalized Formamidinium-Based Quasi-2D Perovskite Photodetector for Potential Application in Optical Communication. *Adv. Funct. Mater.* **2022**, *32*, 2208694.

[147] Huang, J.-A.;Luo, L.-B. Low-Dimensional Plasmonic Photodetectors: Recent Progress and Future Opportunities. *Adv. Opt. Mater.* **2018**, *6*, 1701282.

[148] Sokolowski, K.; Huang, J.; Foldes, T.; McCune, J. A.; Xu, D. D.; de Nijs, B.; Chikkaraddy, R.; Collins, S. M.; Rosta, E.; Baumberg, J. J.; Scherman, O. A. Nanoparticle Surfactants for Kinetically Arrested Photoactive Assemblies to Track Light-induced Electron Transfer. *Nat. Nanotechnol.* **2021**, *16* (10), 1121-1129.

[149] Klein, M.; Binder, R.; Koehler, M. R.; Mandrus, D. G.; Taniguchi, T.; Watanabe, K.; Schaibley, J. R. Slow Light in a 2D Semiconductor Plasmonic Structure. *Nat. Commun.* **2022**, *13*, 6216.

[150] Lu, M.; Zhu, H.; Bazuin, C. G.; Peng, W.; Masson, J. F. Polymer-Templated Gold Nanoparticles on Optical Fibers for Enhanced-Sensitivity Localized Surface Plasmon Resonance Biosensors. *ACS Sens.* **2019**, *4*, 613-622.

[151] Li, D.; Sun, Y. H.; Wang, Z. S.; Huang, J.; Lu, N.; Jiang, L. Large-scale Multiplexed Surface Plasmonic Gold Nanostructures Based on Nanoimprint and Self-assembly. Chem. J. Chin. Univ.2020, 41, 221−227.

[152] Zhang, J.; Zhong, L.; Sun, Y.; Li, A.; Huang, J.; Meng, F.; Chandran, B. K.; Li, S.; Jiang, L.; Chen, X. Enhanced Photoresponse of Conductive Polymer Nanowires Embedded with Au Nanoparticles. *Adv. Mater.* **2016**, *28*, 2978-2982.

[153] Wang, J. L.; Fang, H. H.; Wang, X. D.; Chen, X. S.; Lu, W.; Hu,W. D. Recent Progress on Localized Field Enhanced Two-dimensional Material Photodetectors from Ultraviolet-Visible to Infrared. *Small* **2017**, *13*, 1700894.

[154] Liu, M.; Yazdani, N.; Yarema, M.; Jansen, M.; Wood, V.; Sargent, E. H. Colloidal Quantum Dot Electronics. *Nat. Electron.* **2021**, *4*, 548-558.

[155] Litvin, A. P.; Martynenko, I. V.; Purcell-Milton, F.; Baranov, A. V.; Fedorov, A. V.; Gun'ko, Y. K. Colloidal Quantum Dots for Optoelectronics. *J. Mater. Chem. A* **2017**, *5*, 13252-13275.

[156] Yin, X.; Zhang, C.; Guo, Y.; Yang, Y.; Xing, Y.; Que, W. PbS QD-Based Photodetectors: Future-Oriented Near-Infrared Detection Technology. *J. Mater. Chem. C* **2021**, *9*, 417-438.

[157] Huang, J.; Ojambati, O. S.; Chikkaraddy, R.; Sokolowski, K.; Wan, Q.; Durkan, C.; Scherman, O. A.; Baumberg, J. J. Plasmon-Induced Trap State Emission from Single Quantum Dots. *Phys. Rev. Lett.* **2021**, *126* (4), 047402.

[158] Santhosh, K.; Bitton, O.; Chuntonov, L.; Haran, G. Vacuum Rabi Splitting in a Plasmonic Cavity at the Single Quantum Emitter Limit. *Nat. Commun.* **2016**, *7*, 11823.

[159] Kholmicheva, N.; Moroz, P.; Bastola, E.; Razgoniaeva, N.; Bocanegra, J.; Shaughnessy, M.; Porach, Z.; Khon, D.; Zamkov, M. Mapping the Exciton Diffusion in Semiconductor Nanocrystal Solids. *ACS Nano* **2015**, *9*, 2926-2937.

[160] Chen, S.; Wang, Y. J.; Liu, Q. P.; Shi, G. Z.; Liu, Z. K.; Lu, K. Y.; Han, L.; Ling, X. F.; Zhang, H.; Cheng, S.; Ma, W. L. Broadband Enhancement of PbS Quantum Dot Solar Cells by the Synergistic Effect of Plasmonic Gold Nanobipyramids and Nanospheres. *Adv. Energy Mater.* **2018**, *8*, 1701194.

[161] Chen, W.; Guo, R.; Tang, H.; Wienhold, K. S.; Li, N.; Jiang, Z.; Tang, J.; Jiang, X.; Kreuzer, L. P.; Liu, H.; Schwartzkopf, M.; Sun, X. W.; Roth, S. V.; Wang, K.; Xu, B.; Müller-Buschbaum, P. Operando Structure Degradation Study of PbS Quantum Dot Solar Cells. *Energy Environ. Sci.* **2021**, *14*, 3420-3429.

[162] Melendez, L. V.; Van Embden, J.; Connell, T. U.; Duffy, N. W.; Gomez, D. E. Optimal Geometry for Plasmonic Hot-Carrier Extraction in Metal-Semiconductor Nanocrystals. *ACS Nano* **2023**, *17*, 4659-4666.

[163] Kress, S. J. P.; Cui, J.; Rohner, P.; Kim, D. K.; Antolinez, F. V.; Zaininger, K. A.; Jayanti, S. V.; Richner, P.; McPeak, K. M.; Poulikakos, D.; Norris, D. J. A Customizable Class of Colloidal-Quantum-Dot Spasers and Plasmonic Amplifiers. *Sci. Adv.* **2022**, *8*, e1700688.

[164] Wang, L.; Han, L.; Guo, W.; Zhang, L.; Yao, C.; Chen, Z.; Chen, Y.; Guo, C.; Zhang, K.; Kuo, C. N.; Lue, C. S.; Politano, A.; Xing, H.; Jiang, M.; Yu, X.; Chen, X.; Lu, W. Hybrid Dirac Semimetal-Based Photodetector with Efficient Low-Energy Photon Harvesting. *Light Sci. Appl.* **2022**, *11*, 53.

[165] Kholmicheva, N.; Moroz, P.; Eckard, H.; Jensen, G.; Zamkov, M. Energy Transfer in Quantum Dot Solids. *ACS Energy Lett.* **2016**, *2*, 154-160.

[166] Paracini, N.; Gutfreund, P.; Welbourn, R.; Gonzalez-Martinez, J. F.; Zhu, K.; Miao, Y.; Yepuri, N.; Darwish, T. A.; Garvey, C.; Waldie, S.; Larsson, J.; Wolff, M.; Cardenas, M. Structural Characterization of Nanoparticle-Supported Lipid Bilayer Arrays by Grazing Incidence X-Ray and Neutron Scattering. *ACS Appl. Mater. Interfaces* **2023**, *15*, 3772-3780.

[167] Liang, S.; Guan, T.; Yin, S.; Krois, E.; Chen, W.; Everett, C. R.; Drewes, J.; Strunskus, T.; Gensch, M.; Rubeck, J.; Haisch, C.; Schwartzkopf, M.; Faupel, F.; Roth, S. V.; Cheng, Y.-J.; Müller-Buschbaum, P. Template-Induced Growth of Sputter-Deposited Gold Nanoparticles on Ordered Porous TiO_2 Thin Films for Surface-Enhanced Raman Scattering Sensors. *ACS Appl. Nano Mater.* **2022**, *5*, 7492-7501.

[168] Müller-Buschbaum, P., The Active Layer Morphology of Organic Solar Cells Probed with Grazing Incidence Scattering Techniques. *Adv. Mater.* **2014,** *26* (46), 7692-7098.

[169] Wang, Y.; Li, D.; Sun, Y.; Zhong, L.; Liang, W.; Qin, W.; Guo, W.; Liang, Z.; Jiang, L. Multiplexed Assembly of Plasmonic Nanostructures Through Charge Inversion on Substrate for Surface Encoding. *ACS Appl. Mater. Interfaces* **2020**, *12*, 6176-6182.

[170] Chen, K.; Ding, S. J.; Ma, S.; Wang, W.; Liang, S.; Zhou, L.; Wang, Q. Q. Enhancing Photocatalytic Activity of Au-Capped CdSPbS Heterooctahedrons by Morphology Control. J. Phys. Chem. C 2020, 124, 7938-7945.

[171] Li, F.; Liu, Y.; Shi, G.; Chen, W.; Guo, R.; Liu, D.; Zhang, Y.; Wang, Y.; Meng, X.; Zhang, X.; Lv, Y.; Deng, W.; Zhang, Q.; Shi, Y.; Chen, Y.; Wang, K.; Shen, Q.; Liu, Z.; Müller-Buschbaum, P.; Ma, W. Matrix Manipulation of Directly-Synthesized PbS Quantum Dot Inks Enabled by Coordination Engineering. *Adv. Funct. Mater.* **2021**, *31*, 2104457.

[172] Liu, Y.; Wang, Y.; Sun, Y.; Li, D.; Liang, Z.; Liang, W.; Gao, H.; Qin, W.; Qian, H.; Jiang, L. Programmable Assembly of Colloidal Nanoparticles Controlled by Electrostatic Potential Well. *Small Struct.* **2022**, *3*, 2200066.

[173] Dai, M.; Chen, H.; Feng, R.; Feng, W.; Hu, Y.; Yang, H.; Liu, G.; Chen, X.; Zhang, J.; Xu, C. Y.; Hu, P. A Dual-Band Multilayer InSe Self-Powered Photodetector with High Performance Induced by Surface Plasmon Resonance and Asymmetric Schottky Junction. *ACS Nano* **2018**, *12*, 8739-8747.

[174] Kunwar, S.; Pandit, S.; Jeong, J. H.; Lee, J. Improved Photoresponse of UV Photodetectors by the Incorporation of Plasmonic Nanoparticles on GaN Through the Resonant Coupling of Localized Surface Plasmon Resonance. *Nano-Micro Lett.* **2020**, *12*, 91.

[175] Wang, B.; Zou, Y.; Lu, H.; Kong, W.; Singh, S. C.; Zhao, C.; Yao, C.; Xing, J.; Zheng, X.; Yu, Z.; Tong, C.; Xin, W.; Yu, W.; Zhao, B.; Guo, C. Boosting Perovskite Photodetector Performance in NIR Using Plasmonic Bowtie Nanoantenna Arrays. *Small* **2020**, *16*, 2001417.

[176] Li, Y.; DiStefano, J. G.; Murthy, A. A.; Cain, J. D.; Hanson, E. D.; Li, Q.; Castro, F. C.; Chen, X.; Dravid, V. P. Superior Plasmonic Photodetectors Based on Au@MoS_2 Core-Shell Heterostructures. *ACS Nano* **2017**, *11*, 10321-10329.

List of publications

Publications related to the dissertation

- Guan, T.; Chen, W.; Tang, H.; Li, D.; Wang, X.; Weindl, C. L.; Wang, Y.; Liang, Z.; Liang, S.; Xiao, T.; Tu, S.; Roth, S. V.; Jiang, L.; Müller-Buschbaum, P., Decoding the Self-Assembly Plasmonic Interface Structure in a PbS Colloidal Quantum Dot Solid for a Photodetector. *ACS Nano* **2023,** *17* (22), 23010-23019.

- Guan, T.; Liang, S.; Drewes, J.; Strunskus, T.; Gensch, M.; Rubeck, J.; Haisch, C.; Schwartzkopf, M.; Faupel, F.; Roth, S. V.; Jiang, L.; Müller-Buschbaum, P., High-power Impulse Magnetron Sputter Deposition of Ag on Self-assembled Au Nanoparticle Arrays at Low Temperature Dewetting Conditions. *ACS Appl Mater Interfaces* **2024,** *16*(30), 40286-40296.

Further publications

- Liang, S.; Guan, T.; Yin, S.; Krois, E.; Chen, W.; Everett, C. R.; Drewes, J.; Strunskus, T.; Gensch, M.; Rubeck, J.; Haisch, C.; Schwartzkopf, M.; Faupel, F.; Roth, S. V.; Cheng, Y.-J.; Müller-Buschbaum, P., Template-Induced Growth of Sputter-Deposited Gold Nanoparticles on Ordered Porous TiO_2 Thin Films for Surface-Enhanced Raman Scattering Sensors. *ACS Applied Nano Materials* **2022,** *5* (5), 7492-7501.

- Li, Y.; Li, Y.; Heger, J. E.; Zhou, J.; Guan, T.; Everett, C. R.; Wei, W.; Hong, Z.; Wu, Y.; Jiang, X.; Yin, S.; Yang, X.; Li, D.; Jiang, C.; Sun, B.; Müller-Buschbaum, P., Revealing Surface and Interface Evolution of Molybdenum Nitride as Carrier-Selective Contacts for Crystalline Silicon Solar Cells. *ACS Appl Mater Interfaces* **2023,** *15* (10), 13753-13760.

- Ding, P.; An, H.; Zellner, P.; Guan, T.; Gao, J.; Müller-Buschbaum, P.;

Weckhuysen, B. M.; van der Stam, W.; Sharp, I. D., Elucidating the Roles of Nafion/Solvent Formulations in Copper-Catalyzed CO(2) Electrolysis. *ACS Catal* **2023,** *13* (8), 5336-5347.

- Guo, R.; Xiong, Q.; Ulatowski, A.; Li, S.; Ding, Z.; Xiao, T.; Liang, S.; Heger, J. E.; Guan, T.; Jiang, X.; Sun, K.; Reb, L. K.; Reus, M. A.; Chumakov, A.; Schwartzkopf, M.; Yuan, M.; Hou, Y.; Roth, S. V.; Herz, L. M.; Gao, P.; Müller-Buschbaum, P., Trace Water in Lead Iodide Affecting Perovskite Crystal Nucleation Limits the Performance of Perovskite Solar Cells. *Adv Mater* **2024,** *36* (7), e2310237.

- Xiao, T.; Bing, Z.; Wu, Y.; Chen, W.; Zhou, Z.; Fang, F.; Liang, S.; Guo, R.; Tu, S.; Pan, G.; Guan, T.; Wang, K.; Sun, X. W.; Huang, K.; Knoll, A.; Wang, Z. L.; Müller-Buschbaum, P., A multi-dimensional tactile perception system based on triboelectric sensors: Towards intelligent sorting without seeing. *Nano Energy* **2024,** *123*.

- Xiao, T.; Tu, S.; Tian, T.; Chen, W.; Cao, W.; Liang, S.; Guo, R.; Liu, L.; Li, Y.; Guan, T.; Liu, H.; Wang, K.; Schwartzkopf, M.; Fischer, R. A.; Roth, S. V.; Müller-Buschbaum, P., Autonomous self-healing hybrid energy harvester based on the combination of triboelectric nanogenerator and quantum dot solar cell. *Nano Energy* **2024,** *125*.

- Liang, Y.; Zheng, T.; Sun, K.; Xu, Z.; Guan, T.; Apfelbeck, F. A. C.; Ding, P.; Sharp, I. D.; Cheng, Y.; Schwartzkopf, M.; Roth, S. V.; Müller-Buschbaum, P., Operando Study Insights into Lithiation/Delithiation Processes in a Poly(ethylene oxide) Electrolyte of All-Solid-State Lithium Batteries by Grazing-Incidence X-ray Scattering. *ACS Appl Mater Interfaces* **2024,** *16* (26), 33307-33315.

Scientific reports

- Guan T., Müller-Buschbaum P., “Fabrication on Plasmonic Nanostructures in Photovoltaics” Lehrstuhl für Funktionelle Materialien, Annual Report, 2019.

- Guan T., Müller-Buschbaum P., “Fabrication on Plasmonic Nanostructures in Optoelectronic Devices”, Lehrstuhl für Funktionelle Materialien, Annual Report, 2020.

- Guan T., Müller-Buschbaum P., “Fabrication on Plasmonic Nanostructures in Optoelectronic Devices”, Lehrstuhl für Funktionelle Materialien, Annual Report,

2021.

- Guan T., Müller-Buschbaum P., “Self-assembly of plasmonic nanostructures in optoelectronic devices”, Lehrstuhl für Funktionelle Materialien, Annual Report, 2022.

- Guan T., Müller-Buschbaum P., “Sputter deposition of Ag on self-assembled Au nanoarrays”, Lehrstuhl für Funktionelle Materialien, Annual Report, 2023.

Conference talks

- Guan T., Müller-Buschbaum P., “Decoding the Self-assembled Plasmonic Nanostructure in Colloidal Quantum Dots for Photodetectors” 10th International Workshop on Functional Nanocomposites, Varese, Italy, 2021.

- Guan T., Apfelbeck F. A. C., Yazdanshenas B., “Atomic Force Microscopy”, Polymer Science Summer School, Obertauern, Austria, 2022.

- Guan T., Liang S., Zheng T., “Metal Nanoparticles”, Polymer Science Summer School, Obertauern, Austria, 2023.

Conference poster presentations

- Guan, T., Chen, W., Liang, S., Jiang, L.; Weindl C. L., Roth S. V., Jiang L., Müller-Buschbaum, P., “Fabrication on Plasmonic Nanostructures in Photovoltaics”, 10th Energy Colloquium of the Munich School of Engineering, Garching, Germany, 2020.

- Guan, T., Chen, W., Liang, S., Jiang, L.; Weindl C. L., Roth S. V., Jiang L., Müller-Buschbaum, P., “Fabrication on Plasmonic Nanostructures in Photoelectronic Devices” MLZ User Meeting 2020, Munich, 2020.

- Guan, T., Chen, W., Tang H., Liang, S., Jiang, L.; Weindl C. L., Roth S. V., Jiang L., Müller-Buschbaum, P., “Fabrication on Plasmonic Nanostructures in Photoelectronic Devices”, Virtual DPG Spring Meeting, Germany, 2021.

- Guan, T., Guo R., Jiang L., Müller-Buschbaum, P., “Plasmonic Nanostructures in Photovoltaics”, 11th Energy Colloquium of the Munich School of Engineering, Garching, Germany, 2021.

- Guan, T., Chen, W., Tang H., Liang, S., Jiang, L.; Weindl C. L., Roth S. V., Jiang L., Müller-Buschbaum, P., “Decoding the Self-assembled Plasmonic Nanostructure in Colloidal Quantum Dots for Photodetectors”, DPG Meeting SKM 2021, Germany, 2021.

- Guan, T., Chen, W., Tang H., Liang, S., Jiang, L.; Weindl C. L., Roth S. V., Jiang L., Müller-Buschbaum, P., “Decoding the Self-assembled Plasmonic Nanostructure in Colloidal Quantum Dots for Photodetectors”, MLZ User Meeting 2021, Germany, 2021.

- Guan, T., Guo R., Jiang L., Müller-Buschbaum, P., “Plasmonic Nanostructures in Photovoltaics”, 12th Energy Colloquium of the MEP, Garching, Germany, 2022.

- Guan, T.; Liang, S.; Drewes, J.; Strunskus, T.; Gensch, M.; Rubeck, J.; Haisch, C.; Schwartzkopf, M.; Faupel, F.; Roth, S. V.; Jiang, L.; Müller-Buschbaum, P., “Influence of thermal effects on a combinatorial plasmonic nanostructure for biodetection”, MLZ User Meeting 2022, München, Germany, 2022.

- Guan, T.; Liang, S.; Drewes, J.; Strunskus, T.; Gensch, M.; Rubeck, J.; Haisch, C.; Schwartzkopf, M.; Faupel, F.; Roth, S. V.; Jiang, L.; Müller-Buschbaum, P., “Influence of thermal effects on a combinatorial plasmonic nanostructure for biodetection”, DPG Spring Meeting of the Condensed Matter Section 2023, Dresden, 26-31 March 2023.

Acknowledgements

Here, I want to express my gratitude to everyone who contributed to the projects in this dissertation and supported me over the years. This thesis would not have been possible without their numerous contributions to the findings presented here. I would like to acknowledge them briefly, in no order.

I am deeply grateful to my supervisor, Prof. Dr. Peter Müller-Buschbaum, for the opportunity to join the Chair of Functional Materials at the Physics Department. His guidance and invaluable input, rooted in his deep knowledge and intuition in physics, have been crucial throughout my time in his group. I have learned extensively from him about advanced scattering techniques, presenting results, and scientific writing. I am also thankful for the incredible opportunity to participate in beamtimes at DESY (Deutsches Elektronen-Synchrotron) in Hamburg. His support in sending me to conferences, workshops, and scientific meetings allowed me to learn from other scientists and become an active member of the scientific community. His openness to collaboration greatly encouraged me to work with other groups, which is constructive in completing my projects, especially as the sole student working on plasmonics in our group.

I also wish to express my deep gratitude to Prof. Dr. Lin Jiang at the Institute of Functional Nano and Soft Materials (FUNSOM) for supporting my participation in the TUM-FUNSOM international cooperation program. This opportunity enabled me to join Peter's group and embark on my Ph.D. journey. As my collaborating professor in this program, her insightful feedback on my questions and needs has been immensely valuable. Additionally, I would like to acknowledge the members of Lin's group, including Dr. Zhiqiang Liang, Dr. Wenkai Liang, Yawen Wang, and Dong Li, for their assistance with Au NP synthesis, photodetector device fabrication, SERS measurements, and their valuable suggestions for the project.

A special thank you goes to my mentor, Prof. Dr. Christine M. Papadakis, for her suggestions during seminar talks and workshops, as well as to our secretaries, Carola Kappauf and Marion Waletzki, for their help and excellent organization of group events during my time at the Chair.

I would like to thank the P03 beamline scientists at DESY, Hamburg, Prof. Dr.

Stephan V. Roth and Dr. Matthias Schwartzkopf for providing me with access to learning and operating the synchrotron-based large facility. My thanks also go to Prof. Dr. Franz Faupel, Kristian A. Reck, Jonas Drewes, and Thomas Strunskus at Kiel University for their collaboration on the sputtering beamtime at DESY. Their contributions helped me a lot.

Furthermore, I am grateful to Prof. Dr. Emiliano Cortés, Yicui Kang, and Dr. Evangelina Pensa for their open collaboration on SERS measurements and valuable suggestions on manuscript writing.

I also want to thank my collaborators in Shenzhen, Haodong Tang and Xiao Wang, for their assistance with PbS quantum dots synthesis and photodetector characterization.

I am highly appreciated that Prof. Alexander Holleitner and Peter Weiser give me the access to the SEM measurement.

I have particularly enjoyed my time at the Chair of Functional Materials over the past few years. The moments spent with my kind and lovely colleagues are the most memorable. I cherish and miss our participation in beamtimes, summer school, seminar talks, conferences, beer gardens, BBQs, and coffee break events together. The time spent with you all has been incredibly happy and unforgettable.

I want to thank my colleagues who expericed beamtime with me at the P03 beamline: Dr. Christian Weindl, Dr. Suzhe Liang, Dr. Marc Gensch, Christopher Everett, Yusuf Bulut, Constantin Harder, Yuxin Liang, Fabian Apfelbeck, Yingying Yan, Kun Sun, Xiongzhuo Jiang, and Zerui Li, for their help in conducting experiments together. Additionally, I am grateful to the Alumni of E13: Dr. Dan Yang, Dr. Xinyu Jiang, Dr. Wei Chen, Dr. Wei Cao, Dr. Nian Li, Dr. Shanshan Yin, Dr. Renjun Guo, Dr. Ting Tian, Dr. Suo Tu, Dr. Julian E. Heger, Dr. Dominik Schwaiger, Dr. Lennart Reb, Dr. Shambhavi Pratap, Dr. Apostolos Vagias, Dr. Yuqin Zou, Dr. Anna-Lena Oechsle, Dr. Peixi Wang, Dr. Tianxiao Xiao, Simon J. Schaper, Manuel Scheel, Christina Geiger Dr. Florian Jung, Dr. Chia-Hsin Ko, Dr. Jia-Jhen Kang, whose scientific suggestions have helped and inspired me in my project.

I would also like to thank the students I advised during my doctoral studies: Kotone Tomioka, Lyu Yi, and Kyriaki Nektaria Gavriilidou. I am very pleased that they are interested in my topic and chose as their graduation theses. Supervising and getting to know them has been a continuous learning process for me, providing an opportunity to strengthen my team leadership skills. I am delighted that they successfully completed their theses.

Next, I want to express my gratitude to my colleagues, Peiran Zhang, Guangjiu Pan, Xiaojing Ci, Ruoxuan Qi for the thesis proof reading of my thesis. And, thank to David Kosbahn, Feifei Zheng, Wenqi Xu, Julija Reitenbach, Lukas Spanier, Zhuijun Xu, Jinsheng Zhang, Tianle Zheng, Huaying Zhong, Thomas Baier, Yanan Li, Pablo

Alvarez Herrera, Tobias Hölderle, Linus Huber, Morgan Le Dû, Thien An Pham, Ivana Pivarnikova, Julija Reitenbach, Lukas Spanier, Zhaonan Jin, and Lixing Li, and Ming Yang for making this a wonderful experience at our Chair.

The time spent with you all has been truly unforgettable, but as they say, all good things must come to an end. I sincerely wish everyone mentioned a bright and prosperous future.

I would also like thank to the Grammarly and Open Ai for the thesis grammar and typo checking.

Lastly, I express my deepest gratitude to my family for their constant support of my study for nearly 25 years. I am especially thankful to my father, a devoted physics teacher, who sparked my curiosity about the world early on. I am also profoundly grateful to my grandfather for his upbringing. As I departed China to begin my doctoral studies in Munich, I never imagined our farewell would be our final goodbye. Thank you for naming me Tianfu; this name will carry your best wishes for me and keep my thoughts of you alive throughout my life. I miss you deeply.

Dedicated to the memory of my grandfather Hongxian Guan

Tianfu Guan
13.07.2024
Wuyin, Xinwei, Jiachen
Garching, Germany